Vortex regeneration mechanism in the self-sustaining process of wall-bounded flows

H. J. Bae*, B. J. McKeon

Graduate Aerospace Laboratories, California Institute of Technology, Pasadena, CA 91125, USA

The structure of near-wall turbulence has been extensively investigated over the past half-century. In the vicinity of the wall, the flow is found to be highly organised, consisting of streamwise rolls and low- and high-speed streaks [10, 15, 3] that are involved in a quasi-periodic regeneration cycle [12, 13, 1]. However, despite the large effort devoted to the subject, questions still remain in understanding the exact mechanisms by which turbulence self-sustains in wall-bounded turbulent shear flows, and the dynamics in which these structures interact are still uncertain.

The consensus from previous investigations ([7, 6, 8], among many others) is that the streaks are significantly amplified by the quasi-streamwise vortices via the lift-up effect; the amplified streaks subsequently undergo a rapid streamwise meandering motion, reminiscent of streak instability or transient growth, which eventually results in the breakdown of the streaks and regeneration of new quasi-streamwise vortices. Streak formation by streamwise vortices has been extensively documented in the literature [2, 3, 4, 5], and streak breakdown has also received considerable attention [9, 6, 17, 14]. Regarding the final component of the self-sustaining process, the streamwise vortex regeneration through nonlinear interactions, there is a lack of consensus, and many possible mechanisms have been proposed.

In this work, the streamwise vortex regeneration mechanism in the self-sustaining process of wall-bounded turbulence is investigated using resolvent analysis [11], which identifies the principal forcing mode that produces the maximum amplification of the response modes in the minimal channel for the buffer layer [7]. The identified mode is then projected out from the nonlinear term of the Navier–Stokes equations at each time step from the velocities in direct numerical simulations of the corresponding minimal channel. The results show that the removal of the principal forcing mode is able to inhibit turbulence while removing the subsequent modes instead of the principal one only marginally affects the flow.

Analysis of the dyadic interactions in the nonlinear term shows that the contributions toward the principal forcing mode come from a limited number of wavenumber interactions. By computing the contributions toward the principal forcing mode at each time step, we can identify high forcing-intensity events that produce the most contribution towards the principal forcing mode. Using conditional averaging on these events, the flow structures that are responsible for generating the principal forcing mode, and thus the nonlinear interaction to self-sustain turbulence, are identified to be spanwise rolls interacting with oblique streaks, shown in the form of autocorrelations of velocity fluctuations in Fig. 1. The interaction of the two components highlighted here regenerates streamwise vortices, which through the lift-up mechanism amplifies streamwise streaks. These streamwise streaks break down, spawning new generations of meandering streaks and spanwise rolls, completing the self-sustaining process. This corroborates previous studies on the vortex regeneration mechanism and characterises the underlying quadratic interactions in the self-sustaining process of the minimal channel using resolvent analysis. Morever, this has implications toward novel control schemes (e.g. drag reduction) that can be designed to target the structures identified in this study.

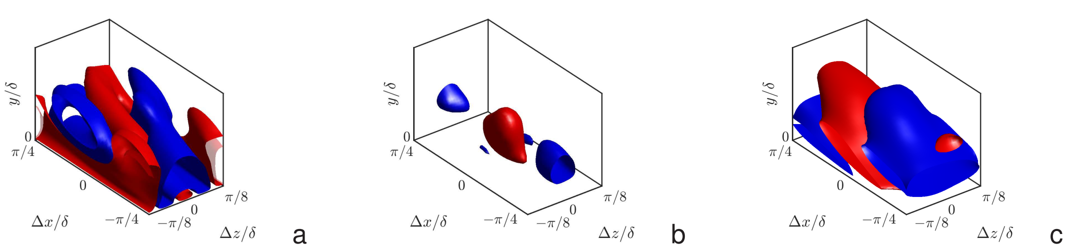

Fig. 1: Autocorrelations of (a) streamwise, (b) wall-normal and (c) spanwise velocity components conditioned to high forcing-intensity events. Autocorrelations are computed for $y^+ \approx 40$, and isosurfaces are 0.1 (red) and -0.04 (blue).

References

[1] Adrian, R. J. *Phys. Fluids*, **19**(4):041301, 2007.
[2] Bakewell Jr, H. P., & Lumley, J. L. *Phys. Fluids*, **10**(9):1880-1889, 1967,
[3] Blackwelder, R. F., & Eckelmann, H. *J. Fluid Mech.*, **94**(3):577-594, 1979.
[4] Butler, K. M., & Farrell, B. F. *Phys. Fluids A*, **5**(3):774-777, 1993.
[5] Chernyshenko, S. I., & Baig, M. F. *J. Fluid Mech.*, **544**:99-131, 2005.
[6] Hamilton, J. M., Kim, J., & Waleffe, F. *J. Fluid Mech.*, **287**:317-348, 1995.
[7] Jiménez, J., & Moin, P. *J. Fluid Mech.*, **225**(4):213-240, 1991.
[8] Jiménez, J., & Pinelli, A. *J. Fluid Mech.*, **389**:335-359, 1999.
[9] Kim, H. T., Kline, S. J., & Reynolds, W. C. *J. Fluid Mech.*, **50**(1):133-160, 1971.
[10] Kline, S. J., Reynolds, W. C., Schraub, F. A., & Runstadler, P. W. *J. Fluid Mech.*, **30**(4):741-773, 1967.
[11] McKeon, B. J., & Sharma, A. S. *J. Fluid Mech.*, **658**:336-382, 2010.
[12] Robinson, S. K. *Ann. Rev. Fluid Mech.*, **23**(1):601-639, 1991.
[13] Panton, R. L. *Prog. Aerosp. Sci.*, **37**(4):341-383, 2001.
[14] Schoppa, W., & Hussain, F. *J. Fluid Mech.*, **453**:57-108, 2002.
[15] Smith, C. R., & Metzler, S. P. *J. Fluid Mech.*, **129**:27-54, 1983.
[16] Sreenivasan, K. R. *Turbulence Management and Relaminarisation*. Springer, 1998
[17] Waleffe, F. *Phys. Fluids*, **7**(12):3060-3066, 1995.

*corresponding author: hjbae@caltech.edu

A fluid mechanic's analysis of the teacup singularity

D. Barkley[1]*

[1]Mathematics Institute, University of Warwick, Coventry, CV4 7AL

Introduction

In 1926 Einstein published a short paper explaining the meandering of rivers [1]. He famously began the paper by discussing the secondary flow generated in a stirred tea cup – the flow now widely known to be responsible for the collection of tea leaves at the centre of a stirred cup of tea. In 2014, Luo and Hou (L&H) presented detailed numerical evidence of a finite-time singularity at the boundary of a rotating, incompressible, inviscid flow [2, 3]. The key to generating this singularity is the teacup effect. The present work is not aimed at proving the existence of a singularity for this flow, nor is it aimed at generating more highly resolved numerical evidence for the singularity than already exists. Rather, I assume that the flow simulated by L&H genuinely develops a singularity in finite time. My goal is to understand, from a fluid-mechanics perspective, why.

The flow under investigation is depicted in Fig. 1(a). The system is initialised with a pure azimuthal flow (swirl) having a sinusoidal dependence on the axial coordinate z. A pressure field is instantaneously generated to provide the radially inward force necessary to keep fluid parcels moving along circular paths. This results in high pressure at the cylinder wall where the circulation is largest ($z = \pm L/4$) and low pressure where this is no azimuthal flow ($z = 0$ and $z = \pm L/2$). Necessarily, then, there is a vertical variation in the pressure at the cylinder wall and this drives a secondary meridional flow. This is the teacup effect – the portion of the fluid just from $z = 0$ to $z = L/4$ corresponds to a cup of tea. (In an actual cup of tea, the variation in swirl with z is due to an Ekman a boundary layer at the bottom of the cup.)

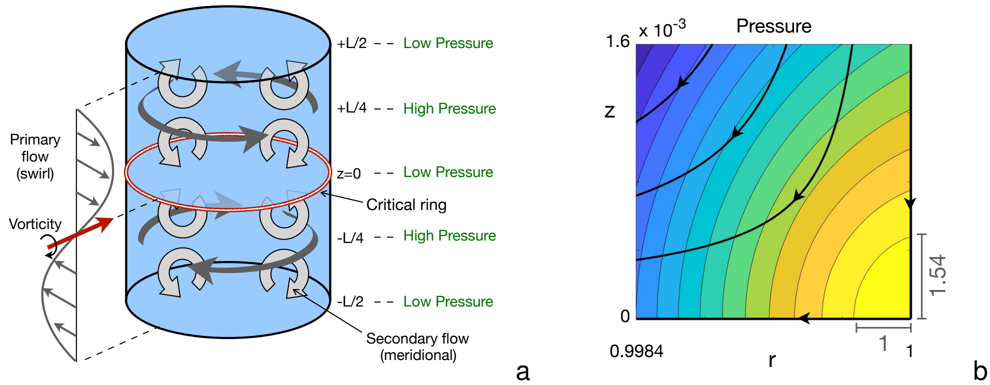

Fig. 1: (a) The teacup flow in a cylinder, periodic in the axial direction. The primary azimuthal flow (swirl) generates an axial variation in the pressure. This produces a secondary meridional flow that in turn drives azimuthal flow along the cylinder wall towards the critical ring. The shear of this azimuthal flow generates intense vorticity on the critical ring, ultimately leading to a singularity and a breakdown of the Euler equations. Note that by symmetry a second critical ring (not indicated) exists at $z = L/2$, which by periodicity is also at $z = -L/2$. In the actual configuration studied, the height L is only one sixth of the radius. (b) The pressure field (colour) and meridional-flow streamlines (black) near the critical ring ($r = 1, z = 0$). A pressure maximum exists on the critical ring to divert the incoming flow. The length ratio 1.54-to-1 associated with exponent γ is indicated (see text).

Results

Figure 1(b) shows the pressure field and meridional flow near the critical ring as the singularity is approached. A local pressure maximum forms on the critical ring to provide the stress necessary to bend (accelerate) the downward velocity to a radially inward velocity. In the vicinity of the critical ring the meridional flow is a saddle. The pressure field shown is similar to that reported by L&H at $t = 0.003505$, very close to the singularity time $T \simeq 0.0035056$ [3]. L&H note that the pressure maximum on the critical ring means that there is locally an adverse axial pressure gradient that decelerates flow on the cylinder wall. However, this does not mean that the pressure maximum inhibits the singularity. On the contrary, a pressure maximum like that in Fig. 1(b) will drive a singularity. This fact is central to this work.

Consider the velocity-gradient dynamics on the critical ring. Differentiating velocity gives the velocity-gradient tensor ∇u and differentiating the pressure gradient gives the pressure Hessian $\nabla(\nabla p)$. Symmetries dictate that on the critical ring the only non-zero derivatives entering these are

$$V = \partial_r u_r\big|_c\,, \quad W = \partial_z u_z\big|_c\,, \quad \Omega = \partial_z u_\theta\big|_c\,,$$
$$Q = \partial_{rr} p\big|_c\,, \quad P = \partial_{zz} p\big|_c\,,$$

where $\big|_c$ means evaluated on the critical ring. We will refer to Q and P as pressure curvatures. Straightforward differentiation of the Euler equations gives

$$\dot V + V^2 = -Q, \quad \dot\Omega + W\Omega = 0, \quad \dot W + W^2 = -P.$$

By incompressibility on the critical ring: $V + W = 0$. Thus V can be eliminated, giving the velocity-gradient dynamics

$$\dot W + W^2 = -P, \tag{1a}$$
$$\dot\Omega + W\Omega = 0, \tag{1b}$$
$$Q + P = -2W^2 \tag{1c}$$

These equations are exact, and while they are not closed ((1c) is insufficient to determine Q and P separately), they are extremely useful in examining what transpires in singularity formation. (1b) is commonly referred to as vortex stretching. For this flow, $\Omega = -\,\omega_r\big|_c$ is the absolute vorticity maximum [2, 3], so $\Omega = \|\omega\|_\infty$. (1c) is the pressure Poisson equation evaluated on the critical ring.

From Fig. 1(b) we see that both pressure curvatures, Q and P, are negative (a pressure maximum occurs on the critical ring), but that they are not equal. The radial curvature is larger in magnitude than axial curvature, that is $|Q| > |P|$. To understand the importance of this, suppose that for $t \geq t_0$,

$$Q/P = a^2, \quad \text{where a} > 1. \tag{2}$$

(More precisely, we need $\inf_{t\geq t_0} a > 1$.) Using (2) to eliminate Q from (1c) gives $P = -2W^2/(a^2+1)$, which can then be used to eliminate P from (1a). The velocity-gradient equations (1) then become

$$\dot W = -\frac{W^2}{\gamma}, \quad \dot\Omega = -W\Omega \tag{3}$$

where $\gamma = (a^2+1)/(a^2-1) < \infty$.

The flow at t_0 is assumed to be axially contracting: $W(t_0) < 0$. Without loss of generality we redefine the origin of time so that $t_0 = 0$. Sacrificing generality here for simplicity, we take $a > 1$ to be constant. The solution to Eqs. (3) is then just

$$W(t) = -\frac{\gamma}{T-t} \sim (T-t)^{-1}, \quad \Omega(t) = \frac{\Omega_0 T^\gamma}{(T-t)^\gamma} \sim (T-t)^{-\gamma}, \tag{4}$$

where $T = -\gamma/W(0) > 0$ is the singularity time and $\Omega_0 = \Omega(0)$. These are the known divergences as $t \to T$ [2, 3]. In particular, $\Omega = \|\omega\|_\infty$ diverges with exponent $-\gamma$. All other divergences associated with the singularity follow immediately from invariances of the Euler equations and the value of γ. We know from L&H that $\gamma \simeq 2.46$, corresponding to $a \simeq 1.54$. The corresponding ratio of length scales is indicated in Fig. 1(b).

The fundamental point is the following. Incompressibility locks radial expansion and axial contraction together such that it is not the signs of Q and P that are important for singularity formation; it is their mismatch. A persistent mismatch in pressure curvatures on the critical ring will drive the flow to a singularity. Of interest here is $|Q| > |P|$. The pressure contours in Fig. 1(b) are the signature of this simple mechanism.

To explain the origin of the pressure mismatch, linearity of the pressure Poisson equation is exploited to decompose the pressure field into a superposition of independent contributions arising from the meridional flow and from the swirl. The swirl pressure is further decomposed into axial mean and fluctuating components, where the fluctuating component itself has distinct contributions maintaining incompressibility and confining the flow. The key pressure field driving singularity formation is shown to be that confining the fluid within the cylinder walls.

References

[1] Einstein A. *Naturwissenschaften* **14**: 223–224, 1926.
[2] Luo G., Hou T.Y. *Proc Natl Acad Sci USA* **111**: 12968–12973, 2014.
[3] Luo G., Hou T.Y. *Multiscale Model Sim.* **12**: 1722–1776, 2014.

*corresponding author: D.Barkley@warwick.ac.uk

Turbulence modeling of strongly-coupled gas-particle flows

J. Capecelatro[1], S. Beetham[1]

[1]Department of Mechanical Engineering, University of Michigan, Ann Arbor, MI 48109, USA

Introduction

Many natural and industrial processes involve the flow of solid particles or liquid droplets whose dynamical evolution and morphology are intimately coupled with a carrier gas. A peculiar behavior of disperse multiphase flows are their ability to give rise to large-scale structures (hundreds to thousands of times the size of individual particles), from dense clusters to nearly-particle-free voids (see Fig. 1). Seminal works by G. K. Batchelor have provided theoretical estimates describing the motion of collections of solid particles suspended in viscous flows [2, 3], in addition to important insights into instabilities present in such systems [4]. For example, Batchelor demonstrated that small rigid spheres falling under gravity gives rise to long-range hydrodynamic interactions resulting in hindered settling [2].

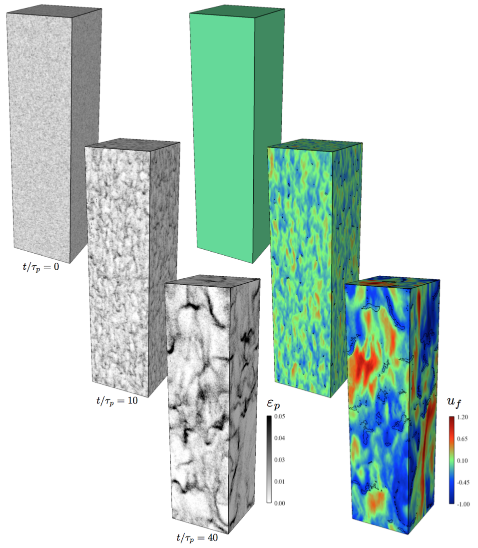

Fig. 1: Simulation of fully-developed CIT [1]. Evolution of particle positions ε_p (left) and fluid velocity $\boldsymbol{u}_f$ (right). Particles, which are initially randomly distributed, spontaneously form clusters (i.e., regions of large ε_p) due to the negative correlation between ε_p and $\boldsymbol{u}_f$.

In the present work, we will demonstrate that at higher Reynolds numbers and particle concentrations, momentum exchange between the phases results in *enhanced* settling when the mean mass loading is order one or larger. In statistically homogeneous gravity-driven flows, the average settling speed can be written as $\langle u_p \rangle \approx \langle \varepsilon_p u_f \rangle / \langle \varepsilon_p \rangle - \tau_p g$, where angled brackets denote a temporal and spatial average, ε_p is the particle-phase volume fraction, u_f is the fluid-phase velocity, τ_p is the particle response time and g is gravity. In this expression, the phase-averaged fluid velocity, $\langle \varepsilon_p u_f \rangle / \langle \varepsilon_p \rangle$, is sometimes referred to as the fluid velocity *seen* by the particles. At sufficient mass loading, the fluid-phase velocity and particle concentration are often highly correlated, and fluctuations in particle concentration can generate and sustain fluid-phase turbulence (see Fig. 1), which we refer to as fully-developed cluster-induced turbulence (CIT). Such coupling can effectively 'demix' the underlying flow, which has enormous consequences in engineering systems [5]. High-resolution simulations of unbounded, gravity-driven fluid-particle flows and particle-laden channel flows will be presented to reveal how multiphase interactions at the particle scale augment or restrict large-scale flow processes, and provide unique insight multiphase turbulence closure.

Turbulence modeling using machine learning

Building upon our previous work [1, 6], the exact (but unclosed) Reynolds-averaged equations for two-way coupled particle-laden flows will be presented. We will demonstrate that existing closure based on single-phase turbulence fails to adequately model the unclosed terms. In an effort to transform the simulation data into a robust and predictive turbulence model, a new data-driven approach based on sparse regression will be presented. While Neural Networks have been a popular choice in the machine learning community, they have a notable drawback: the resultant model does not take on a closed form in the traditional sense and instead acts as 'black box'. This makes integration into existing CFD solvers and dissemination of learned models challenging. One of the most promising, recently introduced techniques for developing closure models is Sparse Regression [7]. This technique uses an Ordinary Least Squares cost functional with an L-1 norm penalty. It has several key benefits: (1) given the strict convex nature of the cost functional under certain conditions, a unique solution is ensured; (2) it results in a compact, algebraic model; (3) it is simple and relatively straight forward to implement; and (4) several efficient algorithms for this class of problem have been developed over the past decade, making this tool accessible even for very large datasets. In order to apply this toward turbulence modeling, we take the following approach. First, we postulate that the model for some tensor quantity, $\mathbb{D}$, can be written as $\mathbb{D} = \mathbb{T}\hat{\beta}$. Where $\mathbb{T}$ is a matrix comprised of an invariant tensor basis and $\hat{\beta}$ is a *sparse* vector of coefficients. An important pre-processing step for ensuring invariance of the resultant model is to rearrange all tensor quantities (namely, $\mathbb{D}$ and $\mathbb{T}$) into column vectors. This is accomplished by vertically concatenating the unique, non-zero components of each tensor into a

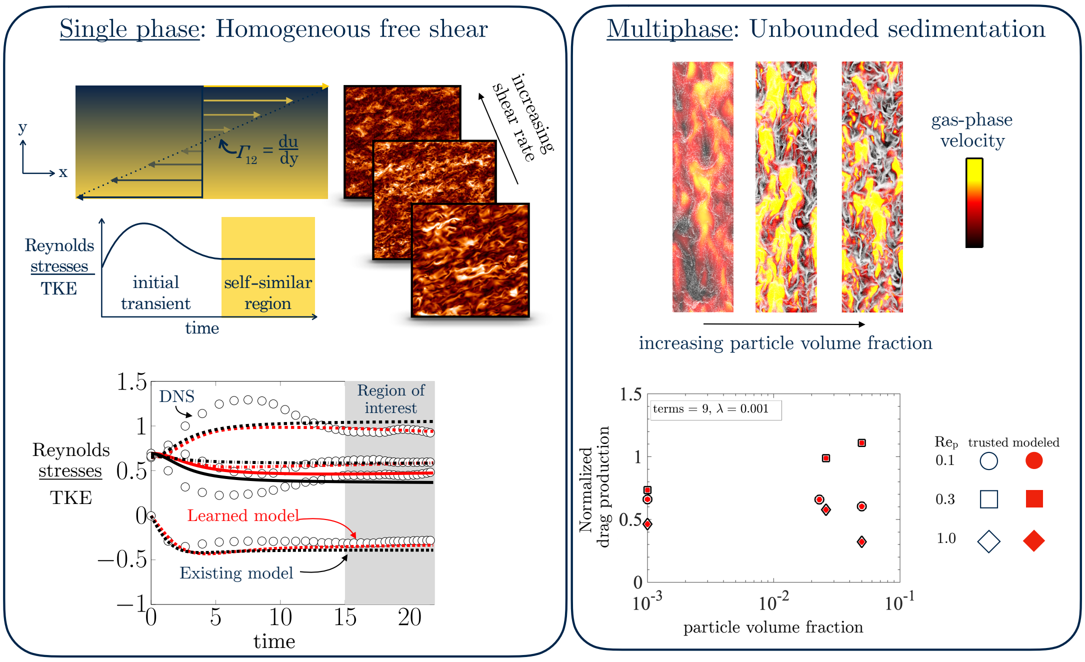

Fig. 2: Demonstration of sparse regression for learning turbulence models. Self-similar behavior of homogeneous free shear turbulence (left pane) is learned from DNS datasets spanning three shear rates (upper right), with improved performance (red lines, lower plot) over state-of-the-art, existing models (black lines). An accurate drag production model is learned for 3D unbounded, gas-solid flow (right pane), over varying particle Reynolds number and particle volume fractions (top). The 'trusted', highly resolved Euler-Lagrange data is shown as empty symbols and the learned model prediction is shown as red symbols.

column vector, over each realization in time and each configuration under study. In formulating the basis $\mathbb{T}$, it is important to ensure that each of the tensors in the basis (each a column in $\mathbb{T}$) has the same properties as $\mathbb{D}$, e.g. symmetric, traceless, etc.

After identifying the basis $\mathbb{T}$ using physics-based insight for the problem under consideration, the coefficients are determined by solving the following optimization:

$$\hat{\beta} = \min_{\beta} ||\mathbb{D} - \mathbb{T}\beta||_2^2 + \lambda||\beta||_1, \tag{1}$$

where the L-2 norm regresses the coefficients to the trusted data $\mathbb{D}$ and the L-1 norm promotes sparsity. The parameters λ is user-specified and balances model complexity and accuracy.

This method will be demonstrated on both single-phase and multiphase flows, two examples of which are shown in Fig. 2. The left pane highlights the success of this method in generating improved models for single-phase, homogeneous free shear turbulence over existing state-of-the-art models. The right pane demonstrates, for a single unclosed term in the multiphase Reynolds-averaged equations, the ability of this methodology to produce a highly accurate, and still compact and algebraic, model for 3D unbounded, gas-solid flow over a range of particle Reynolds numbers and volume fractions.

References

[1] J. Capecelatro, O. Desjardins, and R. O. Fox, "On fluid–particle dynamics in fully developed cluster-induced turbulence," *Journal of Fluid Mechanics*, vol. 780, pp. 578–635, 2015.

[2] G. K. Batchelor, "Sedimentation in a dilute dispersion of spheres," *Journal of fluid mechanics*, vol. 52, no. 2, pp. 245–268, 1972.

[3] G. K. Batchelor, "Sedimentation in a dilute polydisperse system of interacting spheres. Part 1. General theory," *Journal of Fluid Mechanics*, vol. 119, pp. 379–408, 1982.

[4] G. K. Batchelor, "A new theory of the instability of a uniform fluidized bed," *Journal of Fluid Mechanics*, vol. 193, pp. 75–110, 1988.

[5] S. Beetham and J. Capecelatro, "Biomass pyrolysis in fully-developed turbulent riser flow," *Renewable Energy*, vol. 140, pp. 751–760, 2019.

[6] J. Capecelatro, O. Desjardins, and R. O. Fox, "Strongly coupled fluid-particle flows in vertical channels. II. Turbulence modeling," *Physics of Fluids*, vol. 28, no. 3, p. 033306, 2016.

[7] S. L. Brunton, J. L. Proctor, and J. N. Kutz, "Discovering governing equations from data by sparse identification of nonlinear dynamical systems," *Proceedings of the National Academy of Sciences*, vol. 113, no. 15, pp. 3932–3937, 2016.

*corresponding author: jcaps@umich.edu

Mixing and Entrainment in Steady-State Gravity Currents

C. Cenedese[1*], J. N. McElwaine[2], J. M. Heninger[3]

[1]Woods Hole Oceanographic Institution, Physical Oceanography Department, Woods Hole, MA 02536, USA
[2]Durham University, Department of Earth Sciences, Durham, DH1 3LE, UK
[3]University of Texas at Austin, Department of Physics, Austin, TX 78712, USA

Introduction

Turbulent mixing plays an essential role on the large-scale ocean circulation. In particular, the dynamics controlling the entrainment in dense currents are fundamental to the formation, movement, and distribution of the densest water in the ocean: a cornerstone of the thermohaline circulation. However, investigating the stability and mixing processes in these currents is particularly challenging given that they occur at such small scales, and the flows are so rapid that full resolution of the dynamics is presently very difficult, if not impossible, in global circulation and climate models. Consequently, models must rely on parameterizations which require an understanding of the basic fluid mechanical processes regulating turbulence in stratified flows.

Existing parameterizations for entrainment in dense currents account primarily for the shear-induced mixing at the interface between the dense flow and the ambient fluid. However, to date studies have almost entirely focused on ‘run-down initial value problems’ and the fate of a dense current once it reaches a ‘quasi-steady’ state is unknown. Given that dense currents propagate for long distances along the continental slope and over the ocean bottom, it is fundamental to know if the dynamics regulating entrainment during these long periods are modified compared to the dynamics regulating the ‘transient’ regimes investigated up to date.

Results

We report laboratory experiments and Direct Numerical Simulations (fig. 1) which suggest that when in steady state, the dense current velocity and density profiles evolve to sharpen and stabilize the interface. Hence, the stability of the top interface of dense currents propagating in a quasi–steady state regime along the continental slopes or the ocean bottom may have a very different character and produce a very different amount of entrainment of ambient water than when the current is accelerating down a sill or through a constriction. A decrease in entrainment due to a more stable interface or a different kind of instability may result is a less dilute current that can then propagate for longer distances. This result may explain why turbidity currents have been observed to propagate for very long distances, longer than one would expect based on the current knowledge of mixing and evolution of gravity currents.

Direct Numerical Simulations (DNS) The DNS results (fig. 2, left) show that density $b = (\rho - \rho_a)/(\rho_d - \rho_a)$ and velocity $u = u'/U_a$ profiles present different ‘shapes’ with increasing distance x' from the nose (fig. 2, left: a,b), where ρ, ρ_d and ρ_a are the density of the current, dense and ambient inflows, respectively, U_a is the ambient fluid velocity, and the distance from the nose and the vertical

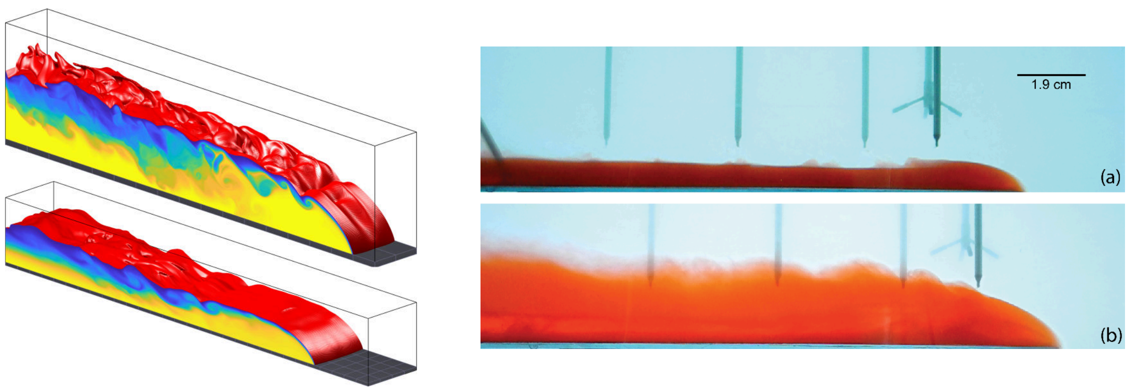

Fig. 1: *Left: DNS of dense currents in a steady state regime. Top: Re =5 000 and bottom: Re =2 000. Colors represent density and red is the 1% density iso-surface. Right: Side view of a dense current in a steady-state regime generated in the laboratory. (a) Re* ~ 650*: the dye suggests a sharp interface which present cusp like features indicative of Holmboe Wave Instability (HWI); (b) Re* $\sim 2\,500$*: the dye suggests a thick interface with Kelvin-Helmhotz Instability (KHI) billows behind the dense current.*

coordinate z' are nondimensionalized by the dense current height, i.e. $x = x'/h$ and $z = z'/h$. All the profiles are well fitted by an error function, but the change in the shape of the profiles is clearly visible. Fig. 2c shows the lengthscales over which the velocity varies, d, and the density varies, δ, for increasing distances from the nose. The head of the dense current presents a very sharp interface which rapidly increases its thickness up to $x \sim 5$ and then slowly becomes sharper with increasing distance from the nose. As qualitatively seen in fig. 1 (left), the dense current seems to have a more stable interface as the distance from the nose increases and a likely mechanism responsible for the apparent increased stability of the interface is the evolution of the density and velocity profiles towards a less sharp velocity gradient and a sharper density gradient, indicative of Holmboe Wave Instability (HWI). The results presented are for a Re $= 2\,000$ simulation but similar results were obtained for a simulation with Re $= 5\,000$, albeit the domain size was shorter and the distance behind the nose only reached to $x = 10$.

Laboratory Experiments Laboratory experiments were conducted with a similar configuration as the simulations. A dense current was generated in a tank with an ambient flow directed in the opposite direction than the dense current in order to obtain a steady current head position. We performed experiments in both the HWI (fig. 1,right: a) and Kelvin-Helmhotz Instability (KHI) (fig. 1, right: b) regimes which had a Re $= 650$ and $2\,500$, respectively. The experiment in the KHI regime showed that the density profile was sharp in the current head (fig. 2, right: b, blue line) but evolved towards a less sharp interface as the distance from the current nose increased up to $x \sim 7$ (fig. 2, right: b). This result is in agreement with the simulations' results in that the lengthscale over which the density varies, δ, increases for increasing distances from the nose up to $x \sim 5$. In order to observe a sharpening density profile, as suggested by the DNS results in fig. 2c, a longer tank is necessary. As expected, the experiment in the HWI regime presented very little entrainment and the velocity and density profiles remained sharp as the distance behind the nose increased (fig. 2 (right: a) and fig. 1 (right: a)). Measurements of density and velocity profiles in the head of the current showed that these two regimes corresponded to different vertical profiles of density and velocity. When the lengthscale δ over which the density changes is smaller than the one (d) for the velocity, the interface is unstable to HWI (fig. 1 (right: a) and fig. 2 (right: a)), while when these two scales are comparable the interface is unstable to KHI (fig. 1 (right: b) and fig. 2, right: b).

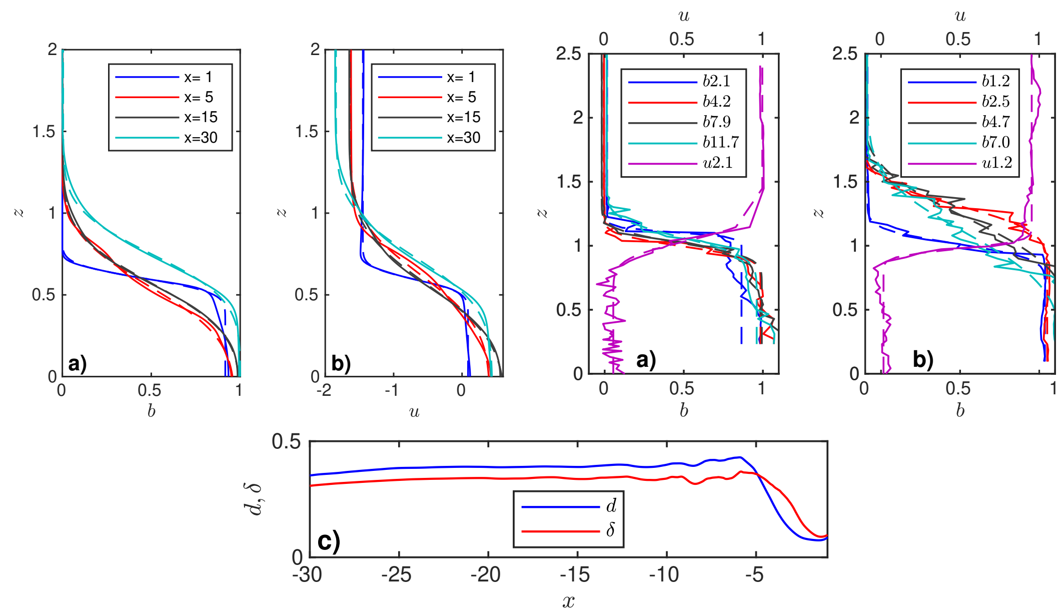

Fig. 2: *Left: (a) Density and (b) velocity profiles at several distances x from the nose of the current for a Re $= 2\,000$ steady-state DNS simulation. The dashed curves show the best fit to an error function. Bottom: (c) Lengthscales over which the velocity varies, d, and the density varies, δ, for increasing distances from the nose x. Right: Experimental results from a steady-state dense current (a) in the HWI regime (Re $= 650$, $U = 28\,\mathrm{mm\,s^{-1}}$) and (b) in the KHI regime (Re $= 2\,500$, $U = 42\,\mathrm{mm\,s^{-1}}$). The plots show the density profiles at four locations, indicated in the legend by a 'b' followed by the non-dimensional distance x from the nose, and one velocity profile in purple indicated in the legend by a 'u' followed by its location near the current head. The dashed curves show the best fit to an error function.*

*corresponding author: ccenedese@whoi.edu

The dynamics of stratified horizontal shear flows at low Péclet number

L. Cope[1]*, P. Garaud[2], C. P. Caulfield[3,1]

[1] DAMTP, University of Cambridge, Centre for Mathematical Sciences, Cambridge CB3 0WA, UK
[2] Department of Applied Mathematics, UC Santa Cruz, Santa Cruz, CA 95060, USA
[3] BP Institute, University of Cambridge, Madingley Rise, Madingley Road, Cambridge CB3 0EZ, UK

Introduction

Stratified flows, in which the background fluid density decreases upwards in a gravitational field, are ubiquitous. Examples in geophysics include atmospheres and oceans, while they also occur on astrophysical scales in planetary and stellar interiors. The interaction of a stable stratification with a background velocity distribution can develop into so-called stratified turbulence, key to transport processes in geophysical flows and also thought to play a crucial role in stellar interiors.

Oceanic and atmospheric flows, in which the Prandtl number is of order one, are often very strongly stratified, nevertheless turbulence still occurs. Density layering is key to understanding the properties of this 'layered anisotropic stratified turbulence' (LAST) regime that is characterised by anisotropic length scales and also anisotropy in the velocity field, and hence the associated turbulence.

On the other hand, the Prandtl number for astrophysical flows is typically significantly smaller than one, inhibiting the formation of density layers. This suggests that LAST dynamics cannot occur, raising the interesting question of whether analogous or fundamentally different regimes exist in the limit of strong thermal diffusion. Following work investigating vertically sheared velocity fields [1], this study aims to answer this question for the case of horizontally-sheared flows.

Mathematical formulation

We consider the dynamics of a vertically stratified, horizontally-forced Kolmogorov flow with streamwise coordinate x, cross-stream coordinate y and vertical coordinate z. The three-dimensional velocity field is given by $\mathbf{u}(x,y,z,t) = u\mathbf{e}_x + v\mathbf{e}_y + w\mathbf{e}_z$ and the total temperature field T includes perturbations $T'(x,y,z,t)$ away from a statically stable basic state. Triply periodic boundary conditions are imposed on T' and $\mathbf{u}$. The non-dimensionalized governing equations are equivalent to those studied in [2]:

$$\frac{\partial \mathbf{u}}{\partial t} + \mathbf{u}\cdot\nabla\mathbf{u} + \nabla p = \frac{1}{Re}\nabla^2\mathbf{u} + BT'\mathbf{e}_z + \sin(y)\mathbf{e}_x, \tag{1}$$

$$\frac{\partial T'}{\partial t} + \mathbf{u}\cdot\nabla T' + w = \frac{1}{RePr}\nabla^2 T', \tag{2}$$

$$\nabla\cdot\mathbf{u} = 0. \tag{3}$$

This set of standard equations depends on three non-dimensional numbers: the Reynolds number Re; the buoyancy parameter B; and the Prandtl number Pr, which determine the dynamics of the system.

Motivated by astrophysical systems, our focus is the little-studied limit of high Reynolds number but low Péclet number $Pe = RePr$ with $Pr \ll 1$. In the asymptotic limit of low Péclet number (LPN), Lignières [3] proposed that the standard equations can be approximated by a reduced set of equations in which the density fluctuations are slaved to the vertical velocity field $w = Pe^{-1}\nabla^2 T'$. These LPN equations, given by

$$\frac{\partial \mathbf{u}}{\partial t} + \mathbf{u}\cdot\nabla\mathbf{u} + \nabla p = \frac{1}{Re}\nabla^2\mathbf{u} + BPe\nabla^{-2}w\mathbf{e}_z + \sin(y)\mathbf{e}_x; \qquad \nabla\cdot\mathbf{u} = 0, \tag{4}$$

depend only on two non-dimensional parameters, notably the Reynolds number Re and the product of the buoyancy parameter and the Péclet number, BPe. We study both sets of equations in this work.

Results

We perform a linear stability analysis about the laminar background flow, $\mathbf{u}_L(y) = Re\sin(y)\mathbf{e}_x$, by considering normal mode disturbances of the form $q(x,y,z,t) = \hat{q}(y)\exp[ik_x x + ik_z z + \sigma t]$. The stability of two-dimensional modes ($k_z = 0$) to infinitesimal perturbations is found to be independent of the stratification, whilst three-dimensional modes ($k_z \neq 0$) are always unstable in the limit of strong stratification ($B \to \infty$) and strong thermal diffusion ($Pr \to 0$).

The subsequent nonlinear evolution and transition to turbulence is studied numerically using direct numerical simulations (DNS). We observe that three-dimensional perturbations of the horizontal shear cause the flow to develop layers in the velocity field that generate vertical shear. For sufficiently thin velocity layers, thermal diffusion reduces the effect of stratification, allowing vertical shear instabilities to

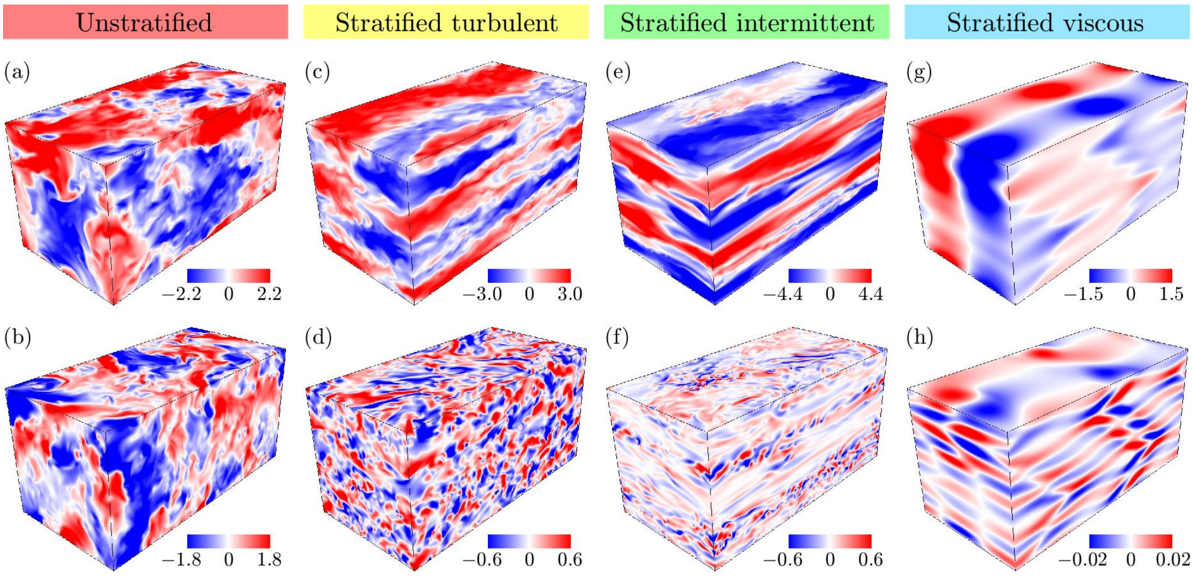

Fig. 1: Snapshots of the streamwise velocity (top) and vertical velocity (bottom) from DNSs with $Pe = 0.1$ and: (a-b) $Re = 300$, $B = 1$; (c-d) $Re = 300$, $B = 100$; (e-f) $Re = 300$, $B = 10,000$; (g-h) $Re = 50$, $B = 100,000$. Each of these examples are characteristic of a particular regime, listed along the top.

develop in between the layers at sufficiently large Re. These two effects combine to drive turbulence and can cause substantial vertical mixing. Four distinct dynamical regimes naturally emerge (illustrated in figure 1), depending upon Re and the strength of the stratification: the unstratified turbulent regime; the stratified turbulent regime; the intermittent regime and the viscous regime.

The emergence of the combined parameter BPe in the LPN equations is suggestive of its potential relevance for LPN flows. This importance is confirmed for a number of turbulent flow diagnostics, including those plotted in figure 2. For all but the largest values of BPe (which corresponds to the viscous regime), the measured vertical eddy scale l_z depends only on BPe, and scales as $(BPe)^{-1/3}$ in the stratified turbulent and intermittent regimes. Additionally, measurements of the mixing efficiency η (defined as a measure of the efficiency with which kinetic energy produced by the forcing is converted into potential energy as opposed to being dissipated viscously) allow the four regimes to be clearly identified. For intermediate stratification, the mixing efficiency plateaus at $\eta \simeq 0.4$ which, we believe, is a defining property of the stratified turbulent regime. η then decreases with well-defined scalings in the intermittent and then viscous regimes. In an analogous fashion to the approach of [4], we consider dominant balances in the governing equations, deriving scaling laws for each regime which explain the empirical observations.

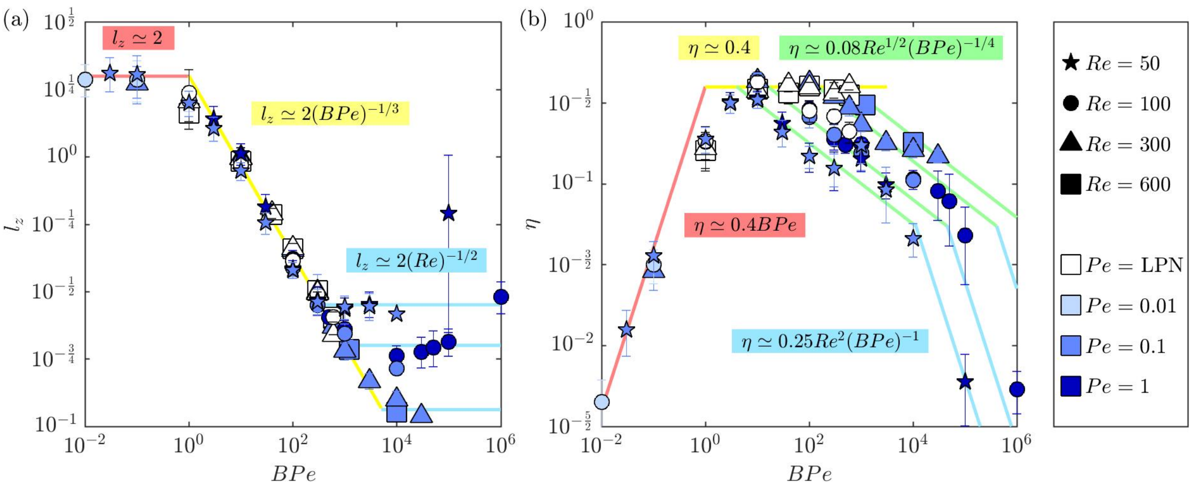

Fig. 2: Variation with BPe of (a) vertical eddy scales l_z and (b) mixing efficiency η for a variety of DNSs using the standard and LPN equations. Coloured lines illustrate scalings for the (red) unstratified, (yellow) stratified turbulent, (green) stratified intermittent and (blue) stratified viscous regimes.

References

[1] Garaud P et al. *Physics of Fluids* **27**:084104, 2015.
[2] Lucas D et al. *J. Fluid Mech.* **832**:409-437, 2017.
[3] Lignières F *Astron. Astrophys.* **348**:933-939, 1999.
[4] Brethouwer G et al. *J. Fluid Mech.* **585**:343-368, 2007.

*corresponding author: lauracope@cantab.net

On the critical electric field for Quincke electrorotation of dielectric drops

D. Das

Department of Applied Mathematics and Theoretical Physics, Centre for Mathematical Sciences, University of Cambridge, Wilberforce Road, Cambridge CB3 0WA, United Kingdom.

Introduction

Drops and particles when suspended in a fluid medium and subjected to an electric field show a rich variety of dynamics. When the ambient fluid and the suspended drop or particle are both weakly conducting, the phenomena is well described by the leaky dielectric model, first proposed by G. I. Taylor [1]. The study of such systems has come to be known as electrohydrodynamics (EHD) [2]. Of particular interest is the case when a strong uniform electric field is applied to a drop or particle less conducting than the surrounding fluid. Under these conditions, the drop or particle can undergo a symmetry breaking bifurcation and start to rotate spontaneously. This EHD instability is called as Quincke rotation first discovered by G. Quincke [3]. There has been a resurgence of interest in Quincke rotation of particles as it has proved to be an ideal system for creating active matter [4, 5, 6]. There have been experiments [7] and simulations [8] on Quincke rotation of drops as well. However, a complete theory for EHD of drops in three dimensions that predicts Quincke rotation has not been done yet. Previously, we had developed a small deformation theory of axisymmetric drops [9] using Stokes streamfunction formulation. In this work, we develop a non-linear small deformation theory for EHD of drops in three dimensions using Lamb's general solution. This allows us to derive an analytical expression for the critical electric field for Quincke rotation of drops using a linear stability analysis.

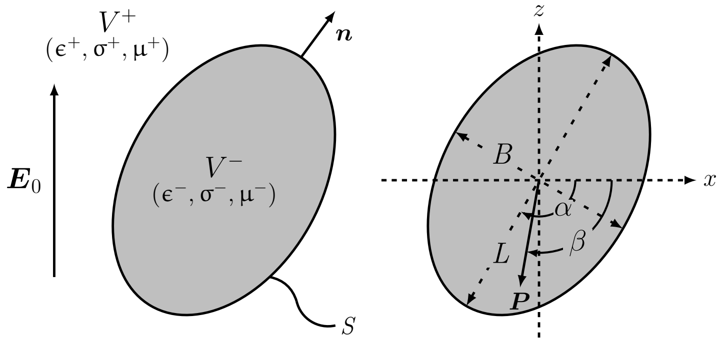

Fig. 1: A liquid droplet with surface S and outward unit normal $\boldsymbol{n}$ is suspended in an unbounded domain and placed in a uniform electric field $\boldsymbol{E}_0$ pointing in the vertical direction. $V^{\pm}$ denote the exterior and interior domains, respectively, and $(\epsilon^{\pm}, \sigma^{\pm}, \mu^{\pm})$ are the corresponding dielectric permittivities, electric conductivities and dynamic viscosities. The drop's major and minor axis lengths are denoted by L and B. The major axis and the effective dipole moment of the drop are tilted at angles α and β, respectively, with respect to the horizontal direction.

Problem definition and results

Consider an uncharged neutrally buoyant deformable drop of volume, V^-, surface, S, and outward unit normal vector, $\boldsymbol{n}$, suspended in an infinite fluid medium of volume, V^+ (see Fig. 1). The dynamic viscosity of the fluid is denoted by μ. The drop gets polarized due to the application of a uniform dc electric field, $\boldsymbol{E}_0 = E_0\hat{\boldsymbol{z}}$. We define two dimensionless numbers $R = \sigma^+/\sigma^-$ and $Q = \varepsilon^-/\varepsilon^+$ such that $RQ = \tau^-/\tau^+ > 1$ is the necessary condition for Quincke rotation to take place. In the Melcher-Taylor leaky dielectric model, all charges are concentrated on the drop surface, so that the electric potential in each domain satisfies Laplace's equation $\nabla^2\varphi^{\pm} = 0$ [2]. On the drop surface, the electric potential and the tangential component of the local electric field are continuous $[\![\varphi(\boldsymbol{x})]\!] = 0$ and $[\![\boldsymbol{E}_t(\boldsymbol{x})]\!] = \boldsymbol{0}$ for $\boldsymbol{x} \in S$, where $\boldsymbol{E}_t^{\pm} = (\boldsymbol{I} - \boldsymbol{nn})\cdot\boldsymbol{E}^{\pm}$, $\boldsymbol{E}^{\pm} = -\boldsymbol{\nabla}\varphi^{\pm}$ and $[\![f(\boldsymbol{x})]\!] \equiv f^+(\boldsymbol{x}) - f^-(\boldsymbol{x})$ denotes the jump for any field variable $f(\boldsymbol{x})$ defined on both sides of the drop surface. The normal component of the electric field $E_n^{\pm} = \boldsymbol{n}\cdot\boldsymbol{E}^{\pm}$ undergoes a jump due to the mismatch in electrical properties between the two media, resulting in a surface charge distribution given by Gauss's law, $q(\boldsymbol{x}) = [\![\varepsilon E_n(\boldsymbol{x})]\!]$ for $\boldsymbol{x} \in S$. The surface charge distribution evolves due to two distinct mechanisms, namely, Ohmic currents from the bulk, $[\![\sigma E_n]\!]$, and advection by the drop surface velocity, $\boldsymbol{v}(\boldsymbol{x})$. Accordingly, the conservation equation for the surface charge is

$$\partial_t q + [\![\sigma E_n]\!] + \boldsymbol{\nabla}_s\cdot(q\boldsymbol{v}) = 0 \quad \text{for } \boldsymbol{x} \in S, \tag{1}$$

where $\boldsymbol{\nabla}_s \equiv (\boldsymbol{I} - \boldsymbol{nn})\cdot\boldsymbol{\nabla}$ is the surface gradient operator. The fluid velocity field, $\boldsymbol{v}(\boldsymbol{x})$, and dynamic pressure, $p(\boldsymbol{x})$, satisfy the Stokes equations in the ambient and suspending fluid mediums, $-\mu\nabla^2\boldsymbol{v}^{\pm} +$

$\nabla p^{\pm} = \mathbf{0}$ and $\nabla \cdot \boldsymbol{v}^{\pm} = 0$. Dynamic boundary condition requires the electric ($\sim \epsilon^+ E_0^2$), hydrodynamic ($\sim \mu^+/\tau_{MW}$) and capillary stresses ($\sim \gamma/a$) to balance each other, written formally as,

$$[\![\boldsymbol{f}^E]\!] + Ma[\![\boldsymbol{f}^H]\!] = 2Ca_E^{-1}\boldsymbol{n} \quad \text{for } \boldsymbol{x} \in S, \quad Ca_E = \frac{a\epsilon^+ E_0^2}{\gamma}, \qquad Ma = \frac{\mu^+}{\epsilon^+ \tau_{MW} E_0^2} \tag{2}$$

The drop's surface is defined as $\xi \equiv r = 1 + \delta f(t, \theta, \phi)$ where θ and ϕ are the polar and azimuthal angles, respectively, and $\delta \sim Ca_E$ is a small parameter. Lastly, we need to specify the kinematic boundary conditions, $\boldsymbol{v}^+ = \boldsymbol{v}^- = \dot{\xi}\hat{\boldsymbol{r}}$. The non-dimensional charge conservation equation then reads,

$$\frac{\partial q}{\partial t} + \frac{Q+2}{1+2R}(RE_n^+ - E_n^-) + \frac{1}{Ma}\nabla_s \cdot (q\boldsymbol{v}) = 0. \tag{3}$$

We only consider terms to the leading order in $\mathcal{O}(Ma^{-1})$, which means that the electric problem is solved by an induced dipole moment $\boldsymbol{P}$ only and higher multipoles arising from non-linear charge convection term can be neglected. We then find the electric stresses generated by the electric dipole in spherical coordinates. Next, using Lamb's general solution for the flow field and hydrodynamics tractions, we solve the flow problem. After some tedious algebra and manipulations, the unknown flow-field and shape (f) coefficients are related to the dipole moments, $\boldsymbol{P} = [P_x, P_y, P_z]$, by using the dynamic and kinematic boundary conditions. This reduces the charge conservation equation to three non-linear coupled ODEs involving only the dipole moment components which can be numerically computed to solve the complete EHD drop problem. We can then perform a linear stability analysis around the no-rotation base state to find the critical electric field for Quincke rotation of drops given as,

$$\frac{E_{c,\mathrm{drop}}}{E_{c,solid}} = \frac{1}{1 - 2\mathcal{G}(\lambda, R, Q) - \mathcal{H}(\lambda, R, Q)\frac{2(1+2R)(Q+2)}{3(RQ-1)}}, \text{ where } E_{c,solid} = \sqrt{\frac{2\mu^+(Q+2)(1+2R)}{3\epsilon^+\tau_{MW}(RQ-1)}}, \tag{4}$$

and the expressions of $\mathcal{G}, \mathcal{H}$ are not provided here for brevity. The expression for the critical electric field of Quincke rotation of drops was first given by T. B. Jones [10].

The ODEs for the dipole moment $\boldsymbol{P} = [P_x, 0, P_z]$ are advanced in time to reach a steady state solution and a phase diagram for Taylor regime (no rotation, red circles) and Quincke regime (rotation, blue squares) are shown in Fig. 2(a). The expression for critical electric field, (4) is also plotted (black dashed line). We find that the critical electric field for Quincke rotation of drops increases with drop viscosity, in qualitative agreement with experimental results [7] (shown in green triangles and purple diamonds). As expected, the agreement is better for smaller and more viscous drops. The tilt angle of the major axis (α) and dipole moment (β) is seen to undergo pitchfork bifurcation, Fig. 2(b). For a given viscosity ratio and electric field strength, the tilt angle α is found to be higher than the dipole tilt angle. The dipole moment tilt angle of a solid particle ($\lambda \to \infty$) is also shown in black solid line.

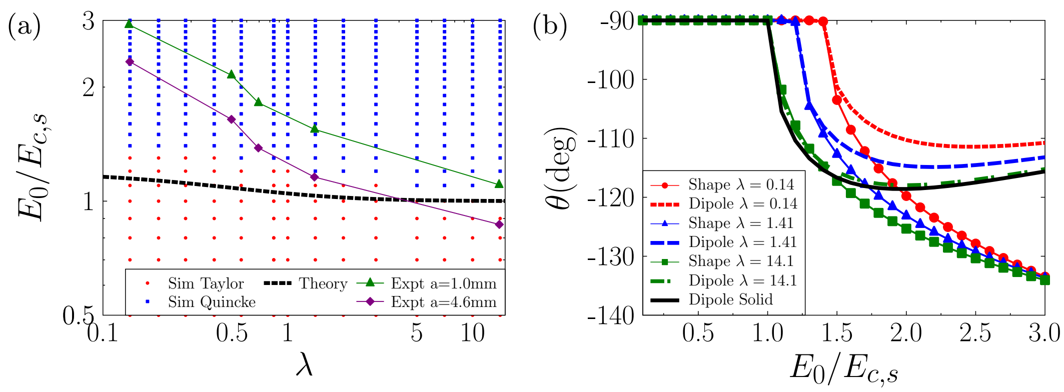

Fig. 2: (a) Phase diagram separating Taylor (no-rotation) and Quincke (rotation) regimes. (b) Pitchfork bifurcation of drop major axis (α) and dipole moment (β) tilt angles for three different viscosity ratios.

We thank John Lister and David Saintillan for helpful discussions.

References

[1] Taylor G. I. , *Proc. R. Soc. Lond. A* **291**:159–166, 1966.
[2] Melcher J. R. and Taylor G. I. , *Annu. Rev. Fluid Mech.* **1**:111–146, 1969.
[3] Quincke G. , *Ann. Phys. Chem.* **59**:417–486, 1896.
[4] Bricard A. et al. , *Nature* **503**:95–98, 2013.
[5] Das D. and Lauga E. , *Phys. Rev. Lett.* **122**:194503, 2019.
[6] Karani H. et al. , *Phys. Rev. Lett.* **123**:208002, 2019.
[7] Salipante P. F. and Vlahovska P. M. , *Phys. Fluids* **22**:112110, 2010.
[8] Das D. and Saintillan D. , *J. Fluid Mech.* **829**:127–152, 2017.
[9] Das D. and Saintillan D. , *J. Fluid Mech.* **810**:225–253, 2017.
[10] Jones T. B. , *IEEE Trans. Ind. Appl.* **20**:845–849, 1984.

*corresponding author: dd496@damtp.cam.ac.uk

Coating Flows down a Vertical Fibre: the full Navier-Stokes problem

Z. Ding[1]* and R. Liu[2]

[1]Department of Applied Mathematics and Theoretical Physics, University of Cambridge, Wilberforce Road, Cambridge CB3 0WA, United Kingdom
[2]School of Mechanical and Electrical Engineering, Gui Lin University of Electronic Technology, Gui Lin 541004, China

Introduction

The dynamics of a coating film flow on the surface of a cylindrical fibre has been extensively studied in the past decades. Of particular interests, Kliakhandler *et al.* [1] carried out experimental studies of thick film flows down a vertical thin fibre. Three distinct flow regimes, labeled as "a", "b", "c", were reported. The droplets in flow regime "a" are separated by a long thin film, which propagate at a constant speed. Flow regime "b" is a necklace-like flow, in which the droplets are short-spaced. The flow regime "c" is operated at very low flow rate ($\sim 5mm^3/s$), and a large droplet is observed to coexist with several tiny beads.

To investigate the dynamics of the three different flow regimes, all the previous works employed a reduced-order model based on the long-wave assumption [1, 2, 3, 4, 5]. The flow regime "a" has been well understood by the long-wave models [2, 3]. All these models, however, failed to capture the dynamics of the flow regime "b" which is essentially a short-wave regime. And the gap between the experimental measurement and theoretical prediction by these reduced-order models on the wave speed of the flow regime "c" is large (a discrepancy of $\sim 30\%$).

To address the dynamics of flow regime "b" and improve the prediction of wave speed of flow regime "c", we drop the long-wave assumption and track the travelling wave solutions of the Navier-Stokes equations, which are compared with the experimental data of flow regimes "a", "b" and "c" (see figure 1). The flow regime "c" is a time-periodic state and was suggested to be represented by a relative periodic orbit [5]. It is more challenging to find the relative periodic orbits of the Navier-Stokes equations. Here, we only report the travelling wave solution using the parameters of flow regime "c". By comparing with the experimental measurements, we show that our numerical results well capture both the long-wave dynamics in flow regime "a" and short wave dynamics in flow regime "b". In addition, the gap in the wave speed between the theoretical prediction and the experimental measurement is reduced to $\sim 10\%$.

Numerical method

We consider an axisymmetric flow and adopt the same non-dimensional scales as Craster and Matar [2]. Then, we directly start from the dimensionless governing equations:

$$\partial_r u + \frac{u}{r} + \partial_z w = 0, \tag{1}$$

$$\epsilon^4 La(\partial_t u + u\partial_r u + w\partial_z u) = -\partial_r p + \epsilon^2 \left[\partial_{rr} u + \frac{\partial_r u}{r} - \frac{u}{r^2} + \epsilon^2 \partial_{zz} u\right], \tag{2}$$

$$\epsilon^2 La(\partial_t w + u\partial_r w + w\partial_z w) = 1 - \partial_z p + \partial_{rr} w + \frac{\partial_r w}{r} + \epsilon^2 \partial_{zz} w, \tag{3}$$

where $La = \rho\gamma R/\mu^2 \sim O(1)$ is the Laplace number and $\epsilon = \rho g R^2/\gamma \sim 0.3$ (ρ is the density, γ is the surface tension, R is the mean radius of the liquid film and μ is the dynamic viscosity). There is no slip boundary condition at the fibre wall and stress is balanced by the surface tension at the liquid surface [2].

We map the domain into a rectangular region $\tilde{r} \times \tilde{z} = [0, 1] \times [0, L]$, by introducing the following coordinate transformation

$$t = \tilde{t}, \quad z = \tilde{z}, \quad r = h(\tilde{z}, \tilde{t})\tilde{r} + a, \tag{4}$$

where h is the thickness of the film. In the radial direction, we used Chebyshev-collocation method and a fast Fourier transform is applied in the axial direction. We used a simulation-based approach to find the recurrent solutions (travelling waves) of the Navier-Stokes equations. Here, we report our study of the three typical flow regimes in experiments.

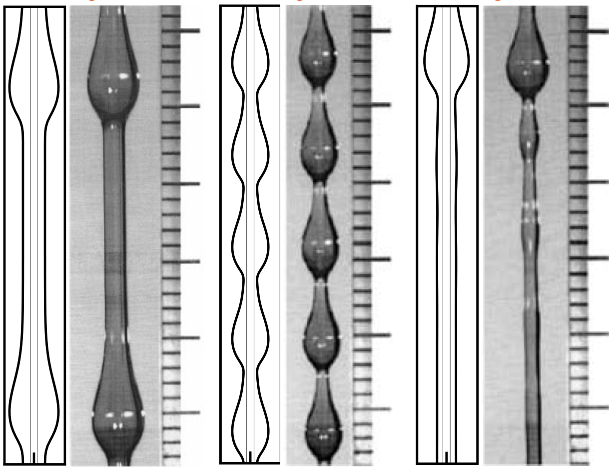

Fig. 1: The comparison between the travelling wave solution of the full Navier-Stokes equation and the experimental observation (adapted from [1]). The parameters for our simulations are the same as the experimental study in [1].

	Regime "a" $(c,\, R_{max})$	Regime "b" $(c,\, R_{max})$	Regime "c" $(c,\, R_{max})$
Experiment	(1.1698, 1.76)	(0.3200, 1.45)	(0.9318, 1.89)
Craster & Matar	(1.195, 1.796)	(0.6560, 1.76)	(1.36, 2.17)
Novbari & Oron	(1.357, 1.61)	(0.54, 1.53)	(1.48, 1.88)
Present	(1.178, 1.70)	(0.51, 1.39)	(1.08, 1.95)

Table 1: The comparison between the experimental measurements and different models. All the wave speeds c are nondimensionalised by $\rho R^2 g/\mu$. R_{max} is the maximal dimensionless radius of the traveling wave which is nondimensionalised by R.

Discussions

For the flow regime "a", all the long-wave models and our present study compare well with the experimental data, which demonstrates that the long-wave assumption is justified. For the flow regime "b", the long-wave model in [2], which neglected the inertial effect, shows a very poor agreement with the experimental result. The predicted wave speed c is about twice of the measured value. In [4], the inertial effect was considered and modeled by an energy integral method, which improved the prediction of the wave speed. We further improve the prediction of the wave speed by solving the full Navier-Stokes equations (see table 1). However, Novbari & Oron showed that the inertia effect included in their energy integral model deteriorates the prediction of wave speeds in flow regime "a" and "c". This implies that the streamwise dissipation effect – neglected in [2, 4]– should play an important role in balancing the inertia effect, which is reflected by our travelling wave solution of Navier-Stokes equations of the flow regime "a" and "c". For the flow regime "c", the present predicted wave speed is 1.08, which significantly improves all the previous theoretical results. As suggested in [5] that the relative periodic orbit travels a bit slower than the steady traveling wave, we conjecture that the wave speed $c = 1.08$ can be slightly reduced further by solving the relative periodic solution of the Navier-Stokes equations.

References

[1] Kliakhandler I.L. Davis, S. and Bankhoff S. *J. Fluid Mech.* **429**:381-390, 2001.
[2] Craster R. Matar O. **553**, 85-105, 2006.
[3] Ruyer-Quil C., Treveleyan P., Giorgiutti-Dauphiné F. & Kalliadasis S. *J. Fluid Mech.* **603**, 431-462, 2008.
[4] Novbari E. & Oron A. *Phys. Fluids* **21**, 062107, 2009.
[5] Ding Z. & Willis A. *J. Fluid Mech.* **873**, 835-855, 2019.

*corresponding author: z.ding@damtp.cam.ac.uk

On the nature of turbulent motions at small scale

B. Dubrulle[1]*

[1]SPEC, Universite Paris-Saclay, CNRS, CEA, F-91191 Gif sur Yvette Cedex, France

In 1949, Batchelor and Townsend[1] speculated about the nature of small scale turbulent motions on the basis of hot wire velocity measurements in the Cavendish wind tunnel. Their main conclusion was that the energy associated with small scales is intermittent in space and time and organized into strong discrete vortices. Since then, progresses in computer power and image velocimetry has made it possible to investigate in more detail the nature and the properties of small scale turbulent motions, at scales of the order of or below the Kolmogorov scale. For example, it is now well established that regions where the vorticity supersedes the strain (the so-called Q criterion) are indeed organized into small scale elongated coherent structures that display a complex dynamics [2]. In some circumstances, they may interact and reconnect iteratively, following a self-similar vortex reconnection cascade. During reconnection, a distinct $-5/3$ inertial range is observed for the kinetic energy spectrum, associated with numerous resulting fine-scale bridgelets and thread filaments [3].

In the mean time, theoretical models of vortex reconnection using Biot-Savart model have evidenced a self-similar process, resulting in a near finite time singularity at the apex of the tent formed by the vortices[4]. Another evidence for quasi blow-up is provided by the ”zeroth law of turbulence” [6], according to which the non-dimensional energy per unit mass become constant at large Reynolds number, implying a blow up of the entsrophy in the limit of zero viscosity. This suggests that the small scale structure of turbulent motions is very irregular, and calls for specific tools to analyze them. A suitable tool to deal with them was invented by [5] and named ”weak formulation”. The main idea is to make a detour via the scale space, and work with smoothed version of the initial field (a ”mollified” field), over a characteristic scale (resolution) ℓ. At any given resolution ℓ, the mollified field is sufficiently regular, so that all classical tools and manipulation of analysis of vector fields are valid. Limiting behaviors as resolution $\ell \to 0$ can then be used to infer results and properties for the rough field.

In this talk, I show how these fields can be used to build two scalar fields, that encode the regularity properties of the small scale motions: i) a pseudo-Holder exponent $\tilde{h}(\mathbf{x})$ built using the *Wavelet Transform Modulus Maxima* method and providing the best local estimate of Hölder regularity compatible with the global multi-fractal analysis [7]; ii) a local energy transfer $|D_\ell^I(\mathbf{x})|$ built from the Navier-Stokes using energy balance for weak solution [8, 9]. Example of such scalar fields computed in a Direct Numerical Simulation of Navier-Stokes equations is shown in Fig. 1 , along with the corresponding vorticity field. I show that $\tilde{h}(\mathbf{x})$ and $|D_\ell^I(\mathbf{x})|$ are globally statistically correlated, but that local maxima of $|D_\ell^I(\mathbf{x})|$ do not coincide exactly with local minima of $\tilde{h}(\mathbf{x})$. Finally, I discuss how these scalar fields can be used to infer interesting informations about the small scale dynamics.

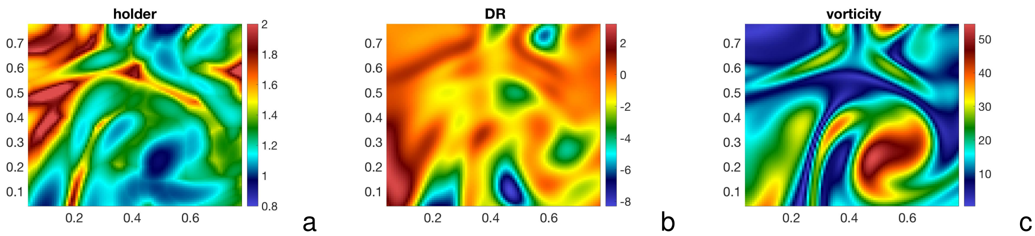

Fig. 1: (a) pseudo-Holder exponent; (b) local energy transfer and (c) vorticity field computed from the velocity field obtained using direct numerical simulation of Navier-Stokes equation.

Acknowledgement

This work has been done within the ANR EXPLOIT, grant agreement no. ANR-16-CE06-0006-01, with T. Chaabo, A. Cheminet, Ch. Cuvier, F. Daviaud, P. Debue, D. Geneste, J-M. Foucault, J-Ph. Laval, Y. Ostovan, V. Padilla, V. Valori, C. Wiertel , for the experimental part, and in collaboration with F. Nguyen, H. Faller, D. Kuzzay, D. Faranda, A. Cheskidov, R. Svydkoy, J-Ph. Laval, C. Nore , J-L. Guermond, L. Cappanera, A. Harekrishnan and N. Vercauteren for the numerical and theoretical part, using access to the HPC resources of IDRIS under the allocation GENCI-IDRIS 2A10096 and 2018-0254 in France and by the Texas A&M University Brazos HPC cluster. This work was also supported by fund from the ANR, project ECOUTURB ANR-16-CE30-0016.

References

[1] Batchelor G. K. & Townsend A.A, . *Proc. of the Royal Soc. of London. Series A.* **199-1057** 238-255, 1949.

[2] Vincent, A. & Meneguzzi, M. *J. Fluid Mech.* **258** 245-254, 1994 .

[3] Yao, J. & Hussain, F. *J. Fluid Mech.* **883** A51 1-36, 2020.

[4] Kimura, Y. & Moffatt, H.K. *J. Fluid Mech.* **834** R1, 2018.

[5] Leray, J. *Acta Math.* **63,** 193248, 1934.

[6] Frisch, U. *Turbulence, the legacy of A.N. Kolmogorov.* Cambridge University Press, 1995.

[7] Nguyen, F. et al. *Physical Review E*, **99**, 053114, 2019.

[8] Kuzzay, D. et al., *Nonlinearity* **30**, 2381 2017.

[9] Dubrulle, B. *J. Fluid Mech*, **867**:1, 2019

*corresponding author: berengere.dubrulle@cea.fr

Seeking the origin of intermittence in turbulent flows.

H. Faller[1,2*], P. Debue [1], T. Chaabo[3], D. Geneste[1], V. Valori [1], A. Cheminet[3], Y. Ostovan[3], L. Cappanera[4], Ch. Cuvier[3], F. Daviaud [1], J-M. Foucaut[3], J-L. Guermond[5], J-P. Laval[3] C. Nore[2], C. Wiertel[1] V. Padilla[1] B. Dubrulle[1]

[1]SPEC/IRAMIS/DSM, CEA, CNRS, Université Paris-Saclay, CEA Saclay, 91191 Gif-sur-Yvette, France. [2]Laboratoire d'Informatique pour la Mécanique et les Sciences de l'Ingénieur, LIMSI, CNRS, Univ. Paris-Sud, Université Paris-Saclay, Bâtiment 508, rue John von Neumann, Campus Universitaire, F-91405 Orsay, France [3]Univ. Lille, CNRS, ONERA, Arts et Métiers ParisTech, Centrale Lille, FRE 2017-LMFL-Laboratoire de Mécanique des Fluides de Lille-Kampé de Fériet, F-59000, Lille, France [4]Department of Mathematics, University of Houston, Houston, TX 77204-3008, USA [5]Department of Mathematics, Texas A&M University 3368 TAMU, College Station, TX 77843-3368, USA

In 1949, Batchelor and Towsend[1] published the first experimental account about inconsistencies in the original turbulence theory of Kolmogorov[2]. Measuring various flatness of the distribution of velocity derivatives, $\alpha(n) = \overline{\left(\frac{\partial^n u}{\partial x^n}\right)^4} / \left[\overline{\left(\frac{\partial^n u}{\partial x^n}\right)^2}\right]^2$, they observed an increase of α both with n and with the Reynolds number Re. Their interpretation was that $\partial^n u/\partial x^n$ fluctuates in a manner that is more markedly intermittent as n or Re increase, a fact confirmed by oscillograms of the velocity field derivatives. The finding was summarized in a remarkable concise but visionary paragraph stating that "*energy associated with large wave-number is very unevenly distributed in space. There appear to be isolated regions in which the large wave-numbers are 'activated', separated by regions of comparative quiescence. This spatial inhomogeneity becomes more marked with increase in the order of the velocity derivative, i.e. with increase in the wave-number. It is suggested that the spatial inhomogeneity is produced early in the history of the turbulence by an intrinsic instability, in the way that a vortex sheet quickly rolls up into a number of strong discrete vortices. Thereafter the inhomogeneity is maintained by the action of the energy transfer.*"

The result of Batchelor and Townsend only concerns intermittency at the dissipative scales. The Kolmogorv 1962 [3] refined theory allows to connect intermittency of the local energy dissipation with (intermittent) correction to scaling of the energy spectrum, or of the velocity structures functions up to the inertial scales. In this picture, there is a direct link between the 'active' regions of intense local dissipation, and the intermittent corrections to scaling. Because the areas of intense dissipation are observed to arise in the vicinity of vorticity filaments [4], or sheets [5], there have been several attempts to link intermittency exponents, and vorticity coherent structures [6, 7], by conditioning statistics upon areas of low or high vorticity. The conclusion is that the coherent structures do affect the intermittency by acting on the way the cascade develops. This means that -as suggested by Batchelor- the vorticity is not the only important ingredient of the intermittency, and that energy transfers should be somehow take, into account.

With this in mind, we use the following scale-by-scale energy balance derived from Duchon & Robert [8]:

$$\partial_t E^\ell(\mathbf{x},t) + \nabla \cdot \mathbf{j}^\ell(\mathbf{x},t) = -\Pi^\ell_{\mathrm{DR}}(\mathbf{x},t) - \Pi^\ell_\nu(\mathbf{x},t). \tag{1}$$

Where E^ℓ is the kinetic energy at scale ℓ; $\mathbf{j}^\ell$ is a spatial transport term; Π^ℓ_{DR} corresponds to the local instantaneous energy flux towards scales smaller than ℓ due to non linear interactions; and Π^ℓ_ν is the viscous dissipation at scale ℓ.

A direct link between intermittent exponent and instantaneous partial local energy transfer at the Kolmogorov scale ($\ell = \eta$) was found in an experimental turbulent swirling flow using conditional statistics [9]. At this time, only velocity measurements on a plane were available, meaning that a fraction of the local energy transfer was missing, and that the vorticity field could not be computed, preventing investigation of possible correlations between local energy transfers, and properties of intense vorticity regions. Thanks to an outstanding experimental and numerical effort, we now have at our disposal both 3D time and space resolved velocity measurements (fig 1) and numerical (fig 2) data in the same geometry [10, 11]. Experimental measurements with particle image velocimetry (PIV) provide a lot of data in a small volume, and are often are subject to noise. They make it possible to obtain the statistical properties of the tools used, but they do not easily lead to a good characterization of the observed structure. Direct numerical simulations provide access to data sets that are well resolved in space, but limited in time, which makes it difficult to obtain good statistical properties. On the other hand, the data are smooth enough perform accurate computations of quantities such as helicity, enstrophy, or the eigenvalues of the velocity gradient.

A mixed experimental and numerical approach enables to benefit from the advantages of each method. The goal of the presentation is thus to gather all results, and invsetigate how much local energy transfers and vorticity are correlated in between them, and with intermittent corrections to scaling.

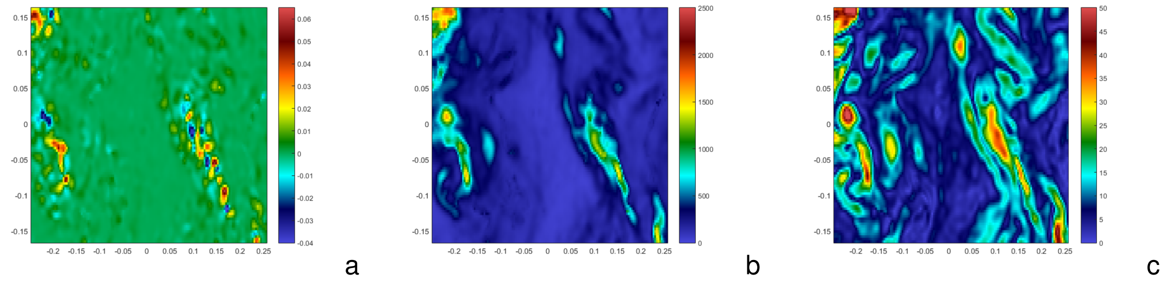

Fig. 1: Π^{ℓ}_{DR} (a), Π^{ℓ}_{ν} (b) and $\|\omega\|$ (c) in an experimental turbulent von Kàrmàn flow.

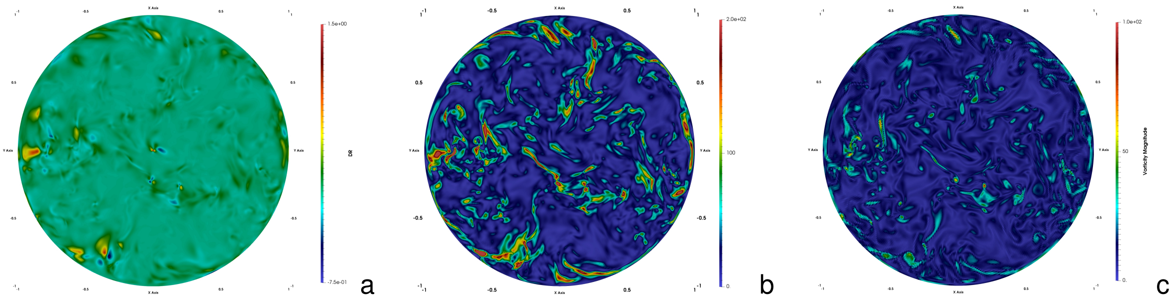

Fig. 2: Π^{ℓ}_{DR} (a), Π^{ℓ}_{ν} (b) and $\|\omega\|$ (c) in a numerical turbulent von Kàrmàn flow.

References

[1] Batchelor G. K. et al. *The nature of turbulent motion at large wave-numbers*. Proc. of the Royal Soc. of London. Series A. **199**-1057: 238-255, 1949.

[2] Kolmogorov, A.N. *The local structure of turbulence in incompressible viscous fluids for very large Reynolds number*. Dokl. Akad. Nauk SSSR [Sov. Phys.-Dokl.], **30**, 913, 1941.

[3] Kolmogorov, A.N. *A refinement of previous hypotheses concerning the local structure of turbulence in a viscous incompressible fluid at high Reynolds number*. J. Fluid Mech. **13** 82, 1962.

[4] Vincent A., and Meneguzzi M. *The dynamics of vorticity tubes in homogeneous turbulence*. J. Fluid Mech. **258**: 245-254, 1994.

[5] Moisy F. and Jimenez J. *Geometry and clustering of intense structures in isotropic turbulence*. J. Fluid Mech. **513**: 111-133, 2004.

[6] Chainais P. et al. *Intermittency and coherent structures in a swirling flow: A wavelet analysis of joint pressure and velocity measurements*. Phys. Fluids **11**-11:3524-3539, 1999.

[7] Paret J. *Intermittency in the two-dimensional inverse cascade of energy: Experimental observations*. Phys. Fluids **10**-12:3126-3136, 1998.

[8] Duchon, J. and Robert, R. *Inertial energy dissipation for weak solutions of incompressible Euler and NavierStokes equations.* Nonlinearity **13**-1: 249-255, 2000.

[9] Dubrulle, B. *Beyond Kolmogorov cascades*. J. Fluid Mech, **867**:1, 2019

[10] Cappaneira L. et al. *Turbulence in realistic geometries with moving boundaries: when simulations meet experiments*. Under consideration at J. Comp. Fluid.

[11] Debue P. et al. *Dissipation, intermittency, and singularities in incompressible turbulent flows*. Phys. Rev. E **97** 053101, 2018.

*corresponding author: hugues.faller@normalesup.org

Beyond statistically homogeneous turbulence

Marie Farge[1]*

Ecole Normale Supérieure, 24 rue Lhomond 75231 Paris Cedex 5, France
[1] CNRS/INSMI, LMD/IPSL, ENS/PSL, Sorbonne Université, Ecole Polytechnique/IP Paris

I will explain why I think that the statistical theory of homogeneous turbulence is based on unrealistic assumptions and that the observables it uses are not reliably measurable in practice.

At a workshop I organised in 1997 at UC Santa Barbara, Hans Liepmann concluded his presentation by saying that: *'As long as we are not able to predict the drag on a sphere or the pressure drop in a pipe assuming a continuous, incompressible, Newtonian fluid, without any further complications (namely from first principles), we will not have made it!'*. Consequently, I decided to take up this challenge by focusing on the study of turbulent wakes generated by different types of obstacles, fixed or mobile, and on the production of turbulence by solid walls.

I will present few results obtained, in collaboration with Kai Schneider, Dmitry Kolomensky, Natacha Nguyen van yen and Thomas Engels, by using direct numerical simulation [1] to study how insects fly in the presence of turbulence (see Figure 1 and [2]), and how boundary layers take off when a dipole hits a solid wall (see Figure 3 and [3]).

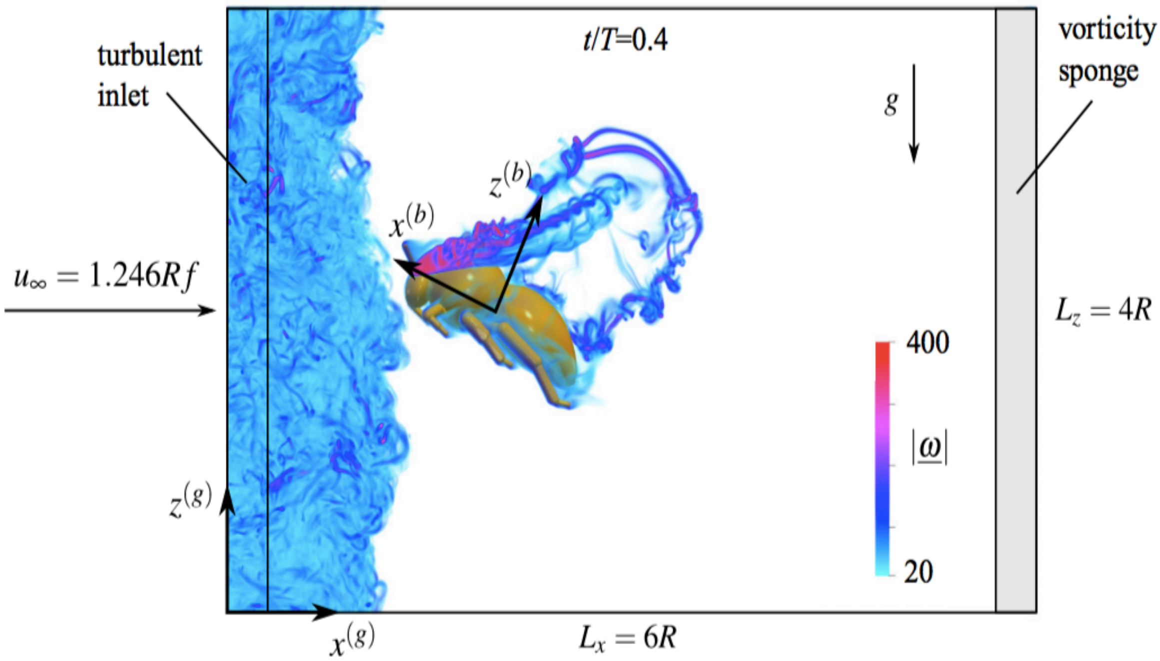

Fig. 1: Direct numerical simulation of a bumblebee flying in a turbulent flow [2].

References

[1] Engels T et al., *arXiv*, 1912.05371v1 [math.NA], 2019.
[2] Engels T et al., *Phys.Rev. Fluids*, **4**:013103, 2019.
[3] Nguyen van yen N *et al.*, *J. Fluid Mech.*, **849**:676-717, 2018.

*corresponding author: marie.farge@ens.fr

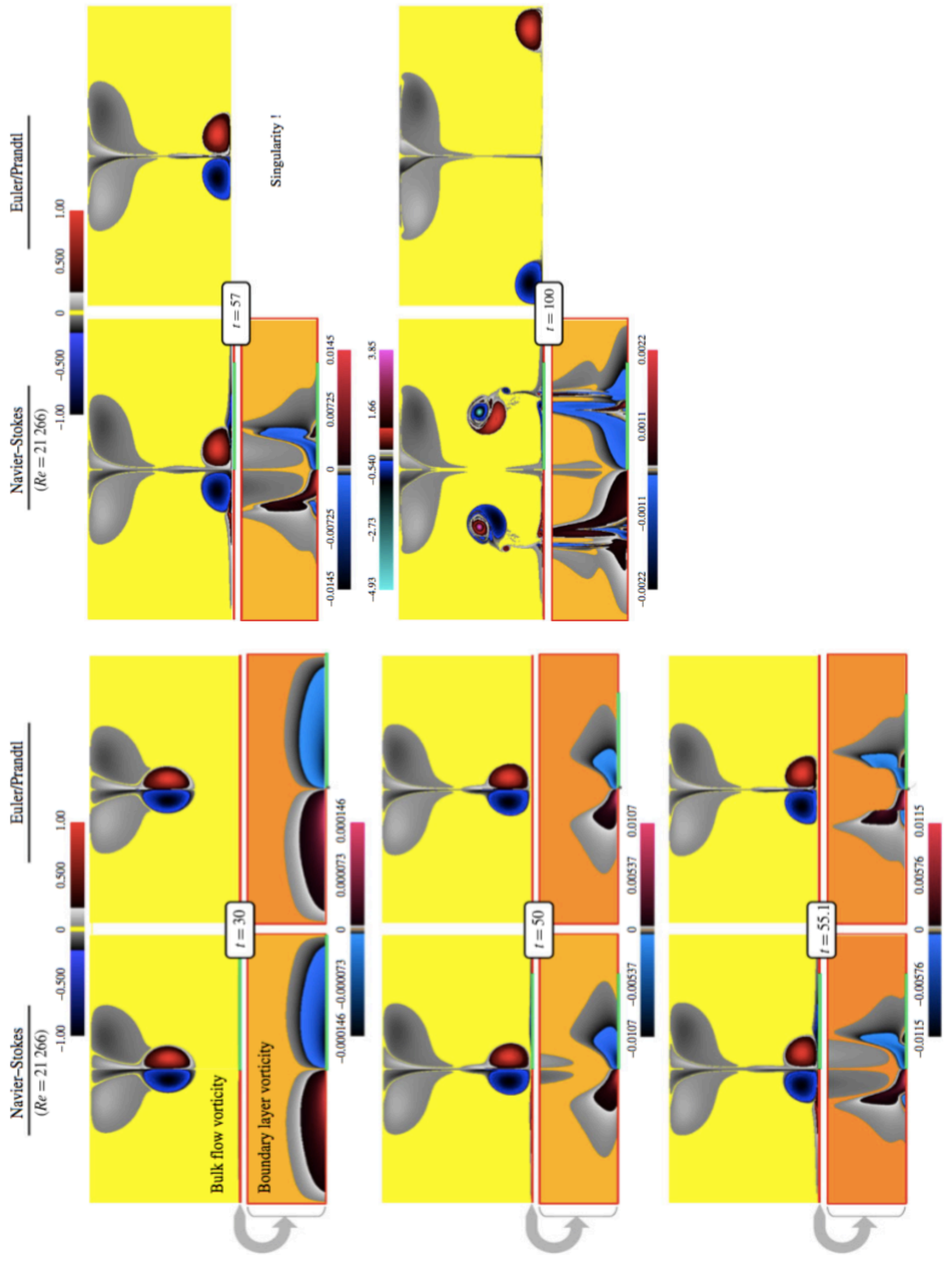

Fig. 2: Direct numerical simulation of a dipole impacting a wall : comparison between Euler/Prandtl and Navier-Stokes solutions [3].

The frictional transition in shear thickening suspensions: from rheology to hydrodynamics

C. Clavaud[1], B. Darbois-Texier[1], A. Bérut[1], H. Lhuissier[1], B. Metzger[1], Y. Forterre[1]*

[1]Aix Marseille Univ, CNRS, IUSTI, 13453 Marseille, France

Introduction

In a landmark paper published in 1972, G.K. Batchelor and J.T. Green determined the first analytic correction in volume fraction to the famous Einstein formula for the effective viscosity of a dilute suspension of hard spheres [1]. In this paper, they considered pair hydrodynamic interactions as a first step to describe more concentrated suspensions. However, understanding the very concentrated regime, where both hydrodynamics and contact interactions are present, still represents a challenge [2]. One of the most intriguing phenomenon observed in some very dense suspensions is the dramatic increase of the viscosity above a critical shear-rate, called shear-thickening. Recently, discrete numerical simulations and theoretical works have proposed that shear-thickening results from a frictional transition, due to the existence of a short-range repulsive force between particles [3, 4]. In this paper, we summarize recent works we conducted to investigate this frictional transition mechanism and its consequence on the flow of shear thickening suspensions.

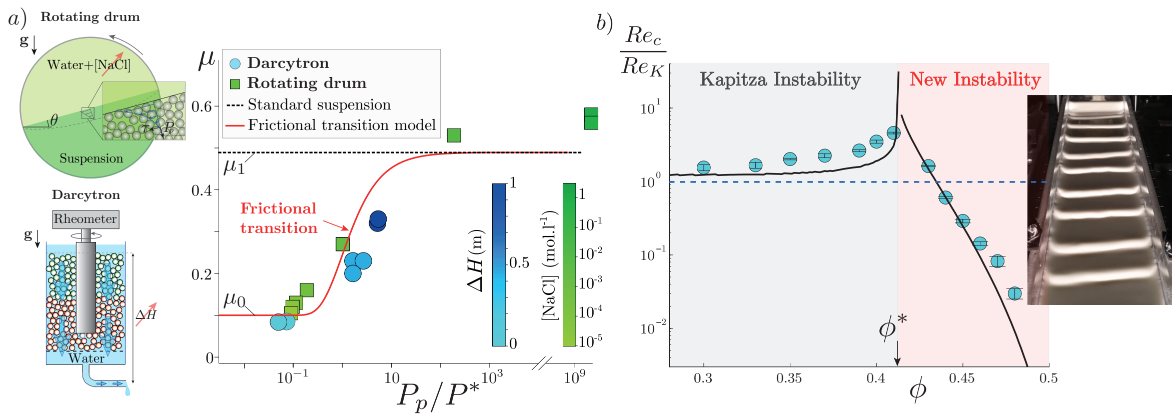

Fig. 1: a) Evidence of the frictional transition in a model shear-thickening suspension made of silica particles ($d = 23.56$ μm, density $\rho_p = 1850$ kg/m^3) in water or ionic solution [NaCl]. As the ratio of the particle pressure to the repulsive pressure increases, the macroscopic friction coefficient of the suspension goes from $\mu \approx 0.1$, the predicted value for frictionless spheres, to $\mu \approx 0.5$, corresponding to frictional spheres. b) Surface instability observed when a concentrated shear thickening suspension flows down an inclined plane (cornstarch in water, $\phi = 0.45$, inclination $\theta = 10°$, layer thickness $h = 7.5$ mm).

Testing the frictional transition model using pressure-imposed rheology

The frictional transition model is based on the fact that the contact interactions between particles switch from frictionless to frictional depending on the applied stress. Testing the model thus requires to access the frictional property of the suspension, which is not possible using conventional rheometry performed at constant volume fraction. To circumvent this difficulty, we proposed two different approaches in which the particle stress is imposed, not the volume fraction. In the first approach, we studied the quasi-static avalanche angle θ of a pile of non-buoyant repulsive particles immersed in liquid in a slowly rotating drum [5] (Fig. 1a). In this configuration, both the shear stress τ and the particle pressure P_p are fixed and imposed by the weight of the flowing layer of grains at the top of the pile. Consequently, the frictional state of the suspension can be directly inferred from the avalanche angle since $\mu = \tau/P_p = \tan\theta$. We used a suspension made of non-Brownian silica beads in water or ionic solution [NaCl], in which the repulsive force originates from the electrostatic Debye double-layer. By changing the salt concentration, we were able to tune the repulsive pressure P^* between particles and evidence the transition between a 'frictionless' suspension to a 'frictional' suspension as P^* decreases. Moreover, we confirmed that shear thickening can only be observed with the suspension having a frictionless state at low stress, in agreement with the frictional transition model [5]. To complement these results, we developed a pressure-imposed device, called Darcytron, that enables us to vary the particle pressure P_p [6]. The idea is to shear a non-buoyant granular suspension in a large gap Couette geometry and to add, in addition to gravity, a vertical Darcy flow across the settle bed of particles (Fig. 1a). The total vertical stress P_p acting on the particles can then be changed by varying the intensity of the Darcy flow, while the shear stress τ is obtained from the torque, yielding the friction coefficient $\mu = \tau/P_p$. Using this setup, we were able to demonstrate that varying the particle pressure induces a frictional transition in the shear thickening suspension of silica beads in pure water. Moreover, data of the suspension friction coefficient $\mu = \tau/P_p$ as function of the dimensionless particle pressure P_p/P^* for both experiments with the rotating drum and the Darcytron collapse on a single master curve, in agreement with the frictional transition model (Fig. 1a).

Consequence on hydrodynamics: Surface instability down inclined planes

We next investigated the consequence of this frictional transition on the flow of shear-thickening suspensions in hydrodynamic configurations. When a thin layer of a concentrated cornstarch suspension flows down an inclined plane, the free surface rapidly breaks up in a series of regular waves propagating downstream (Fig. 1b) [7]. This instability is reminiscent of the Kapitza instability that occurs when a Newtonian fluid flows down a slope [8]. However, the Kapitza instability is an inertial instability arising above a critical Reynolds number $Re_K = 5/(6\tan\theta)$, while here the Reynolds number is much lower: $Re = 0.2 \ll Re_K = 5$ ($\theta = 10°$), suggesting a new kind of instability [7]. To confirm this, we systematically measured the instability onset for a wide range of volume fractions. Below a critical volume fraction $\phi^* = 0.41$, we recover the classical Kapitza instability, with a critical Reynolds number that slightly increases with the volume fraction as expected for a continuous shear-thickening rheology [9]. However, for $\phi > \phi^*$, the critical Reynolds number starts to drop drastically, reaching values two order of magnitude below the Kapitza threshold at large volume fractions. We have shown that this new instability actually corresponds to the onset of discontinuous shear-thickening and the emergence of 'S-shape' flow curves in the rheology $\tau(\dot\gamma)$, with a region of negative slope ($A = d\dot\gamma/d\tau < 0$) for $\tau > \tau^*(\phi)$. To show this, we note that in the absence of inertia, the linearized depth-averaged mass and momentum balances reduce to:

$$\frac{\partial h}{\partial t} + c_K \frac{\partial h}{\partial x} = \frac{A}{\tan\theta}\frac{\partial^2 h}{\partial x^2} \tag{1}$$

where h is the flow thickness and $c_k = 2 + A$ is the speed of the kinematic waves ($k \to 0$). One recognizes a diffusion equation in the reference frame of the kinematic waves, which is unstable when $A < 0$. A full linear stability analysis of the depth-averaged equations taking into account inertia and the Wyart-Cates constitutive law for shear-thickening suspensions [4] enabled us to predict both the classical Kapitza instability at low volume fraction and the new low Reynolds number instability above $\phi > \phi^*$ related to the 'S-shape' rheology (Fig. 1b).

Conclusion

Overall, our results support the frictional transition framework recently proposed to explain shear-thickening in certain dense suspension of particles. The key ingredient compared to standard suspensions of macroscopic particles lies in the existence of a short-range repulsive force between particles, which introduces a new force scale in the problem. Under low stress, the interparticle force repels particles and thus prevents solid frictional contacts between them, yielding a suspension of low viscosity. Under large stress however, the repulsive force becomes negligible and solid frictional contact can occur, yielding a suspension with a much larger viscosity. We have seen how this frictional transition strongly affects the rheology of dense suspensions and induces new hydrodynamic instabilities, that have no counterpart in classical fluids.

References

[1] Batchelor GK & Green JT. J. Fluid Mech., 56: 401-427, 1972.
[2] Guazzelli E & Pouliquen O. J. Fluid Mech., 852: P1, 2018.
[3] Seto R, Mari R, Morris JF & Denn MM. Phys. Rev. Lett., 11: 218301, 2013.
[4] Wyart M & Cates ME. Phys. Rev. Lett., 112: 098302, 2014.
[5] Clavaud C, Bérut A, Metzger B & Forterre Y. Proc. Natl. Acad. Sci. USA, 114: 5147–5152, 2017.
[6] Clavaud C, Metzger B & Forterre Y. J. Rheol. in press, 2020
[7] Balmforth NJ, Bush JWM & Craster RV. Phys. Lett. A, 338: 479-484, 2005.
[8] Kapitza PL Kapitza SP. Zh. Eksp. Teor. Fiz, 18: 3-28, 1948.
[9] Ng CO & Mei CC. J. Fluid Mech., 263:151-184, 1994.

*corresponding author: yoel.forterre@univ-amu.fr

The fluid dynamics of collective vortex structures of plant-animal worms

George T. Fortune[1]*, Alan Worley[2], Ana B. Sendova-Franks[2], Nigel R. Franks[2], Raymond E. Goldstein[1]

[1]Department of Applied Mathematics and Theoretical Physics, Centre for Mathematical Sciences, Wilberforce Road, University of Cambridge, Cambridge CB3 0WA, UK
[2]School of Biological Sciences, University of Bristol, 24 Tyndall Avenue, Bristol BS8 1TQ, UK

Summary Through a combination of experiments in the field and theoretical modelling, we investigate the phenomenon of circular milling in *Symsagittifera roscoffensis* from a fluid dynamical viewpoint. By considering the circular mill as a rigid disc which rotates in the opposite direction to the motion of the worms and hence generates a vertically constant Stokes flow, we demonstrate the effect of the surrounding fluid on the mill, developing conditions for the temporal stability of a circular mill system.

Background

From the flocking of birds to the schooling of fish, collective motion, i.e. global group dynamics resulting from the interactions of many individuals, occurs all across the natural world. A visually striking example of this is circular milling, namely when individuals turn about a common centre. Studied for more than a century, since 1899 when Jean-Henri Fabre first reported the spontaneous formation of continuous loops in columns of pine processionary caterpillars [1], circular mills have been observed in many species e.g. army ants [2], fish and *Bacillus subtilis* [3].

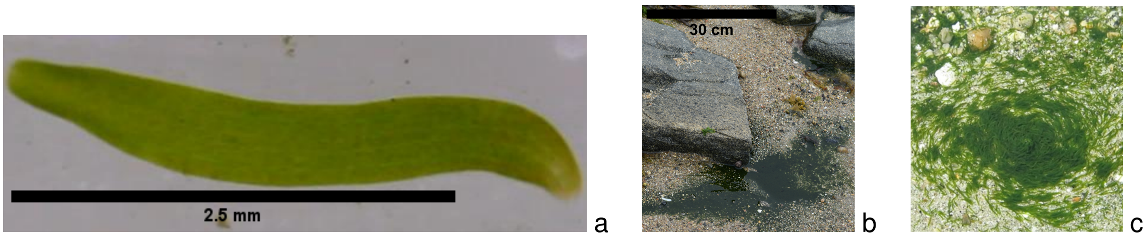

Fig. 1: (a) Adult *Symsagittifera roscoffensis*. (b) *Symsagittifera roscoffensis in situ* on the beach. (c) Circular milling on the beach (Adapted from [6]).

The marine aceol worm *Symsagittifera roscoffensis* (figure 1(a), [4]) forms circular mills, both in a shallow layer of salt water in a petri dish (figure 2(a), [5]) and also naturally on intertidal sand (figure 1(c)). *S. roscoffensis*, more commonly known as the plant-animal worm [7], engages in a photosymbiotic relationship [8] with the marine alga *Tetraselmis convolutae* [9]. The worms reside on the upper part of the foreshore of Atlantic coast beaches in large colonies of many millions (figure 1(b)). It is hypothesised that this circular milling behaviour allows the worms to self-organise into dense biofilms that, covered by a mucus layer, optimise the absorption of light by the algae for photosynthesis [5].

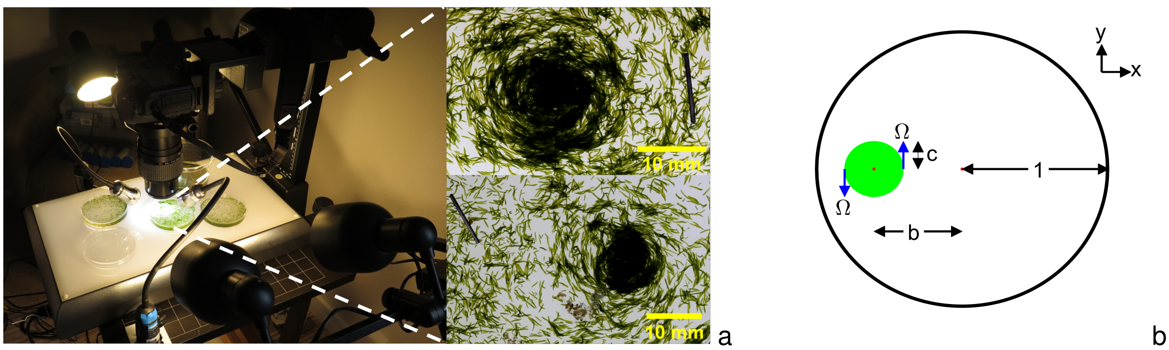

Fig. 2: (a) Experimental setup used to film circular milling behaviour in Guernsey (b) Schematic of the model showing a disc, rotating with angular velocity Ω, that has radius c and is a distance b away from the centre of a circular petri dish of unit radius.

The Fluid Dynamics of Circular Milling

Here we investigate, both theoretically and experimentally, the fluid velocity field that is generated by the motion of a circular mill and its subsequent effect on the mill. We present a simple mathematical model for the system, considering a 2D Stokes flow within a circular boundary (figure 2b). Representing a mill as a rotating disc with a defined centre and radius which are allowed to vary as functions of time, a bipolar coordinate system is utilised to yield an analytic solution for the fluid flow field. Experimentally, the evolution of circular mills is filmed using the camera setup given in figure 2(a). Despite the simplifications that result from representing a constantly evolving structure consisting of many thousands of worms by a disc, this reduced model fits the observed experimental behaviour remarkably well. For example, it correctly predicts that the flow exerts a force on the mill, causing the centre of the mill to drift on a circle centred on the middle of the arena.

Multiple Mill Systems

Experimentally, one often observes systems in which multiple circular mills co-exist. Snapshots of a binary circular mill system for three distinct experiments are given in figure 3. We bring together our mathematical model with a large experimental video data set. Our work motivates and confirms a powerful hypothesis: subsequent circular mills only form around a stagnation point of the flow produced by the first mill, with the worms tending to swim in the direction of the flow (both mills rotate in the same direction). In particular, this means that the system evolves to one of two stable states, namely a single mill with no nearby stagnation points or a set of linked mills where each mill centre is located in the stagnation regions of the other mills.

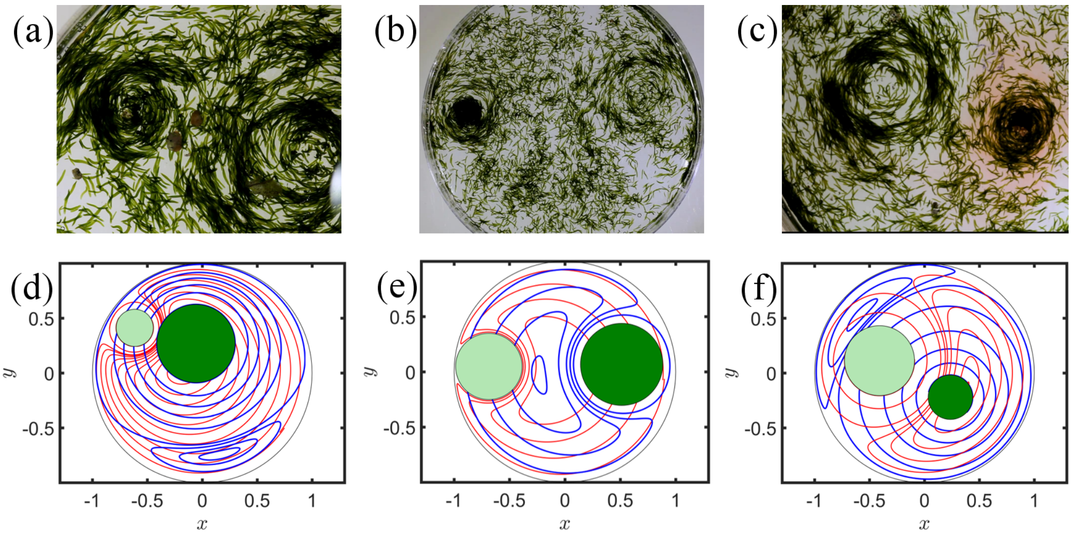

Fig. 3: Snapshots of a binary circular mill system for three distinct experiments together with corresponding streamline plots (in each case, the first mill is light green with red streamlines and the second mill is dark green with blue streamlines): (a) Unstable, with the second mill dominating, (b) Stable, (c) Unstable, on a longer timescale with the first mill dominating.

Conclusions

We have shown that a circular mill generates a substantial fluid velocity field flowing in the opposite angular direction to the direction of motion of the worms. This might allow nutrient circulation and would provide an efficient method of dispersal of waste products away from the main body of worms. We present a simple model for the system which fits the experimental results well, both in terms of the mill centre drift direction and also the predicted streamlines. Utilising this understanding, we are able to shed light on the fluid dynamical stability of circular mills. Secondary circular mills only form around a stagnation point of the flow. Stagnation points only occur when the mill is close to the arena boundary and they are typically closer to the arena centre than the initial mill. This allows the worm population to organise passively towards the centre of the arena without needing to know its exact extent. This may be beneficial for the worms since the arena centre will be less shaded and hence facilitate more effective photosynthesis.

References

[1] Fabre J-H. *Études sure l'Instinct et les Moeurs des Insectes*. Paris: Librairie Ch. Delagrave, 1899.
[2] Couzin I.D. and Franks N.R. *Proc. R. Soc. B* **270**:139-146, 2003.
[3] Cisneros L.H. et. al. *Exp. Fluids* **43**:737-753, 2007.
[4] Bourlat S.J. and Hejnol A. *Curr. Biol.* **19**:R279-R280, 2009.
[5] Franks N.R. et. al. *Proc. R. Soc. B* **283**:20152946, 2016.
[6] Sendova-Franks A.B. et. al. *R. Soc. open sci.* **5**:180665, 2018.
[7] Keeble F. *A Study in Symbiosis*. Cambridge University Press, 1910.
[8] Bailly X. et. al. *Front. Microbiol.* **5**(498):1-13, 2014.
[9] Norris R.E. et. al. *Bot. Mag. Tokyo* **93**:317-339, 1980.

*corresponding author: gtf22@cam.ac.uk

Two Stories of Fluids and Light: Algal Phototaxis and Dinoflagellate Bioluminescence

Raymond E. Goldstein [1]*

[1]Department of Applied Mathematics and Theoretical Physics, Centre for Mathematical Sciences, University of Cambridge, Wilberforce Road, Cambridge CB3 0WA

In this talk I will present two scientific stories about the involvement of microorganisms with light: one about sensing and swimming towards light (*phototaxis*), the second about organisms sensing fluid flow and generating light (*bioluminescence*). These studies illustrate how theory and experiment can be used together to address problems at the intersection of biology and physics.

Phototaxis: Green algae of the *Volvocine* lineage, spanning from unicellular *Chlamydomonas* to vastly larger *Volvox*, are models for the study of the evolution of multicellularity, flagellar dynamics, and developmental processes [1, 2]. Phototactic steering in these organisms occurs without a central nervous system, driven solely by the response of individual cells. All such algae spin about a body-fixed axis as they swim; directional photosensors on each cell thus receive periodic signals when that axis is not aligned with the light. The flagella of *Chlamydomonas* [3] and *Volvox* [4] both exhibit an adaptive response to such signals in a manner that allows for accurate phototaxis, but in the former the two flagella have distinct responses, while the thousands of flagella on the surface of spherical *Volvox* colonies have essentially identical behaviour. The planar 16-cell species *Gonium pectorale* thus presents a conundrum, for its central 4 cells have a *Chlamydomonas*-like beat that provide propulsion normal to the plane, while its 12 peripheral cells generate rotation around the normal through a *Volvox*-like beat. I will describe how experiment, theory, and computations reveal the mechanism by which *Gonium*, perhaps the simplest differentiated colonial organism, achieves phototaxis [5]. High-resolution cell tracking, particle image velocimetry of flagellar driven flows, and high-speed imaging of flagella on micropipette-held colonies show how, in the context of a recently introduced model for *Chlamydomonas* phototaxis [3], an adaptive response of the peripheral cells alone leads to photo-reorientation of the entire colony. The analysis also highlights the importance of local variations in flagellar beat dynamics within a given colony, which can lead to enhanced reorientation dynamics.

Bioluminescence: One of the characteristic features of many marine dinoflagellates is their bioluminescence, which lights up night-time breaking waves or seawater sliced by a ship's prow. While the internal biochemistry of light production by these microorganisms is well established, the manner by which fluid shear or mechanical forces trigger bioluminescence is still poorly understood. I will describe controlled measurements [6] of the relation between mechanical stress and light production at the single-cell level, using high-speed imaging of micropipette-held cells of the marine dinoflagellate *Pyrocistis lunula* subjected to localized fluid flows or direct indentation. We find a viscoelastic response in which light intensity depends on both the amplitude and rate of deformation, consistent with the action of stress-activated ion channels. A phenomenological model captures the experimental observations.

This work was supported by the Wellcome Trust and the Gordon and Betty Moore Foundation.

References

[1] Goldstein RE, Green Algae as Model Organisms for Biological Fluid Dynamics, *Annu Rev Fluid Mech* **47**:343-375, 2015.
[2] Goldstein RE, Fluid Dynamics at the Scale of the Cell, *J Fluid Mech* **807**:1-39, 2016.
[3] Leptos KC, Chioccioli M, Furlan S, Pesci AI & Goldstein RE, An Adaptive Flagellar Photoresponse Determines the Dynamics of Accurate Phototactic Steering in *Chlamydomonas*, *preprint*, 2020.
[4] Drescher K, Goldstein RE & Tuval I, Fidelity of Adaptive Phototaxis, *Proc Natl Acad Sci USA* **107**:11171-11176, 2010.
[5] de Maleprade H, Moisy F, Ishikawa T & Goldstein RE, Phototaxis in *Gonium*, the Simplest Differentiated Colonial Alga, *Phys Rev E* **101**:022416, 2020.
[6] Jalaal M, Schramma N, Dode A, de Maleprade H, Raufaste C & Goldstein RE, Stress-Induced Dinoflagellate Bioluminescence at the Single Cell Level, *preprint*, 2020.

*corresponding author: R.E.Goldstein@damtp.cam.ac.uk

Ellipsoids in inviscid and Stokes flow

Rama Govindarajan[1]*

[1]International Centre for Theoretical Sciences, Tata Institute of Fundamental Research, Shivakote, Bengaluru 560089, !ndia.

Summary

This talk contains three stories about the dynamics of solid objects in fluid. In inviscid flow, a triaxial ellipsoid can execute chaotic motion, whereas the dynamics of a spheroid is more limited. In Stokes flow, the Crowley instability of an array of spheres can be suppressed by a departure from a spherical shape. In unsteady Stokes flow, the Basset-Boussinesq history term is calculated by a new approach, without the need for constantly increasing storage.

A triaxial ellipsoid in inviscid fluid

In 1982, Kolzov and Onishchenko [1] proved that the motion of an ellipsoid immersed in inviscid fluid is non-integrable if its shape satisfies a certain condition. Aref and Jones [2] then demonstrated chaotic orbits executed by such an ellipsoid. The condition is satisfied whenever the ellipsoid is triaxial, i.e., when all three axes of the ellipsoid are unequal. We have shown [3], by solutions of the Kirchoff-Clebsch equations, and by high resolution numerical simulations using a variant of the immersed boundary method, that the fraction of phase space displaying chaotic orbits increases with the fluid/solid density ratio. It also depends on the fraction of energy initially in translational motion, see figure 1(a). We will discuss how the added mass tensor of the system is an important player. We have identified a new integral of motion for a spheroid in inviscid fluid: one component of the generalised angular momentum. This makes the dynamics of a spheroid more restricted in many ways than that of a triaxial ellipsoid.

Slowly settling disks

An array of spheres settling in Stokes flow will display an instability to clumping. This is called the Crowley instability. We discuss how [4], when we have an array of disks or spheroids rather than spheres, the orientation of the objects can compete with the tendency to clump, and stabilise the structure. However, the relevant linear stability matrix is non-normal, so we have algebraic growth of perturbations, which can trigger nonlinearity. We show this experimentally and in numerical solutions of far-field Stokes equations.

Spheres with history

The Maxey-Riley equations, which describe the dynamics of a small spherical particle in unsteady Stokes flow, contain a history term due to the relative acceleration of the particle and the fluid. This term is notoriously difficult to handle since it involves an integral demanding ever-increasing storage. We show [5] how this term may be computed exactly and without the need for such high storage but solving a heat equation in a fictitious domain, where the Maxey-Riley equation appears as a Robin boundary condition.

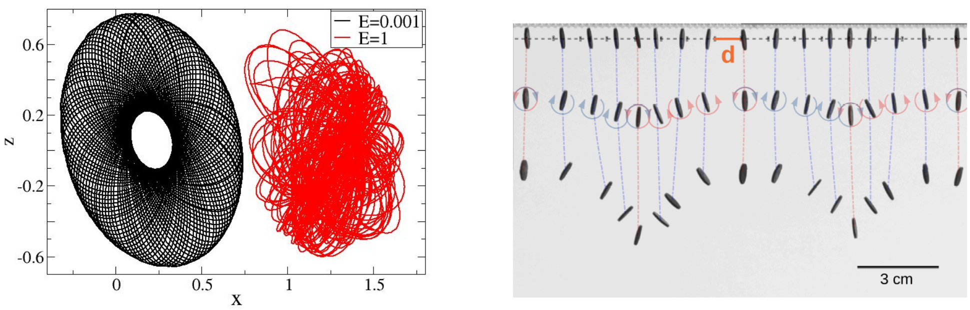

Fig. 1: (a) Depending on the ratio E of energy in rotational motion versus translational motion initially, a triaxial ellipsoid can execute periodic or chaotic motion [3]. (b) An array of settling disks in the linearly unstable regime [4].

References

[1] V. V. Kozlov and D. A. Onishchenko, Nonintegrability of Kirchhoff's equations, 1982, *Sov. Math. Dokl*, **26**, 2, pp.495–498.

[2] Hassan Aref and Scott W. Jones, Chaotic motion of a solid through ideal fluid, 1993, *Physics of Fluids A*, **5**, pp. 3026.

[3] Erich Essmann, Pei Shui, Stephane Popinet, Stephane Zaleski, Prashant Valluri and Rama Govindarajan. Chaotic orbits of tumbling ellipsoids, 2020, under revision for the *Journal of Fluid Mechanics.*

[4] Rahul Chajwa, Narayanan Menon, Sriram Ramaswamy and Rama Govindarajan. Waves, algebraic growth and clumping in sedimenting disk arrays, 2020, preprint.

[5] S Ganga Prasath, Vishal Vasan and Rama Govindarajan. Accurate solution of the Maxey-Riley equation, and effects of Basset history, 2019. *Journal of Fluid Mechanics*, 2019. **868**, pp. 428-460.

*corresponding author: rama@icts.res.in

Dilute sedimenting suspensions of spheres at small inertia

Laurence Bergougnoux[1] and Élisabeth Guazzelli[2*]

[1]Aix-Marseille Univ, CNRS, IUSTI, Marseille, France
[2]MSC, CNRS, Université de Paris, Paris, France

Sedimentation of particles is ubiquitous in natural phenomena such as mud sedimentation in rivers and estuaries and rain drop sedimentation in the atmosphere. It is also a basic engineering technique of separation or clarification used in particular in water treatment process for removing suspended solids from water. While it can be considered as one of the simplest suspension flows, much remains to be understood. The key difficulty lies in the long range nature of the multibody hydrodynamic interactions between the particles which leads to complex and collective dynamics.

One of the primary formula used in sedimentation is the Stokes velocity V_S which gives the terminal velocity of a single sphere falling in a quiescent fluid in the absence of inertia, $V_S = (2/9)a^2(\rho_p - \rho_f)g/\mu$, where a is the sphere radius, ρ_p and ρ_f the density of the particles and the fluid, respectively, and μ the fluid viscosity. Going beyond a single sphere and obtaining the mean settling speed of a concentrated suspension is much more difficult. As stated above, the difficulty comes from the long range nature of the hydrodynamic interactions which leads to integrals diverging with the size of the container when the interactions are naively summed. This divergence paradox was solved by Batchelor [1] who gave the first order correction in volume fraction ϕ to the Stokes velocity (i.e. -6.55ϕ) assuming low ϕ and randomly dispersed spheres.

The mean velocity does not characterize completely the sedimentation dynamics as the constantly changing configuration of the suspension microstructure and the resulting long-range hydrodynamic interactions cause significant fluctuations of the individual particle motions about the mean. It happens that a divergence paradox again arises for the variance of the fluctuating velocities [2]. A scaling argument given by Hinch [3] brings some understanding of this divergence. The random mixing of the suspension creates statistical fluctuations in particle number, $\sqrt{N}$ (where N is the particle number), also called blobs on all length-scales l from container size, L, down to the mean interparticle spacing, $a\phi^{-1/3}$. Balancing the fluctuations in the weight, $\sqrt{N}\frac{4}{3}\pi a^3(\rho_p - \rho)g$, against the Stokes drag on the blob, $6\pi\mu l w'$, yields convection currents, $w' \sim V_S\sqrt{\phi l/a}$. Hence, the fluctuations on the length-scale of the container, L, are dominant.

In experiments with large sedimentation vessels, large vortices of the size of the container dominates the initial moments after the cessation of mixing, in agreement with the predicted scaling with $l = L$. But these initial large fluctuations are transient and decay in time to weaker small-scale fluctuations of the order of 20 interparticle separations (i.e. $\approx 20\,a\phi^{-1/3}$) which remain constant in a plateau region until the arrival of the upper sedimentation front between the suspension and the clear fluid [4, 5]. This reduction of the initially large fluctuations to a smaller steady value is consistent with the further speculation of Hinch [3] that the strong initial convection currents would remove long-wavelength horizontal density fluctuations, leaving the irreducible scale of the interparticle separation, $a\phi^{-1/3}$ (in fact more like ≈ 20 this irreducible scale in the experiments). This description is of course valid for container size larger than 20 interparticle separations. Otherwise, the velocity fluctuations always depend on the container size and follow the predicted scaling with $l = L$ [6].

The above results hold for vanishing Reynolds number and much less is known when inertia is not negligible. In experiments, whereas the particle Reynolds number, $Re_a = \rho_f a V_S/\mu$, may be still maintained very small, the container Reynolds number, $Re_L = \rho_f L V_S/\mu = Re_a L/a$, may not be that small. Hinch [3] noted that the initial large-scale convection currents could be limited by inertial forces, $\rho_f {w'}^2 l^2$, rather than by viscous forces, yielding $w' \sim \sqrt{ag}\,\phi^{1/4}(l/a)^{-1/4}$. This large-$Re_L$ prediction presents a decrease with the size of the container whereas the Stokes-regime prediction shows an increase. Hinch speculated that the observed fluctuations would be those found at matching. This leads to $w' \sim V_S\,\phi^{1/3}Re_a^{-1/3}$ and thus to a screening of the fluctuations by inertia with a decrease in fluctuations scaling as $Re_a^{-1/3}$. An alternative argument leading to the same scaling was given by Brenner [7]. These arguments are designed to be valid for vanishing Re_a.

Conversely, Koch [8] examined the case of moderate particle Reynolds numbers, i.e. $Re_a \sim 1$, and considered the variance of a dilute suspension of randomly distributed particles producing linearly superimposed Oseen fluid velocity disturbances. In that case, the velocity fluctuations still increase with the size of the container but the divergence is weaker, to be more precise $w' \sim \sqrt{\log L/a}$ in this Oseen regime instead of $w' \sim \sqrt{L/a}$ in the Stokes regime. These fluctuations are predicted to decrease as $Re_a^{-1/2}$ for large Re_a, i.e. $Re_a > 5$. Koch [8] also noted that the lift force acting on a particle in the wake of another particle tends to push it outward and argued that this spreading of the wake would lead to fluctuations independent of the system size.

Numerical simulations at moderate inertia showed that the divergence with the size of the box was much slower than that for Stokes flow [9, 10, 11] in good agreement with the logarithmic prediction of [8] and even could disappear when sufficiently large domain size and simulation time were used [12]. They demonstrated the importance of the wake-induced interactions between the spheres and a clear tendency for a reduction of both the average settling velocity and the relative fluctuations in the weak inertia regime. There is however a lack of real experiments against which the theoretical scalings and simulations can be compared [13, 14].

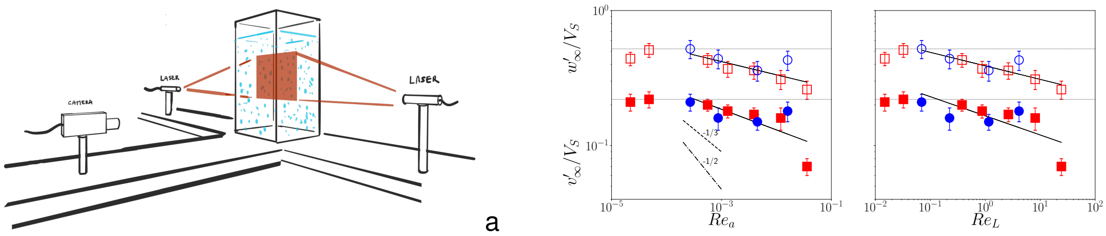

b

Fig. 1: (a) Sketch of the experimental apparatus. (b) Plateau velocity fluctuations, w'/V_S and v'/V_S, in the vertical (open symbols) and the horizontal (filled symbols) directions, respectively, versus Re_a and Re_L for two batches of spheres (red square and blue circle). The horizontal dotted lines correspond to the constant plateau fluctuations in the vertical and horizontal directions for the Stokes regime. The solid lines are power-law fittings of the data in the vertical and horizontal directions. The power laws $-1/3$ and $-1/2$ are represented by dashed and dashed-dotted lines, respectively.

In this contribution, we examine dilute sedimenting suspensions in large containers (larger than 20 interparticle separations) when inertia is increased by means of decreasing the viscosity of the fluid. When inertia is progressively augmented, the container Reynolds number can become greater than one whereas the particle Reynolds number remains smaller than one. In the present experiments, the container Reynolds number is $0.01 \lesssim Re_L \lesssim 25$ whereas the particle Reynolds number is $2\,10^{-5} \lesssim Re_a \lesssim 4\,10^{-2}$.

The sedimentation experiments were carried out in a glass container. Two batches of spheres having different sizes and densities were used but same initial volume fraction $\phi_0 = 0.3\%$ was imposed. A thin light-sheet produced by two red laser diodes facing each other was used to illuminate the median plane of the glass container, see figure 1a. The illuminated particles were imaged by a camera placed at right angles to the light-sheet. Particle image velocimetry was used to measure the sedimentation dynamics.

While the long-time velocity fluctuations are constant in the Stokes regime, they are seen to decrease with increasing inertia above the critical Reynolds numbers $Re_a \sim 4\,10^{-4}$ and $Re_L \sim 0.1$, and more precisely to vary as a power of the Reynolds number ($\sim Re_a^{-0.1}$) differing from the theoretical predictions of Hinch [3], Brenner [7] ($\sim Re_a^{-1/3}$), and Koch [8] ($\sim Re_a^{-1/2}$) as well as from the results of the large-box simulations of Sungkorn and Derksen [12] ($\sim Re_a^{-0.69}$), see figure 1b. To capture the observed fluctuation decrease, it is tempting to extend the Caflisch-Luke-Hinch model to a drag experienced by the blobs which accounts for small inertial corrections. However, the microstructure of the suspension is seen to evolve with increasing inertia and to depart from random positioning, which differs from the model underlying assumption.

References

[1] Batchelor GK. *J. Fluid Mech.* **52**:245-68, 1972.
[2] Caflisch RE & Luke JHC. *Phys. Fluids* **28**:759-60, 1985.
[3] Hinch EJ. in *Disorder and Mixing*. Kluwer Acad. 153-61, 1988.
[4] Guazzelli É. *Phys. Fluids* **13**:1537-40, 2001
[5] Guazzelli É & Hinch EJ. *Annu. Rev. Fluid Mech.* **43**:97-116, 2011.
[6] Segrè PN, Helbolzheimer E & Chaikin PM. *Phys. Rev. Lett.* **79**:2574-77, 1997.
[7] Brenner MP. *Phys. Fluids* **11**:754–772, 1999.
[8] Koch DL. *Phys. Fluids* **5**:1141-55, 1993.
[9] Climent E & Maxey MR. *Int. J. Multiph. Flow* **29**:579-601, 2003.
[10] Yin X & Koch DL. *Phys. Fluids* **19**:093302, 2007.
[11] Yin X & Koch DL. *Phys. Fluids* **20**:043305, 2008.
[12] Sungkorn R & Derksen JJ. *Phys. Fluids* **24**:123303, 2012.
[13] Cowan ML, Page JH & Weitz DA. *Phys. Rev. Lett.* **85**:453-456, 2000.
[14] Segrè PN. *arXiv*: 0709.0995, 2007.

*corresponding author: elisabeth.guazzelli@univ-paris-diderot.fr

Levitation and locomotion on an air-table of plates with herringbone grooves.

by John Hinch and Hélène de Maleprade

DAMTP-CMS, Cambridge University
Wilberforce Road, Cambridge, CB3 0WA, UK

ejh1@cam.ac.uk

Abstract:

Experiments in ESPCI in Paris and numerical simulations in Darmstadt have shown that plates with herringbone grooves in their base are accelerated on a smooth air-table in the direction that the chevron grooves point, while smooth plates on an air-table with herringbone grooves are accelerated in the opposite direction. Newton's third law? Not quite.

A simple two-dimensional model is constructed of the air flow down a long channel with pressure controlled influx across the lower boundary: lubrication theory with inertia or boundary layers without an outer flow.

Limiting cases are considered of low and high Reynolds numbers, and of small and large pressure drop down the channel compared with the pressure drop across the porous plate; all tested against numerical solutions.

The levitation and locomotion forces are calculated, with a relatively simple prediction for the locomotive acceleration; which fits the experimental data with plausible excuses.

Hairy Hydrodynamics

A. E. Hosoi[1]*

[1]Massachusetts Institute of Technology, 77 Massachusetts Ave, Cambridge, MA 02139, USA

Flexible slender structures in flow are everywhere. While a great deal is known about individual flexible fibers interacting with fluids, considerably less work has been done on fiber ensembles, such as fur or hair, in flow. These hairy surfaces are abundant in nature and perform multiple functions from thermal regulation to water harvesting to sensing; they appear as wind through grass, as sensors in the inner ear and on the antennae of insects and crustaceans, as fur on diving marine mammals, and on the tongues of nectar-feeding organisms, to name a few. In a series of studies, we have developed reduced models to capture the underlying physical mechanisms in these biological systems. In all of the cases we have investigated, these models can be mapped onto some of the most iconic fluid dynamic experiments, modified by the addition of hairs or other mesoscale features at the boundaries. A summary of the systems we have explored to date is presented in Figure 1.

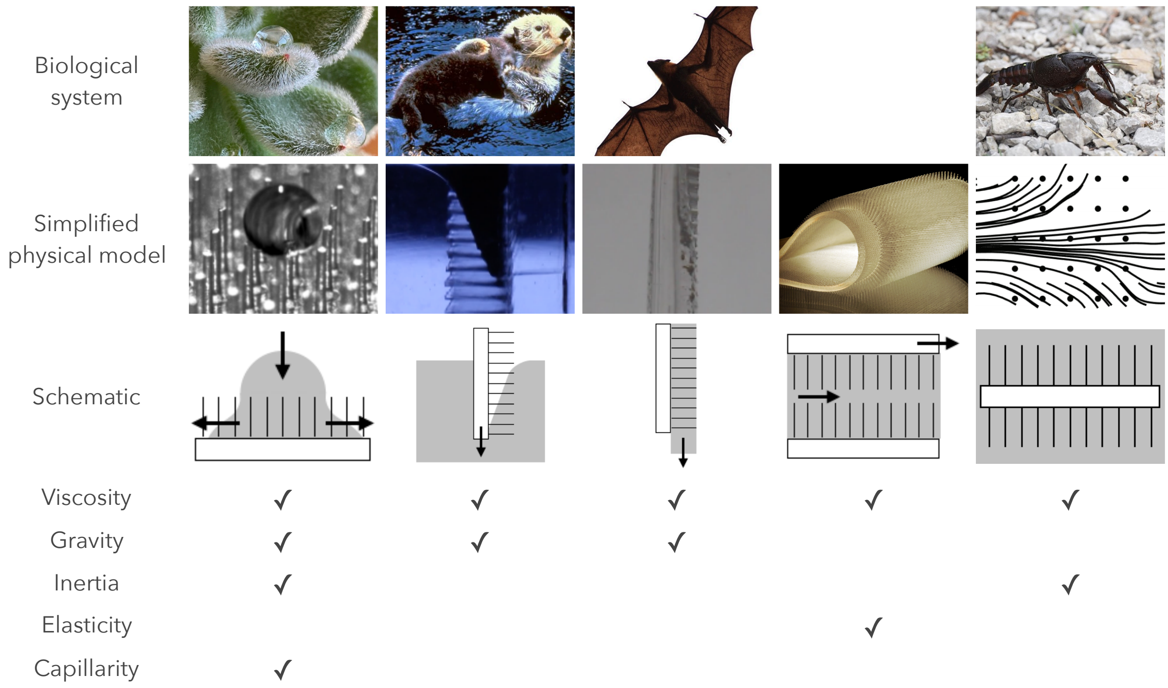

Fig. 1: Summary of the hairy hydrodynamical systems we have considered to date. The top row shows the motivating biological systems; image credits: Sea otter image is in the common domain, bat image [1] and crawdad image [2] from Wiki Commons. The second row shows photos or data from laboratory table-top experiments which illustrate simplified representations of the underlying physics. From left to right: droplet impacting a hairy surface [3]; air entrainment in the fur of diving mammals modeled as a hairy plate plunging into a viscous bath [4]; viscous drainage through hair beds as a model for nectar uptake in drinking bats and other nectarivores [5]; design of flow rectifiers via viscous flow through hairy channels [6]; optimal sensing and feeding in crustaceans modeled as flow through bristles at varying Reynolds numbers [7].

In this talk I will describe two examples of hairy surfaces interacting with flow. In the first example I will illustrate the rich landscape of phenomena that are brought out with the addition of hairs or other mesoscale structures at boundaries via a toy problem of angled hairs in Couette flow. Using this simple model, I explore asymmetry in the flow and anomalous drag scaling by exploiting various limits in the parameter space. In the second example I will move on to a biological system and consider hairy appendages on crustaceans which are used to sense and track food. These animals influence the flow through the hairs by changing the speed of the appendage as it moves through the fluid, thereby manipulating the Reynolds number. It is known that by changing the velocity of the flow relative to the appendage, the hairs can act either as a rake, diverting flow around the hair array (useful in feeding), or as a sieve, filtering flow through the hairs (useful in sensing) [8, 9]. We develop a reduced-order model that predicts the flow phase based on the depth of the boundary layer around a single hair. Model predictions are compared with measurements of hairs in both chemosensing and suspension-feeding crustaceans.

References

[1] This file is licensed under the Creative Commons Attribution 4.0 International license. `https://commons.wikimedia.org/wiki/File:Flying-Fox-Bat.jpg`

[2] This file is licensed under the Creative Commons Attribution 2.0 Generic license. `https://commons.wikimedia.org/wiki/File:Crawdad%3F_(35551202476).jpg`

[3] Nasto, Alice et al. *Phys. Rev. Fluids* **4**, 064004, 2019.

[4] Nasto, Alice et al. *Phys. Rev. Fluids* **1**, 033905, 2016.

[5] Nasto, Alice et al. *Phys. Rev. Fluids* **3**, 024002, 2018.

[6] Alvarado, José et al. *Nature Phys.* **13**, 1014-1019, 2017.

[7] Hood, Kaitlyn et al. *Phys. Rev. Fluids* **4**, 114102, 2019.

[8] Koehl MAR et al. *Science* **294**, 1948, 2001.

[9] Koehl MAR et al. *Mar. Biol.* **133**, 419, 1999.

*corresponding author: peko@mit.edu

Quantifying irreversible mixing from the shear-induced breaking of large amplitude internal gravity waves

Christopher J. Howland[1]*, John R. Taylor[1], C. P. Caulfield[2,1]

[1]Department of Applied Mathematics and Theoretical Physics, Centre for Mathematical Sciences, University of Cambridge, Wilberforce Road, Cambridge CB3 0WA, UK
[2]BP Institute, University of Cambridge, Madingley Road, Cambridge CB3 0EZ, UK

Introduction

Turbulent mixing exerts a vital influence on the transport of tracers such as heat, carbon and nutrients throughout the ocean. This mixing is especially important in the thermocline, where strong stratification inhibits vertical transport and turbulence can enhance diapycnal mixing (across density surfaces). Due to the strong stratification, turbulence in the thermocline is highly intermittent in both space and time, with sporadic, highly energetic 'mixing events' commonly attributed to the breaking of internal waves.

Near-inertial internal waves, whose dynamics are controlled by the Earth's rotation, introduce vertical shear and can break at sufficiently large amplitude through shear instabilities. By contrast, higher frequency internal *gravity* waves introduce vertical motion and strain into the density field, which can lead to breaking via a combination of shear and convective instabilities. Observations in the thermocline [1] reveal that local overturns in density profiles, associated with mixing, can be produced in regions where both shear and wave-induced strain contribute significantly to the flow dynamics. Understanding how the interaction of internal gravity waves and near-inertial shear leads to turbulent mixing is thus vital in constraining diapycnal fluxes in the ocean interior. This study aims to identify the primary mechanisms that lead to turbulence in such flows and pinpoint how these depend on the relative amplitude of the gravity waves compared to the shear. We also aim to quantify mixing, appropriately defined as the irreversible transfer of available potential energy to background potential energy, in these flows and test how well simple parameterisations can describe their energetics.

Materials and methods

We use high resolution direct numerical simulations to investigate the turbulent mixing that arises due to the interaction of a sinusoidal shear flow and an internal gravity wave. Motivated by the observations of [1] in the ocean thermocline, we consider an initial value problem where the shear flow $\overline{u} = \sin(z)$, with a minimum gradient Richardson number of 1, is superimposed on a finite-amplitude internal gravity wave with wave vector $\boldsymbol{k} = (1/4, 0, 3)$. We perform the simulations in a triply-periodic domain at Reynolds numbers of 5000 and 8000, and vary the initial wave steepness s to investigate the relevant breaking mechanisms in different flow scenarios. The equations of motion are solved subject to the Boussinesq approximation and a uniform background stratification.

We extend the definitions of available potential energy from [2] and [3] for use in our triply-periodic computational domain, and compare the "true" rate of irreversible turbulent mixing

$$\phi_d = \frac{Ri_0}{RePr}\left\langle \frac{\partial z_*}{\partial \theta}\left|\nabla\theta\right|^2\right\rangle, \tag{1}$$

to the dissipation rate of scalar variance χ commonly used to infer mixing rates in stratified turbulence.

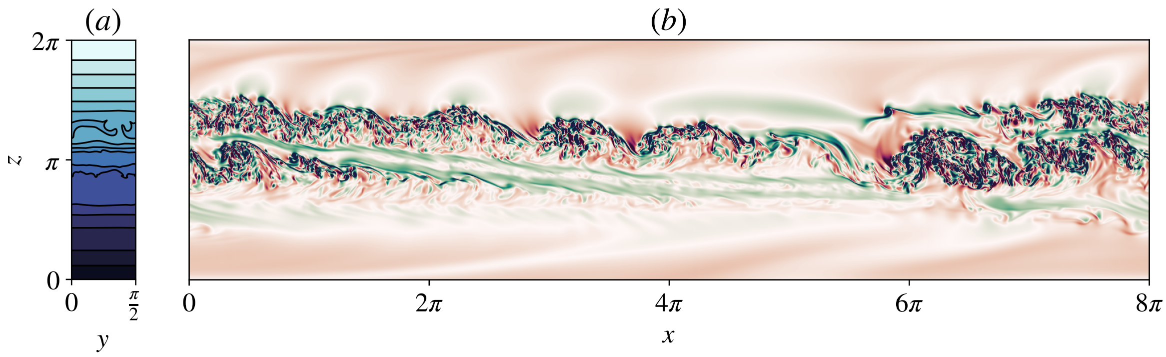

Fig. 1: (a) Snapshot of density field contours in a spanwise-vertical plane at time $Nt = 26$. (b) Snapshot of the spanwise vorticity component in a streamwise-vertical plane at time $Nt = 32$. Both snapshots are taken from the simulation with initial wave steepness $s = 1$ at $Re = 5000$.

Results

The initial dynamics of all our numerical simulations involve the shear flow distorting the internal wave in a similar fashion to how waves are refracted in weakly nonlinear ray tracing calculations. Perturbation length scales increase in regions associated with positive shear, whereas in regions of negative shear these scales decrease. For the larger values of initial wave steepness (e.g. $s = 1$) this quickly leads to regions with statically unstable density profiles, and a build-up of available potential energy. As shown in figure 1a, convective plumes develop locally in the region of negative shear (close to $z = \pi$), introducing spanwise variation to the initially two-dimensional flow. At later times local shear instabilities develop, leading to the 'trains' of turbulent billow structures seen in figure 1b.

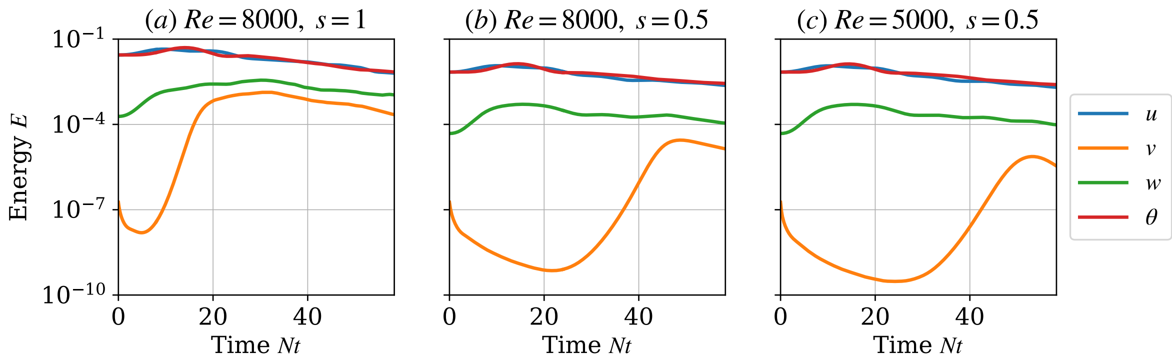

Fig. 2: Time series of the perturbation energy associated with individual components of velocity $\boldsymbol{u}$ and the scalar field θ, plotted on a logarithmic scale.

The energy associated with the spanwise velocity component grows exponentially in every simulation once a local Rayleigh number of $Ra = O(1000)$ exists somewhere in the domain, as seen from the orange curves in figure 2. We can deduce that a linear convective instability plays an important role in the early development of three-dimensional motion in these flows. Figure 2 also shows that the onset time of this linear growth depends strongly on the initial wave steepness s, but not so much on the Reynolds number of the flow. The difference in the peak values of the spanwise energy in figures 2b and 2c highlights that smaller Re does however affect the nonlinear saturation of the instability.

As well as providing a mechanism for the generation of small scales, this local convection significantly modifies the density profile on which the turbulent structures seen in figure 1b develop. Locally this leads to significant differences between χ and ϕ_d, with χ overestimating mixing in areas of low local stratification and underestimating mixing in areas of high local stratification. The discrepancies in the local mixing rates may furthermore lead to significant changes in the inferred value of the total diapycnal flux for these wave breaking events.

References

[1] Alford M & Pinkel R. *J. Phys. Oceanogr.* **30**(5):805-832, 2000.
[2] Winters KB et al. *J. Fluid Mech.* **289**:115-128, 1995.
[3] Scotti A & White B. *J. Fluid Mech.* **740**:114-135, 2014.

*corresponding author: cjh225@damtp.cam.ac.uk

FREEZING A RIVULET

A. Huerre[1]*, A. Monier[2], T. Séon[2], C. Josserand[1]

[1]LadHyX, UMR 7646 CNRS-Ecole Polytechnique, IP Paris, 91128 Palaiseau CEDEX, France
[2]Sorbonne Université, CNRS, UMR 7190, Institut Jean Le Rond ∂'Alembert, F-75005 Paris, France

Abstract

We investigate experimentally the formation of the particular ice structure obtained when a capillary trickle of water flows on a cold substrate. We show that after a few minutes the water ends up flowing on a tiny ice wall whose shape is permanent. We characterize and understand quantitatively the formation dynamics and the final thickness of this ice structure. In particular, we identify two growth regimes. First, a 1D solidification diffusive regime, where ice is building independently of the flowing water. And second, once the ice is thick enough, the heat flux in the water comes into play, breaking the 1D symmetry of the problem, and the ice ends up thickening linearly downward. This linear pattern is explained by considering the competition between the water cooling and its convection.

Introduction

Solidification in flowing systems is a question encountered in numerous area such as geophysics, metallurgy and aeronautics. From a geophysical point of view, understanding of solidification of lava flows could help preventing the impact of volcanic eruptions on human populations [1]. The metallurgic industry is also interested in understanding the fine coupling between hydrodynamics and solidification to control the aparition of cracks during the formation of metal sheets [2]. Finally, freezing of velocity sensors during commercial flights is thought to be responsible for plane crashes. As a result, understanding the freezing process of small quantities of liquid flowing over a cold surface could help for all those topics. In this study, we will investigate experimentally and theoretically the freezing of a rivulet, obtained by flowing water on a cold solid substrate.

Experimental Method

In order to study the effect of different parameters on the shape of the ice structure formed while freezing a rivulet, we built a simple model experiment. We flowed water dyed with fluorescein (water layer thickness h_{w}) on a mettalic inclined substrate which is cooled to a given temperature, T_{s}, with liquid nitrogen. We record the evolution of the ice thickness h_{i}, taking advantage of the de-activation of fluorescein upon freezing (see Figure 1a). We vary experimentally the thermal parameters: the substrate and the liquid temperatures (T_{s} and T_{in}, respectively).

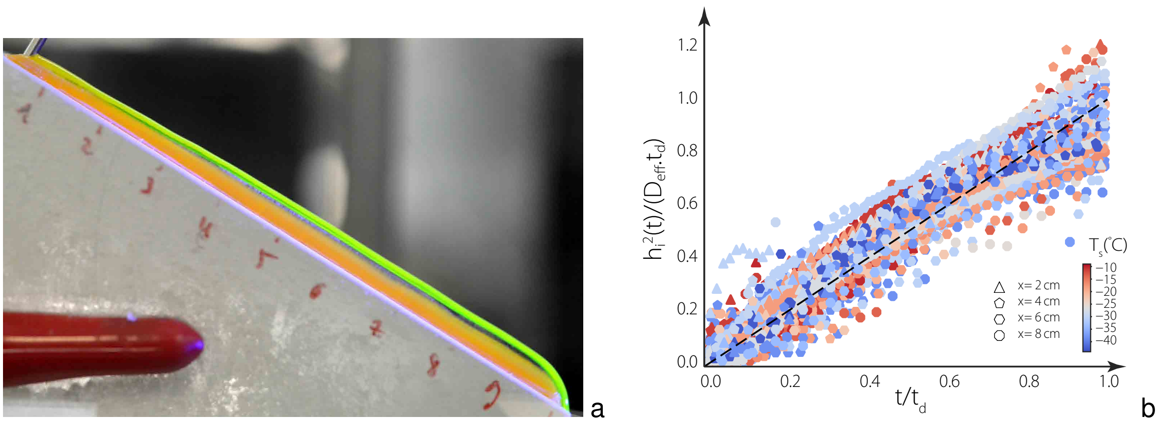

Fig. 1: (a) Side view of the ice structure (orange) with water flowing on top (yellow) (b) Rescaled ice thickness $h_{\mathrm{i}}^2(t)/(D_{\mathrm{eff}}t)$, $t \in [0, t_{\mathrm{d}}]$ as a function of the non-dimensional time t/t_{d}. D_{eff} is computed from [5] and t_{d}, the time where the spatially homogeneous growth ends, is experimentally determined.

Initial diffusive growth

When growing initially, the ice layer thickness is found to vary with the square-root of time. To understand this short time behavior of the ice layer growth, we model it by using the Stefan condition, where the latent heat produced by the ice formation results from the difference between the heat fluxes through the ice and the water. It reads here:

$$\rho_{\rm i}\mathcal{L}\partial_t h_{\rm i} = \lambda_{\rm i}\partial_y T\left(x, h_{\rm i}^-, t\right) - \lambda_{\rm w}\partial_y T\left(x, h_{\rm i}^+, t\right), \tag{1}$$

where $\rho_{\rm i}$ is the ice density, $\lambda_{\rm i,w}$ are the heat conductivities of the ice and water respectively, and $\mathcal{L}$ the latent heat of solidification. Initially, when $h_{\rm i} \ll h_{\rm w}$, the flux through the ice, which scales as $\lambda_{\rm i}(T_{\rm m} - T_{\rm s})/h_{\rm i}$, is dominant compared to the flux through the water. This dynamics at short time corresponds to the classical one dimensional problem of the growth of an ice layer when a liquid is suddenly put in contact with a substrate at a uniform subfreezing temperature, usually known as the *classical Stefan problem* [4, 3]. In this situation, the front follows a diffusive dynamics: $h_{\rm i}(t) = \sqrt{D_{\rm eff}\, t}$, where the coefficient $D_{\rm eff}$ is solution of a transcendental equation that involves $T_{\rm s}$, $\mathcal{L}$ and the ice and aluminum thermal coefficients.

In Fig. 1b, we plot the rescaled ice thickness $h_{\rm i}^2(t)/(D_{\rm eff}t_{\rm d})$, $t \in [0, t_{\rm d}]$, where $D_{\rm eff}$ is calculated using a refined model of the classical Stefan problem [5], versus the non-dimensional time $t/t_{\rm d}$. The graph presents the results of 31 experiments and 4 different positions along the plane, where $T_{\rm s}$ varies from -9 to -44°C and $T_{\rm in}$ from 8 to 35°C. All the data collapse on a line of slope 1, confirming that at short time the ice growth is only determined by the heat transfer toward the substrate without influence of the water flow.

Permanent regime

After few minutes, the ice thickness reaches a permanent regime where the water continues to flow on an ice wall. The thickness of the ice layer grows linearly along the plane, forming an angle β with the mettalic plane.

The presence of such a permanent regime can be understood qualitatively by considering the thermal fluxes at the ice-water interface. Because the ice acts as a thermal diffusive layer between the plate and the liquid, the cooling flux - through the ice layer - diminishes as the ice layer thickens and the temperature gradient decreases. On the other hand, since the flowing water is dispensed at constant temperature on the forming ice layer, the heat flux brought to the system is constant. Consequently, an equilibrium is reached when the ice layer thickness is such that both fluxes balance.

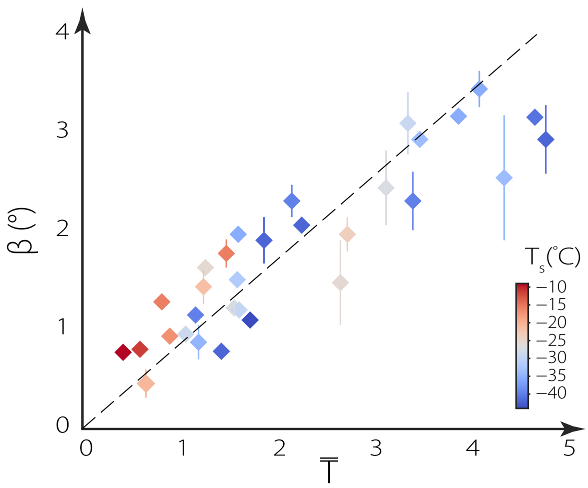

Fig. 2: Slope of the ice layer β as a function of the rescaled temperature $\bar{T} = \frac{T_{\rm m}-T_{\rm s}}{T_{\rm in}-T_{\rm m}}$.

To rationalize the peculiar structure formed by the ice, we derive and solve the temperature field in the ice layer and in the water. Coupling this to the flux continuity at the interface, we show that the ice thickness should follow the law:

$$h_{\rm max}(x) \sim h_{\rm w}\frac{\lambda_{\rm i}}{\lambda_{\rm w}}\frac{T_{\rm m} - T_{\rm s}}{T_{\rm in} - T_{\rm m}}(1 + a\, x)\,. \tag{2}$$

This calculation predicts, in particular, that the slope of the ice structure β should vary linearly with the reduced temperature $\bar{T} = (T_{\rm m} - T_{\rm s})/(T_{\rm in} - T_{\rm m})$. Figure 2 shows precisely the experimental values of β, measured for all of our experiments with different water and substrate temperatures, as a function of $\bar{T}$. The color-code corresponds to experiments performed with different $T_{\rm s}$. The dashed line is a linear fit of the data, showing a very good agreement with the prediction of Eq. (2).

Conclusions

Performing simple experiments and exploring the shape adopted by the ice, we were able to probe the effect of hydrodynamics on the solidification process. After an initial diffusive growth, we observe a stationnary regime. It could be explained by a subtle balance between the advection of heat imposed by the water flow and the diffusion through the ice layer.

References

[1] Hardee, H. C. *J. Volcanol. Geotherm. Res.*. **3**:211-23, 1980.
[2] Cieslak, M. J. *Welding Journal*. **70**.2, 1991.
[3] Rubinstein, L.I., *The Stefan Problem*. American Mathematical Soc., 1971.
[4] Stefan, J. *Annal. der Phys.*. **278**:269-286, 1891
[5] Thiévenaz, V. et al. *J. Fluid Mech.*, **874**:756-773, 2019.

*corresponding author: axel.huerre@gmail.com

George Batchelor and the Founding of EUROMECH

Patrick Huerre

Laboratoire d'Hydrodynamique - LadHyX, CNRS - Ecole Polytechnique, Institut Polytechnique de Paris, F-91128 Palaiseau, France

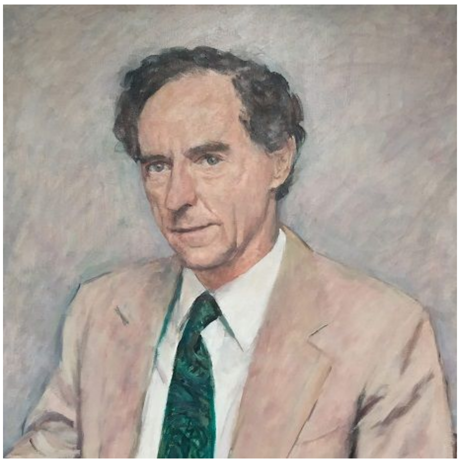 a  b

Fig. 1: The founders of Euromech: (a) George Batchelor (1920–2000); (b) Dietrich Küchemann (1911–1976).

Over the last fifty years the European Mechanics Society, commonly referred to as Euromech, has succeeded in bringing together the community of European scientists engaged in fundamental and applied research in Mechanics. This process came about through the decisive steps and initiatives taken collectively by a few outstanding personalities among whom the Australian-born George Batchelor emerged as a natural benevolent leader. In this presentation, a short account of the "story" of Euromech is given by its former President between 2003 and 2012. A very comprehensive history of the Society until 2000 [1] was an extremely valuable source of information for the preparation of this talk.

After the Second World War, in the early and mid-sixties, scientists in several European countries began to consider exchanging scientific ideas and organising conferences on the European scale. Any effort in that direction would have to face the division between Eastern and Western Europe brought about by the "Cold War". Two exceptional fluid dynamicists, George Batchelor (Figure 1a) and Dietrich Küchemann (Figure 1b), shared the compelling need for European cooperation in the Mechanical Sciences.

George Batchelor (1920–2000) moved from Australia to the UK in 1945 to work with G.I. Taylor. In the early sixties he was internationally renowned for his accomplishments in the field of turbulence. He knew well the Fluid and Solid Mechanics communities in Eastern and Western Europe and in America. For several years he had been a member of the influential Congress committee of the International Union of Theoretical and Applied Mechanics (IUTAM). Foremost, he was the founder, in 1959, of the respected Department of Applied Mathematics and Theoretical Physics (DAMTP) at the University of Cambridge. In 1956 he had also founded the Journal of Fluid Mechanics which was already considered as the preeminent means of publication in the field. He knew many colleagues from Eastern Europe and from the Soviet Union, a great asset to build bridges across the whole of Europe.

Dietrich Küchemann (1911–1976) studied for his Doctorate in Göttingen under the supervision of Ludwig Prandtl. Until 1946, he was engaged in High Speed Aerodynamics research at the famous *Aerodynamische Versuchsanstalt* (AVA), also in Göttingen. He then moved to the UK to join the Royal Aircraft Establishment (RAE) in Farnborough. Dietrich Küchemann was very much a European man and a citizen of the World [1]. He ultimately became Chief Scientific Officer at RAE and a Visiting Professor at Imperial College.

George Batchelor, the renowned and greatly influential scholar, and Dietrich Küchemann, the brilliant modest Engineer in the great German tradition, were endowed with very complementary talents which were essential in the founding phase of Euromech. In the 1960's, both men had definitely reached full maturity in their scientific careers.

In 1963, George Batchelor participated in the biennial Conference in Fluid Dynamics attended by European scientists from the East and the West and organized by Wladeck Fiszdon (Warsaw) in Poland. Both men came to the conclusion that greater cooperation between Eastern and Western researchers was very desirable. Highly supportive signals were also received from the Royal Society of London and IUTAM. At the 12th International Congress of Theoretical and Applied Mechanics held in Munich, representatives from six countries met on September 2, 1964, an Interim Committee for European Mechanics Colloquia (Euromech) was established, with Batchelor as Chairman and Küchemann as Secretary of the Committee.

The essential mission of Euromech would be the organisation of Colloquia, i.e. meetings of at most 50 scientists, focussing on a sufficiently specialized topic and leaving ample time for informal discussions. The 1st Euromech colloquium entitled “The Coanda effect” was held in April 1965, at the *Technische Universität Berlin*, under the chairmanship of Professor Rudolph Wille. The colloquium framework was highly successful with over 600 colloquia organised since 1965.

The proposals for colloquia were evaluated each year by the Euromech Colloquium Committee which, in its steady-state configuration, was composed of about ten co-opted scientists with diverse expertise in Fluid and later Solid Mechanics.

Even though the selection and support of colloquia proved to be the hallmark of Euromech, by the mid-eighties the Euromech Committee began to consider enlarging the scope of its activities via the organisation of several series of much larger European Conferences. These changes led in turn to the transformation of the European Mechanics Committee, in charge of Colloquia only, into the European Mechanics Society, in charge of Colloquia and ultimately of five series of European Conferences. During this transition period, the DAMTP at Cambridge very much remained at the helm of Euromech. In 1987, George Batchelor voluntarily resigned from being Chairman of Euromech. David Crighton also at DAMTP, became his successor.

George was no longer in charge but he remained strongly involved. Together with David Crighton and Hans Fernholz, they were the prime movers in this transformation phase. In his usual vigorous and friendly style, David Crighton became in 1994 the 1st President of the newly established European Mechanics Society, and Hans Fernholz its 1st Secretary-General. There are currently five series of conferences in Fluid Mechanics, Solid Mechanics, Turbulence, Mechanics of Materials and Nonlinear Oscillations.

After his resignation, George remained a regularly co-opted member of the Euromech Council. From 1990 to 1994 he became the 1st Chairman of the Standing Committee in charge of supervising the European Fluid Mechanics series of conferences (EFMC) during its launching phase. The 1st EFMC was held in Cambridge in 1991.

In 1994 G.K. Batchelor resigned from both the EFMC Standing Committee and the Euromech Council, putting an end to his involvement in the affairs of the society after 31 years of dedicated service. He spent his last years in the caring and affectionate company of his colleagues at DAMTP. He passed away on March 30th, 2000. In 1997 David fell very seriously ill and had to relinquish the Euromech presidency. Hans Fernholz, who had been closely associated with Euromech since its inception in the sixties, became his natural successor (1998–2002). It is a sad coincidence that David wrote a moving obituary of George one month before his own death in April 2000.

In 2003 the first Fluid Mechanics Prize was awarded to Keith Moffatt (Cambridge) and the first Solid Mechanics Prize to Franz Ziegler (Vienna). In 2005, the Council further created the status of Euromech Fellow.

George Batchelor maintained a friendly atmosphere among those involved in the “running” of Euromech, by keeping considerations of national pride and “political” strategies at bay. Over the years, participating in Euromech affairs has remained a gratifying experience. Euromech has grown into a major actor in the exchange of scientific information, the establishment of personal contacts and the collaboration between scientists in Europe. This is in large part due to George Batchelor’s visionary action.

References

[1] Fernholz HH. *The European Mechanics Society. From its Founding in 1964 to 2000*. Euromech, 2010.

*corresponding author: huerre@ladhyx.polytechnique.fr

Printing with Bubbles: Laser-Induced Forward Transfer of Complex Fluids

M. Jalaal[1,2*], M. Klein Schaarsberg[2], Detlef Lohse[2]

[1]Department of Applied Mathematics and Theoretical Physics, Centre for Mathematical Sciences, University of Cambridge, Cambridge CB3 0WA, UK
[2]Physics of Fluids Group, Max Planck Center for Complex Fluid Dynamics, MESA+ Institute and J.M. Burgers Centre for Fluid Dynamics, University of Twente, 7500 AE Enschede, The Netherlands

Introduction

Laser-induced forward transfer (LIFT) is a nozzle-free printing technology that can be used for two- and three-dimensional printing [1]. In our LIFT system, a nano-second laser pulse forms plasma and then creates a bubble inside a thin film. Using high-speed imaging, we show how the growth and collapse of the bubble dynamics lead to jet and eventually droplet formation. We theoretically identify the characteristic jetting velocity and define non-dimensional groups to classify the regimes of jetting of complex fluids. Based on the results, we propose optimal printing conditions.

Experiments

Figure 1a shows a schematic of the experimental setup for the investigation of LIFT[2]. A laser pulse passes through a $\lambda/2$ plate and a polarizing beam splitter (PBS), which serve to control the beam energy. We measure the energy of the laser with an energy-meter (EM). The laser is guided through a 10X objective lens (OL) and focused on a specified focal position. The side view is imaged with a high-speed camera attached to a long-distance microscope (LDM). The test-section is illuminated through back-light. The camera is protected with a notch filter. In the schematic, BD is the beam dump.

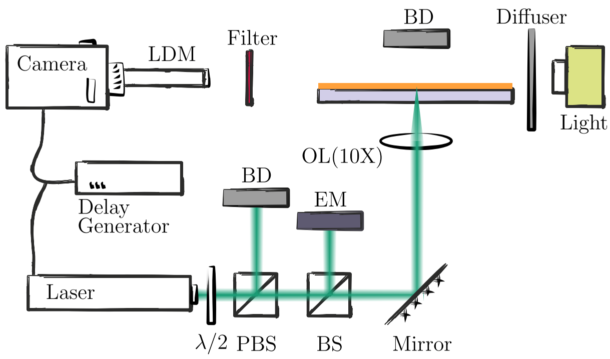

Fig. 1: a) Schematic of the experimental procedure.

Results

An example of the process of bubble and jet formation is show in figure 2. Optical breakdown results in plasma formation (shown by the black arrow in figure 2 and as a consequence a bubble forms inside the liquid (figure 2b) that contains vapour. The bubble grows initiating the liquid jet (figure 2c) and then collapses under hydrostatic pressure (shown by blue arrows in figure 2d). Meanwhile, the liquid jet is extending vertically (shown by the orange arrow in figure 2d). During the bubble collapse a downward *micro-jet* forms (due to the gravity, the presence of the wall and the free-surface). This *micro-jet* impacts on the bottom of the bubble, resulting in a complex toroidal shape of secondary bubbles (figure 2f). The formation of the crown seems to be highly connected to the second growth of the bubble; when it pushes the perimeter around the jet and forms a crown.

We performed experiments for Newtonian and yield stress materials. Several parameters such as the laser energy (E), focal height, and the rheology of the material determine the shape of the jet, that can vary from bumps, jets with stable or unstable crowns, and fragmented jets, to sprays (see figure 3a). In most applications, a non-fragmenting straight jet is desirable. To look for the suitable conditions, we reduce the parameter space into two non-dimensional groups, namely the Weber and Reynolds numbers:

$$We = \frac{\rho U_0^2 z_f}{\sigma} \quad \text{and} \quad Re = \frac{\rho U_0^2}{K\left(U_0/z_f\right)^n + \tau_0}. \tag{1}$$

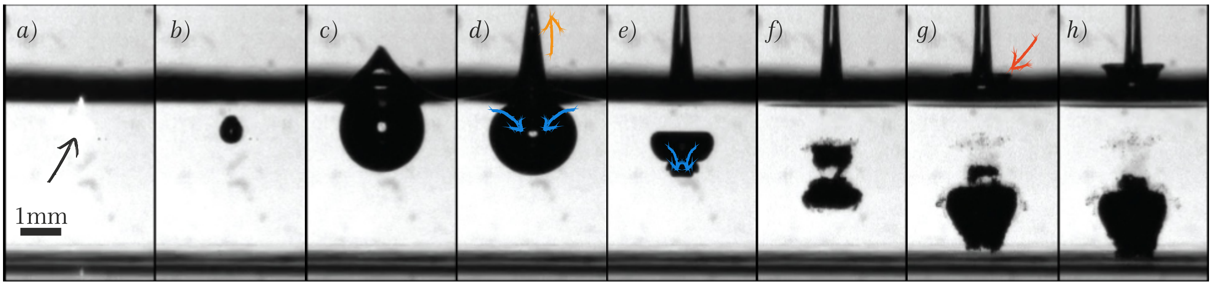

Fig. 2: Process of bubble, jet, and crown formation in a film. Snapshot correspond to a) $t = 0\,\mu$s, b) $t = 5\,\mu$s , c) $t = 125\,\mu$s, d) $t = 250\,\mu$s, e) $t = 350\,\mu$s, f) $t = 450\,\mu$s, g) $t = 575\,\mu$s, h) $t = 625\,\mu$s.

Where, ρ and σ are density and surface tension, respectively, and z_f is the distance of the focal point from the surface. Also, K, n, τ_0 are consistency index, flow index, and yield stress, respectively. U_0 is the early stage jet velocity in which was calculated theoretically[3].

Figure 3b shows the experimental phase map based on these numbers. Our results suggest operating conditions that satisfy the two conditions of $0.075 < Oh < 0.2$ and $Re > 200$, where $Oh = We^{1/2}/Re$ is the Ohnesorge number. Outside these ranges, the viscous dissipation (due to the shear-thinning and plastic viscosities) is either too large to avoid jetting or too small to make a stable straight jet. We note that the conditions above are for jet formation only. Depending on the technical details of printing, additional conditions can be introduced for optimal printing. For instance, one should avoid splashing when droplets are deposited on the surface.

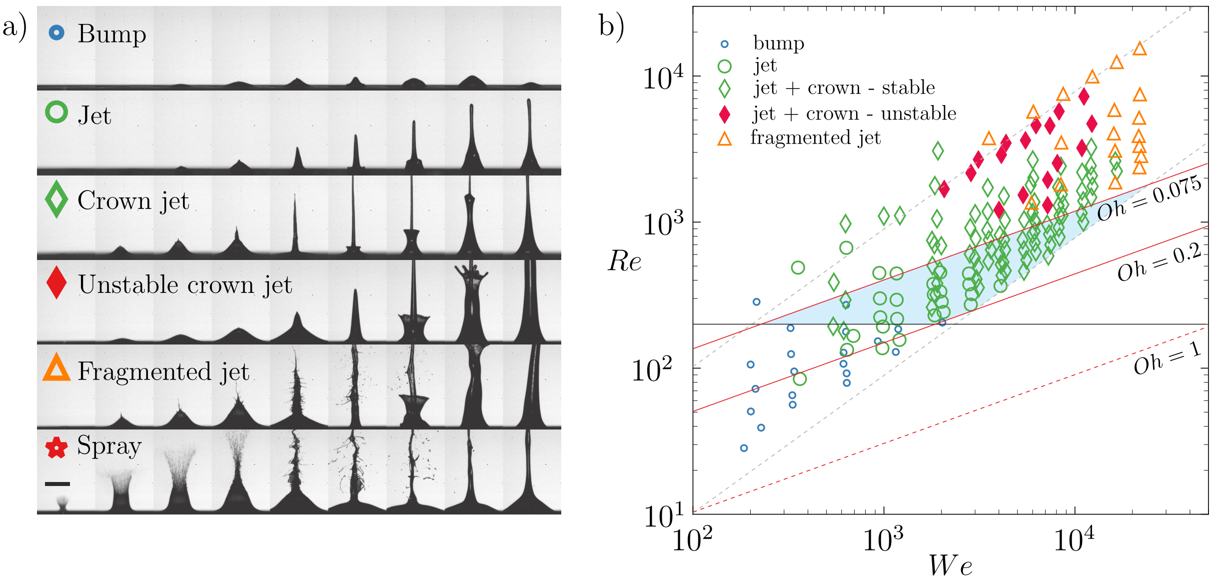

Fig. 3:) Examples of the jetting regimes observed in the experiments. The experimental conditions from top to bottom: *bump*: $E = 2.1$ mJ, $z_f/H = 0.75$, $\tau_0 = 67$Pa; *jet*: $E = 2.7$ mJ, $z_f/H = 0.5$, $\tau_0 = 75$Pa; *jet with a crown*:$E = 2.6$ mJ, $z_f/H = 0.25$, $\tau_0 = 35$Pa; *jet with an unstable crown*: $E = 6.3$ mJ, $z_f/H = 0.75$, $\tau_0 = 20$Pa; *fragmented jet*: $E = 6.4$ mJ, $z_f/H = 0.25$, $\tau_0 = 20$Pa; *spray*: $E = 6.3$ mJ, $z_f/H = 0$, $\tau_0 = 35$Pa. Phase space in terms of Reynolds and Weber number. The optimal printing condition is highlighted.

References

[1] Serra P & Pique A. *Advanced Materials Technologies* p. 1800099, 2018.
[2] Jalaal M et al. *Applied Physics Letter* **114(21)**:213703, 2019.
[3] Jalaal M et al. *Journal of Fluid Mechanics* **880**:497513, 2019.

*corresponding author: mj547@cam.ac.uk

Life and fate of a bubble in a constricted Hele-Shaw channel

A. Gaillard[1], J. S. Keeler[2], A. B. Thompson[2], A. L. Hazel[2], A. Juel[1]

[1] Manchester Centre for Nonlinear Dynamics and Department of Physics & Astronomy, University of Manchester, UK
[2] Department of Mathematics and Manchester Centre for Nonlinear Dynamics, University of Manchester, UK

Introduction

Two-phase displacement flow in a confined geometry is a fundamental problem in fluid mechanics with applications in biomechanics, geophysics and industry. A canonical example is the viscous fingering instability which occurs when air displaces a viscous fluid in a Hele-Shaw channel of width much greater than its depth. An initially flat interface evolves into a single finger of air, symmetric about the centreline of the channel [1]. When the nondimensional driving flux is above a threshold, which depends on the roughness of the channel, this finger is observed to become unstable to tip-splitting leading to the emergence of complex patterns [2]. As the steady solution is linearly stable for all computed flow rates [3], these further instabilities must arise subcritically. For both air fingers (i.e. of semi-infinite extent) and bubbles (with fixed volume), models of the system also contain alternative, weakly-unstable families of multiple-tipped symmetric solutions and asymmetric solutions in addition to the linearly stable solution branch [4].

Recent experiments and numerical simulations [4] have shown that with the introduction of a depth-perturbation to the bottom of the channel henceforth referred to as a rail (Fig. 1a,b), the system retains similar modes of finger or bubble propagation as in the Hele-Shaw channel of rectangular cross-section, but their stability is altered so that several stable invariant solutions occur for the same imposed flow rates, as indicated by the solid lines in the numerical bifurcation diagram of Fig. 1c.

Hence, several long-term invariant outcomes are possible for a bubble propagating from a centred initial position but the bubble may also undergo changes in topology by breaking up into multiple bubbles [5]. In this talk, we characterise the transient evolution of propagating bubbles from controlled initial conditions. We compare our results with numerical simulations which indicate that when the flow-rate is large enough the bubble evolution is guided by transient exploration of the stable manifolds of weakly unstable two-bubble edge states of the system [5].

Experiment

The experimental channel is shown schematically in Fig.1a,b. The channel aspect ratio is fixed at 40, and the rail occupies 25% of the channel width and 2.4% of its height. An air bubble of controlled volume is injected at one end of the channel and propagated by infusing silicone oil at a constant flow rate with a non-dimensional flow rate $Q = \mu Q^*/(W^* H^* \sigma)$, where μ is the dynamic viscosity of the oil, σ the surface tension, $W^* H^*$ the cross-section of the unoccluded channel and Q^* the dimensional flow rate. We impose controlled initial conditions by deforming a centred bubble to a width $b = b^*/W^*$, and propagating it from rest. We track its evolution in top-view with a camera that moves with the bubble.

Results

We find that depending on the initial bubble shape and the value of the flow rate, an initially centred bubble may evolve towards the on-rail or off-rail invariant modes (see Fig. 1c) or undergo a change

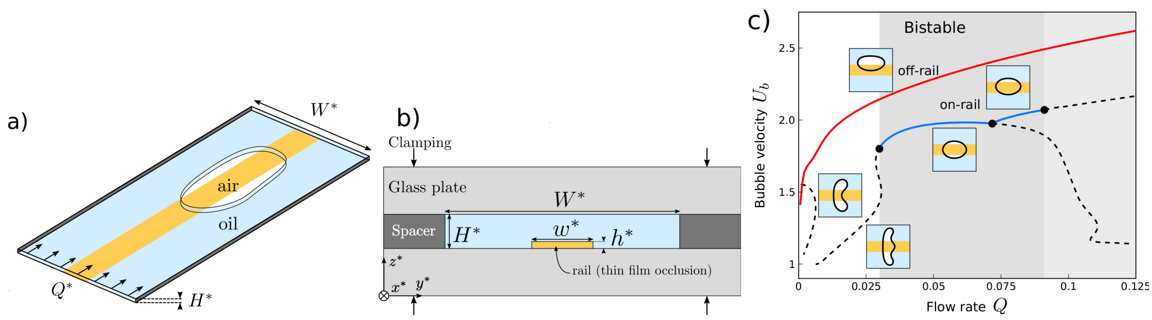

Fig. 1: (a) Top-view of the experimental channel with an axially uniform, centred rail. (b) Cross-section of the channel. (c) Numerical bifurcation diagram depicting the steady modes of bubble propagation in terms of the bubble velocity as a function of the flow rate [5]. Stable and unstable modes are indicated by solid and dashed lines, respectively.

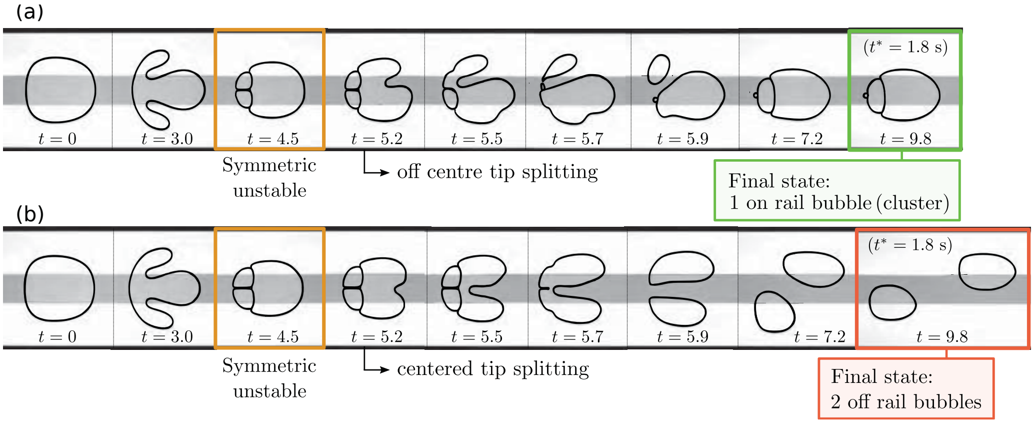

Fig. 2: Examples of experimentally-observed transient bubble dynamics showing bubble breakup and recombination, leading to distinct outcomes (a) the compound bubble will eventually recombine to a single bubble and (b) two asymmetric bubbles which will eventually drift apart.

in topology by breaking up into two bubbles, whose relative distance increases as they propagate. There is a rich variety of transient evolution scenarios leading to these long-term outcomes, which each occurs in well-defined regions of the parameter plane spanning flow rate and initial bubble width. Above a threshold flow rate, initially slender bubbles tend to evolve towards on-rail invariant modes, whereas initially wide bubbles typically break up into two separating bubbles. Examples of these long-term outcomes are shown in the images of the final states in Fig. 2.

For initially wide bubbles, the early-time evolution is to a double-tipped bubble reminiscent of the weakly unstable state shown in Fig. 1 leading to break-up into two bubbles on either side of the rail. These two newly formed bubbles may either remain on separate sides of the rail or one may migrate over the rail to recombine with the other. Numerical simulations of this process indicate that the evolution of this newly formed two-bubble system is orchestrated by weakly unstable two-bubble steady solutions whose existence depends on the flow rate and the relative bubble sizes.

For more slender bubbles, the early-time evolution is to a triple-tipped bubble similar to the unstable steady solution in Fig. 1c. A typical evolution is shown in the first three snapshots in Fig. 2(a-b). The resulting compound bubble then breaks up into two bubbles which either recombine into an on-rail asymmetric compound bubble (a) or separate indefinitely (b). Fig. 2 also illustrates the sensitivity of the system at high flow rate since both figures correspond to the same initial condition within experimental resolution. In fact, as the flow rate is increased, the evolution becomes increasingly disordered and the bubble can break up into multiple parts, some of which are sufficiently small to rapidly separate from the larger bubbles as they propagate, resulting in a loss of volume of the remaining parts.

Conclusion

This system exhibits rich transient evolutions, some of which involving bubble breakup into two or more bubbles, and can be followed by other topological reorganisations of the system. In the long term, either a single steadily-propagating bubble may be recovered or multiple bubbles remain, whose relative distance increases with time. We find numerically that these dynamics are orchestrated by weakly-unstable, two-bubble edge states of the system. As the flow rate increases, transient bubble shapes are increasingly deformed and the number of breakups and recombinations undergone by the bubble increases. We suspect that this increase in complexity is due to a subcritical transition to disorder above a threshold that depends on the roughness of the occlusion, reminiscent of the transition to turbulence in shear flow.

References

[1] Saffman, P.G. & Taylor, G.I. (1958) The penetration of a fluid into a porous medium or Hele-Shaw cell containing a more viscous liquid. *Proc. R. Soc. A* **245** 312-329.

[2] Tabeling, P., Zocchi, G. & Libchaber, A. (1987) An experimental study of the Saffman-Taylor instability. *J. Fluid Mech.* **177**, 67-82.

[3] Bensimon, D. (1986) Stability of viscous fingering. *Phys. Rev. A* **33** 1302-1308.

[4] Franco-Gómez, A., Thompson, A. B., Hazel, A. L. & Juel, A. (2016) Sensitivity of Saffman-Taylor fingers to channel-depth perturbations. *J. Fluid Mech* **794**, 343-368.

[5] Keeler, J.S., Thompson, A.B., Lemoult, G., Juel, A. & Hazel, A.L. (2019) The influence of invariant solutions on the transient behaviour of an air bubble in a Hele-Shaw channel. *Proc. R. Soc. A* **475**, 20190434.

*corresponding author: anne.juel@manchester.ac.uk

An ultimate state in "wall-bounded" convective turbulence

Genta Kawahara[1]*, Kouki Kawano[1], Shingo Motoki[1], Masaki Shimizu[1]

[1]Graduate School of Engineering Science, Osaka University, Toyonaka 560-8531, Osaka, Japan

Introduction

Rayleigh–Bénard convection is one of the most canonical turbulent flows. It is thermal convection driven by buoyancy, and dimensionless parameters in this system are the Rayleigh number Ra and the Prandtl number Pr. At low Ra wall-to-wall heat flux is given by thermal conduction. When Ra is increased, thermal convection arises and eventually convective turbulence appears to drastically enhance the heat flux. The dimensionless wall-to-wall heat flux normalized with the thermal conduction heat flux is the Nusselt number Nu. A large number of experiments and numerical simulations have been performed, and the scaling law $Nu \sim Ra^{0.31}$ have been commonly observed at $Ra \sim 10^8 - 10^{11}$ (see e.g. He *et al.* 2012). Grossmann & Lohse (2000) have proposed the scaling theory of Nu with Ra and Pr. Their theory gives us the scaling $Nu \sim Ra^{1/3}$ in the high-Ra range $Ra \sim 10^8 - 10^{14}$ for $Pr \sim 1$.

It has long been anticipated that at extremely high Ra, both thermal and kinetic energy dissipation ϵ are dominated by the bulk region rather than the thermal and kinetic boundary layers, leading to the so-called ultimate scaling $Nu \sim Ra^{1/2}$ (Kraichnan 1962; Grossmann & Lohse 2000). However, the ultimate scaling has not been observed even at very high Ra as yet. Recently, it has been reported that even the introduction of surface roughness on the wall cannot bring about the ultimate scaling (Zhu *et al.* 2017).

In this study we investigate turbulent thermal convection between horizontal no-slip, permeable plates heated from below and cooled from above by numerically solving the Boussinesq equation for $Pr = 1$. We have found that wall permeability brings about the ultimate scaling $Nu \sim Ra^{1/2}$.

Scaling of the Nusselt number with the Rayleigh number

We perform direct numerical simulations for convective turbulence between the horizontal plates with the distance H and the temperature difference ΔT using a Fourier–Chebyshev spectral method. The no-slip, permeable conditions, $u = v = 0$ and $w = -\beta p'/\rho, +\beta p'/\rho$ (Jiménez *et al.* 2001), are imposed on the plate surfaces $z = 0, H$. The permeability parameter is fixed at $\beta(g\alpha\Delta TH)^{1/2} = 0$ (impermeable case), 3 (permeable case), where $(g\alpha\Delta TH)^{1/2}$ denotes the buoyancy-induced terminal velocity. The Prandtl number is set to unity, and the horizontal period is taken to be H.

Figure 1 shows the Nusselt number Nu as a function of the Rayleigh number $Ra = g\alpha\Delta TH^3/(\nu\kappa)$. In the impermeable case $\beta(g\alpha\Delta TH)^{1/2} = 0$, at high $Ra \sim 10^8 - 10^{10}$ the Nusselt number can be seen to

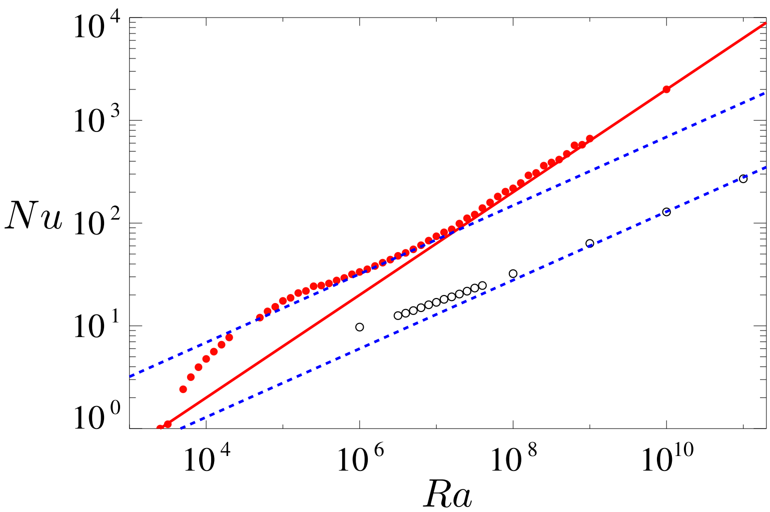

Fig. 1: The Nusselt number Nu as a function of the Rayleigh number Ra. The Prandtl number is fixed at $Pr = 1$. The closed red circles represent the permeable case $\beta(g\alpha\Delta TH)^{1/2} = 3$ while the open black circles denote the impermeable case $\beta(g\alpha\Delta TH)^{1/2} = 0$. The solid red line and the dashed blue line stand for the scalings $Nu \sim Ra^{1/2}$ and $Nu \sim Ra^{1/3}$, respectively.

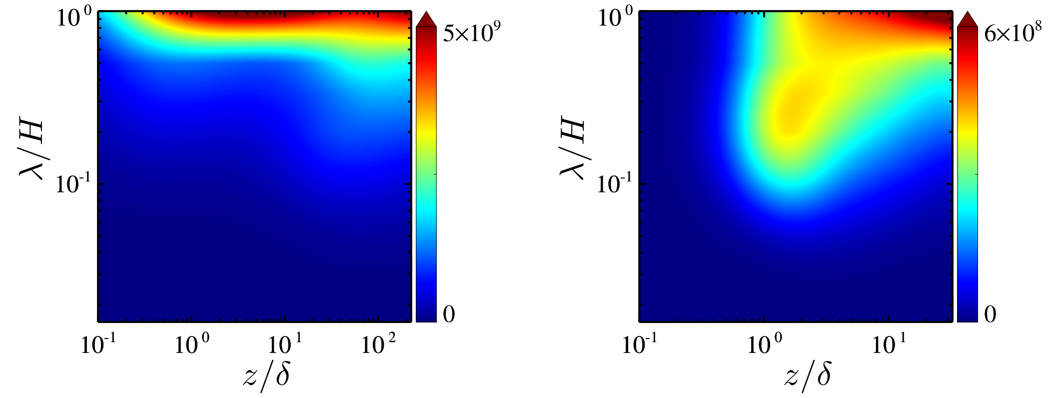

Fig. 2: Premultiplied spectra of buoyancy power $g\alpha Tw$ as a function of the horizontal wavelength λ and the distance to the lower wall z in the permeable case $\beta(g\alpha\Delta TH)^{1/2} = 3$ (left) and the impermeable case $\beta(g\alpha\Delta TH)^{1/2} = 0$ (right) at $Ra = 10^8$ for $Pr = 1$. $\delta = \Delta T/\mathrm{d}\overline{T}/\mathrm{d}z|_{z=0}$ represents the thermal conduction length.

scale with the Rayleigh number as $Nu \sim Ra^{1/3}$, nearly consistent with the well-known turbulent scaling law $Nu \sim Ra^{0.31}$ (see e.g. He *et al.* 2012). In the permeable case $\beta(g\alpha\Delta TH)^{1/2} = 3$, on the other hand, the ultimate scaling $Nu \sim Ra^{1/2}$ can be observed undoubtedly at higher $Ra = 10^8 - 10^{10}$, whereas the ordinary scaling $Nu \sim Ra^{1/3}$ is confirmed at lower $Ra \sim 10^6$. It is worthy of note that the scaling property of Nu critically changes at $Ra \sim 10^7$ from $Nu \sim Ra^{1/3}$ to $Nu \sim Ra^{1/2}$ with increasing Ra. Even in the permeable case, at lower $Ra \sim 10^6$ we have not observed significant wall-normal transpiration velocity (figure not shown) in the near-wall region, implying that the ultimate scaling cannot be achieved.

Discussion on ultimate scaling

Premultiplied spectra of buoyancy power $g\alpha Tw$ are shown in figure 2 as a function of the horizontal wavelength λ and the distance to the lower wall z in the permeable case $\beta(g\alpha\Delta TH)^{1/2} = 3$ and the impermeable case $\beta(g\alpha\Delta TH)^{1/2} = 0$ at $Ra = 10^8$ for which the ultimate scaling has been observed in the permeable case (see figure 1). In the impermeable case the significant buoyancy power can be seen for small-horizontal-scale motion, i.e. near-wall plumes, in the vicinity of the wall $z/\delta \sim 10^0$. In the permeable case, on the other hand, even in the the vicinity of the wall $z/\delta \sim 10^0$ the large-horizontal-scale motion can be induced by buoyancy.

Let us discuss this remarkable difference in the near-wall length scale between the permeable and the impermeable case, leading to difference in the Nu scaling. In the permeable case at higher $Ra \sim 10^8 - 10^{10}$ significant wall-normal transpiration velocity is induced even in the near-wall region (figure not shown). Therefore, although the thermal conduction layer still exists on the wall, there is no near-wall layer of the wall-normal (vertical) velocity in the higher-Ra permeable case, suggesting that there would not appear small-scale vertical motion in the near-wall region where the effects of the viscosity on the vertical velocity is negligible. The vertical motion should exhibit the length scale comparable with H anywhere, and thus the balance between the dominant buoyancy and inertial terms in the vertical Boussinesq equation gives us the velocity scale of the order of the buoyancy-induced terminal velocity $(g\alpha\Delta TH)^{1/2}$. Then the energy budget equation, including pressure power on the permeable plates (being an energy sink and comparable with ϵ), provides us with the Taylor's dissipation law $\epsilon \sim (g\alpha\Delta TH)^{3/2}/H$ as well as the ultimate scaling $Nu \sim Ra^{1/2}$ in the higher-Ra permeable case.

References

[1] Grossmann S., Lohse, D. Scaling in thermal convection: a unifying theory. *J. Fluid Mech.* **407**: 27–56, 2000.

[2] He X., Funfschilling, D., Nobach, H., Bodenschatz, E., Ahlers, G. Transition to the ultimate state of turbulent Rayleigh–Bénard convection. *Phys. Rev. Lett.* **108**: 024502, 2012.

[3] Jiménez J., Uhlmann M., Pinelli A., Kawahara G. Turbulent shear flow over active and passive porous surfaces. *J. Fluid Mech.* **442**: 89–117, 2001.

[4] Kraichnan R. H. Turbulent thermal convection at arbitrary Prandtl number. *Phys. Fluids* **5**: 1374–1389, 1962.

[5] Zhu X., Stevens R. J. A. M., Verzicco R., Lohse D. Roughness-Facilitated Local 1/2 Scaling Does Not Imply the Onset of the Ultimate Regime of Thermal Convection. *Phys. Rev. Lett.* **119**: 154501, 2017.

*corresponding author: kawahara@me.es.osaka-u.ac.jp

Physicochemical Hydrodynamics of Droplets out of Equilibrium

Detlef Lohse [1]*

[1]Physics of Fluids Group & Max Planck Center, Univ. of Twente, PO Box 217, 7500AE Enschede, Netherlands

Classical hydrodynamics focuses on pure liquids. In nature and technology, fluid dynamical systems are however *multicomponent*, and often with gradients in concentration, even changing in time, i.e., they are out of equilibrium. These concentration gradients, be they smooth or sharp, can induce a flow. Moreover, phase transitions can occur, with either evaporation, solidification, dissolution, or nucleation of a new phase. The liquids can be binary, ternary, or contain even more components, with several across different phases. The non-equilibrium can be driven by flow, mixing, phase transitions, chemical reactions, electrical current, heat, etc.

To theoretically deal with such systems, in the 1950s, Levich wrote the wonderful book "Physicochemical Hydrodynamics" [1]. The central theme of the book is the "elucidation of mechanisms of transport phenomena and the conversion of understanding so gained into plain, useful tools for applications," as L. E. Scriven describes it in the foreword to the book in its 1962 translation into English [1]. Levich can be viewed as a physical chemist and theoretical physicist at the same time, or, as Scriven puts it, above all, as an "engineering scientist" with a recognizable "blend of applied chemistry, applied physics, and fluid mechanics." V. Levich himself, in his foreword to the first Russian Edition (1952), describes the scope of physicochemical hydrodynamics as the "aggregate of problems dealing with the effect of fluid flow on chemicals or physicochemical transformations as well as the effect of physicochemical factors of the flow."

First and foremost, Levich's "Physicochemical hydrodynamics" is a book describing the relevant theoretical and mathematical concepts, given that in those days the experimental tools to actually measure the flow on the microscale were very limited and the possibility to perform direct numerical simulations of the underlying partial differential equations even absent. Today, more than 60 years later, the scientific and in particular the hydrodynamical and physicochemical communities have developed tremendously and the experimental, instrumental, and numerical means to actually deal with the problems Levich defined in his book have become available and are being used to do so.

These developments are more than timely, as the relevance of physicochemical hydrodynamics of multicomponent and multiphase liquids is ever increasing, in order to address the challenges of mankind for the 21st century. These challenges include energy, namely storage and batteries, hydrogen production by electrolysis, CO_2 capture, polymeric solar cell manufactering, biofuel production, and catalysis. They also include health and medical issues like chemical analysis and diagnostics or the production and purification of drugs, advanced material manufacturing, environmental issues like flotation, water cleaning, membrane management, and separation technology, or food processing and food safety issues. They also include issues in modern production technologies such as additive manufacturing on ever decreasing length scales and inkjet printing, and in the paint and coating industry.

These challenges have often been approached with a pure engineering approach, and less in the spirit of Levich as an engineering scientist. On the other hand, as said above, classical hydrodynamics has focused on pure and single-phase liquids. In the last two decades, the advent of new experimental and numerical tools has allowed for a more integrated understanding of physicochemical hydrodynamics and to further narrow the gap between classical hydrodynamics and chemical engineering and colloid & interfacial science. The objective of this effort is to improve the *quantitative* understanding of multicomponent and multiphase fluid dynamic systems far from equilibrium, in order to master and better control them. To achieve this objective, one has to perform controlled experiments and numerical simulations for idealized setups, allowing for a *one-to-one comparison* between experiments and numerics/theory, in order to test the theoretical understanding. This effort indeed is in the spirit of Levich's "Physicochemical Hydrodynamics", but now building on and benefiting from the developments of modern microfluidics, microfabrication, digital (high-speed) imaging technology, confocal microscopy, atomic force microscopy, and various computational techniques and opportunities for high-performance computing. These are, in a nutshell, the blessings from what can be considered as the golden age of fluid dynamics, which builds on the digital revolution, both on the experimental and the numerical side. Given these developments, and given the necessity in chemical engineering to move towards higher precision and enhanced control, this effort is indeed very timely.

There is a large number of physical phenomena and effects which come into play in multicomponent and multiphase liquids far from equilibrium. These include gradients in concentration, either in the bulk of the liquid or on the surface, leading to solutal Marangoni flow and diffusiophoresis. They include (selective) dissolution of (multicomponent) droplets and bubbles in host liquids or vice versa their nucleation and growth. They also include the coalescence of droplets consisting of different liquids, possibly with chemical reactions and/or solidification and other transitions from one phase to another. The material parameters which become important are the various diffusivities and viscosities of the liquids, their surface tensions and how they depend on the concentrations, the volatilities and mutual solubilities, latent heats, reaction rates, etc.

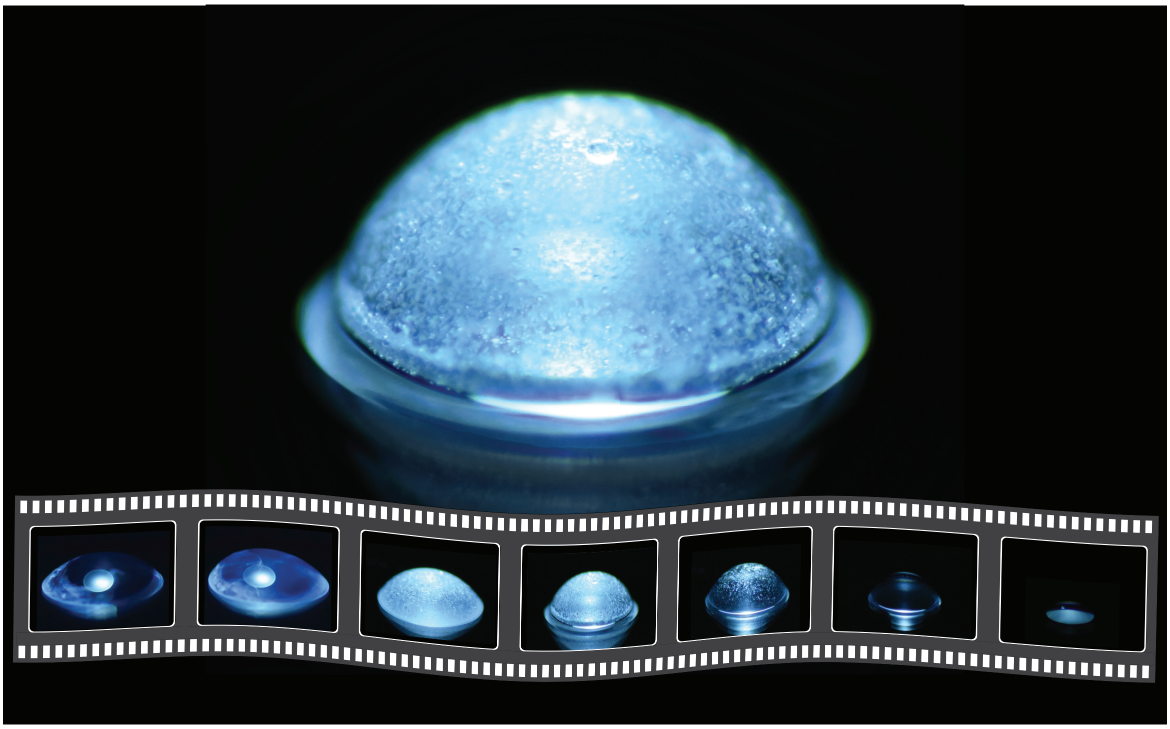

Fig. 1: *Evaporating ouzo droplet: Optical image of the droplet after phase separation, with a milky droplet sitting on an oil ring. The seven insets show earlier and later snapshots of the droplet. Figure based on our work in ref. [2].*

In this talk I will restrict myself to multiphase hydrodynamical systems at small length scales, focusing on the physicochemical hydrodynamics of (multicomponent) droplets far from equilibrium. The objective is to show examples of such systems for which a successful quantitative description and one-to-one comparison between well-controlled table-top experiments and theory and numerics has been achieved, to identify the complex interplay of the underlying principles, The discussed examples include immiscible droplets in a concentration gradient [3], coalescence of droplets of different liquids, droplets in concentration gradients emerging from chemical reactions and phase transitions such as evaporation [4], dissolution, or nucleation [2, 5], and droplets in ternary liquids, including solvent exchange, nano-precipitation, and the so-called ouzo effect, which, for the case of an evaporating ouzo droplet, is shown in figure 1.

I will also briefly discuss the relevance of the physicochemical hydrodynamics of such droplet systems for many important applications, including in chemical analysis and diagnostics, microanalysis, pharmaceutics, synthetic chemistry and biology, chemical and environmental engineering, the oil and remediation industries, inkjet-printing, for micro- and nano-materials, and in nanotechnolgoy.

References

[1] V. G. Levich, *Physicochemical hydrodynamics* (Prentice Hall, Englewood Cliffs, 1962).

[2] H. Tan, C. Diddens, P. Lv, J. G. M. Kuerten, X. Zhang, and D. Lohse, *Evaporation-triggered micro-droplet nucleation and the four life phases of an evaporating Ouzo drop*, Proc. Nat. Acad. Sci. **113**, 8642 (2016).

[3] Y. Li, C. Diddens, A. Prosperetti, K. L. Chong, X. Zhang, and D. Lohse, *Bouncing Oil Droplet in a Stratified Liquid and its Sudden Death*, Phys. Rev. Lett. **122**, 154502 (2019).

[4] Y. Li, C. Diddens, P. Lv, H. Wijshoff, M. Versluis, and D. Lohse, *Gravitational effect in evaporating binary microdroplets*, Phys. Rev. Lett. **122**, 114501 (2019).

[5] C. Diddens, H. Tan, P. Lv, M. Versluis, J. G. M. Kuerten, X. Zhang, and D. Lohse, *Evaporating pure, binary and ternary droplets: thermal effects and axial symmetry breaking*, J. Fluid Mech. **823**, 470 (2017).

*corresponding author: d.lohse@utwente.nl

Particle-Fluid Interaction in a Turbulent Boundary Layer

E. K. Longmire*, Y. H. Tee

Dept of Aerospace Engineering and Mechanics, University of Minnesota
Minneapolis, Minnesota, 55455 USA

Introduction and Methodology

In this work, we investigate how wall friction and coherent structures within a boundary layer can affect particle transport and suspension. We consider the detailed motion of spheres released from rest within a turbulent boundary layer and investigate particle-wall and particle-turbulence interactions. Depending on the friction Reynolds number and the sphere-to-fluid density ratio, the spheres can either slide or roll along the bounding surface as well as lift off from or collide with the wall.

The experiments are performed in a recirculating water channel with a turbulent boundary layer developing along the bottom wall. The glass test section is 8 m long and 1.12 m wide. Individual magnetic wax spheres with diameter d = 6.35 mm and specific gravities of 1.006 (P1), 1.054 (P2) and 1.152 (P3) are released from rest on a smooth wall. We consider two friction Reynolds numbers, Re_τ = 680 and 1320 (d^+ = 58 and 122 viscous units) with boundary layer thicknesses, δ = 73 and 69 mm respectively. Each sphere is initially held at rest by a magnet before being released and allowed to propagate with the flow. Small markers are painted on the sphere surface and tracked in three-dimensional space using LED illumination and sequential pairs of cameras in stereoscopic configuration viewing through the side wall. The sphere rotation and translation are tracked over a streamwise distance of 5.5δ using the method outlined in [1]. The coordinates x, y and z denote the streamwise, wall-normal and spanwise directions.

To track the fluid motion, simultaneous stereoscopic PIV experiments are conducted using two high-speed cameras positioned under the channel. The flow is seeded with 13-micron silver-coated hollow glass beads. An Oxford Firefly 300W infrared laser (wavelength: 808 nm), looking from the side wall, illuminates a thin sheet in the x-z plane of the flow field. Following Adhikari's methodology [2], infrared-block and pass optical filters are mounted to the lenses of the tracking and PIV cameras, respectively. The PIV images are calibrated and cross-correlated in Davis 10.1, and a spatial automask function is implemented to mask out the sphere and shadow. The mean flow statistics of the unperturbed turbulent boundary layers were determined separately from PIV measurements in x-y planes.

Results and Conclusions

Spheres with a density ratio of 1.006 always lifted off the wall upon release, translated with minimal rotation, and subsequently fell back toward the wall. After these spheres had accelerated significantly, they frequently lifted off to even greater heights. While the initial lift off events agree well with the mean lift on fixed spheres estimated by Hall's correlation [3], these subsequent lift-off events, which occurred at much smaller relative velocities, are attributed to coherent structures in the flow. By contrast, spheres with density ratio of 1.152 exhibited completely different behavior. They did not lift off upon release, also in agreement with Hall's correlation [3]. Instead, they slid along the wall over distances greater than δ before eventually developing some forward rotation. This forward rotation was often accompanied by additional rotations about the wall-normal and streamwise axes. Further, the forward rotation was accompanied by repeated weak lift-offs occurring at relatively high frequency which we attribute to a Magnus lift force. For this larger density ratio, wall friction was significant in impeding acceleration as well as eventually in helping initiate rotation. All sphere-wall collisions were completely inelastic, a result consistent with collisions characterized by relatively low Stokes number in simpler flows [4].

The SPIV measurements help explain the large variability in sphere velocity and trajectory observed across many runs under like conditions. A sample sequence of fields surrounding sphere P1 is shown in Fig. 1a. In this case, the sphere is enveloped by and translates within a long streamwise region of relatively slow moving fluid. The sphere continues to lag the fluid through the sequence with a particle Reynolds number of $\sim$ 230 based on relative velocity between surrounding fluid and sphere, and its translational velocity is relatively low compared with the average computed over many runs (see Fig. 1b). A contrasting sequence (not shown), includes a sphere enveloped and dragged downstream by a long streamwise region of fast moving fluid.

Detailed results on sphere lift off and rotation as well as the surrounding fluid velocity fields will be presented and discussed.

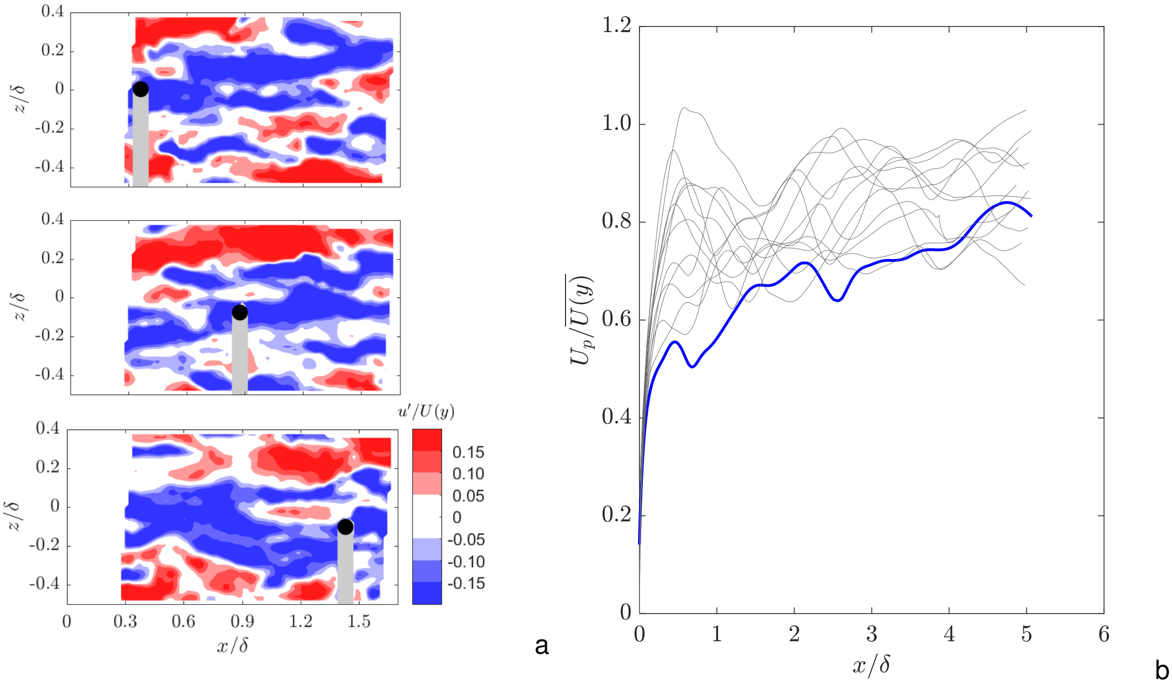

Fig. 1: Sphere P1 at Re_τ = 680. (a) Time-resolved fluctuating streamwise fluid velocities (u') normalized by the mean fluid velocity ($\overline{U(y)}$) across the streamwise-spanwise plane at y^+ = 37 or y = 0.63d. Grey region under the sphere represents its shadow. (b) Sphere streamwise velocity (U_p) normalized by mean fluid velocity at the height of the sphere centroid for 13 runs. Blue curve corresponds with the sample result shown on the left.

References

[1] Barros D et al. *Exp Fluids* **59**:104, 2018.
[2] Adhikari D & Longmire EK. *Meas Sci Technol* **24(2)**:024011, 2013.
[3] Hall D. *J Fluid Mech* **187**:451–466, 1988.
[4] Gondret P et al. *Phys Fluids* **14**:643-652, 2002.

*corresponding author: longmire@umn.edu

Alternative physics to understand wall turbulence: Navier–Stokes equations with modified linear dynamics

A. Lozano-Durán[1]*

[1]Center for Turbulence Research, Stanford University, CA 94305, USA

Introduction

One aspect particularly beautiful about numerical simulations is the freedom to perform conceptual experiments that break with our current laws of physics. These experiments, even if inconsistent with the physics of our world, provide invaluable information about the dynamics of a system. In this study, I present a collection of numerical experiments in which the Navier–Stokes equations are sensibly modified to understand the role of different physical mechanisms.

The focus of this study is on self-sustaining wall turbulence. Despite the fact that turbulence is a primary example of a highly nonlinear phenomenon, there is ample agreement that the energy-injection mechanisms from the base flow into the fluctuating field (Fig. 1a) can be partially attributed to linear processes [1]. The different mechanisms have their origins in linear stability theory [2, 3, 4, 5, 6] and constitute the foundations of many control and modeling strategies [7, 8]. The possible scenarios comprise exponential instabilities from mean-flow inflection points, transient growth from non-normal operators, and parametric instabilities from temporal mean-flow variations, among others. These mechanisms, each potentially capable of leading to the observed turbulence structure, are rooted in simplified theories and conceptual arguments. Whether the flow follows any or a combination of them remains unclear.

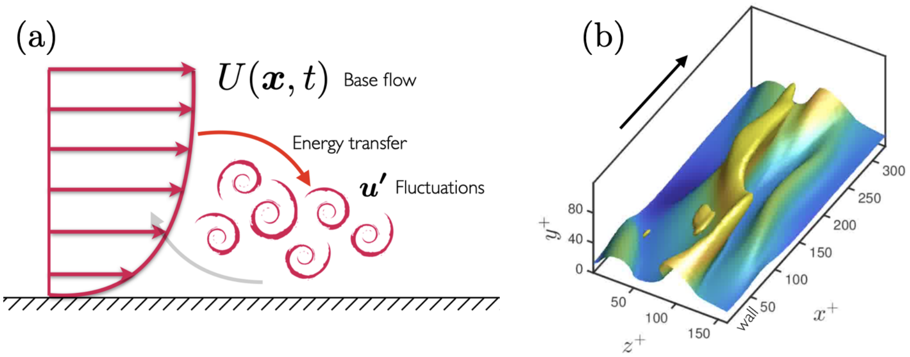

Fig. 1: (a) Sketch of the energy transfer from the base flow to the fluctuating flow. (b) Numerical experiment: isocontour of the streamwise velocity equal to 0.8 of the maximum value.

Methods

To investigate the role of different linear mechanisms, we examine data from spatially and temporally resolved simulations of an incompressible turbulent channel flow driven by a constant mean pressure gradient. Hereafter, the streamwise, wall-normal, and spanwise directions of the channel are denoted by x, y, and z, respectively, and the corresponding flow velocity components and pressure by u, v, w, and p. The density of the fluid is ρ and the channel height is h. The wall is located at $y = 0$, where no-slip boundary conditions apply, whereas free stress and no penetration conditions are imposed at $y = h$. The streamwise and spanwise directions are periodic. The grid resolution of the simulations in x, y, and z is $64 \times 90 \times 64$, respectively, which is fine enough to resolve all the scales of the fluid motion.

The Reynolds number selected is $\mathrm{Re}_\tau = \delta/\delta_v \approx 180$, which provides a sustained turbulent flow at an affordable computational cost [9]. The streamwise, wall-normal, and spanwise sizes of the computational domain are $L_x^+ \approx 337$, $L_y^+ \approx 186$, and $L_z^+ \approx 168$, respectively, where the superscript $+$ denotes quantities normalized by ν and u_τ. Jimenez & Moin [10] showed that turbulence in such domains contains an elementary flow unit comprised of a single streamwise streak and a pair of staggered quasi-streamwise vortices, which reproduce the dynamics of the flow in larger domains (Fig. 1b).

We focus on the dynamics of the fluctuating velocities $\boldsymbol{u}' \equiv (u', v', w')$, defined with respect to the streak base flow $U(y, z, t) \equiv \langle u(x, y, z, t)\rangle$, where $\langle\cdot\rangle$ denotes average in the streamwise direction, and such that $u' \equiv u - U$, $v' \equiv v$, and $w' \equiv w$. The fluctuating velocity vector $\boldsymbol{u}' \equiv (u', v', w')$ is governed by

$$\frac{\partial \boldsymbol{u}'}{\partial t} = \mathcal{L}(U)\boldsymbol{u}' + \boldsymbol{N}(\boldsymbol{u}'), \tag{1}$$

where $\mathcal{L}$ is the linearized Navier–Stokes operator for the fluctuating state vector about the instantaneous $U(y,z,t)$ and $\boldsymbol{N}$ collectively denotes the nonlinear terms (which are quadratic with respect to fluctuating flow fields). Both $\mathcal{L}$ and $\boldsymbol{N}$ account for the kinematic divergence-free condition $\boldsymbol{\nabla} \cdot \boldsymbol{u}' = 0$. The corresponding equation of motion for $U(y,z,t)$ is obtained by averaging the Navier–Stokes equations in the streamwise direction.

Results

To investigate the role of exponential instabilities, we modify the operator $\mathcal{L}$ so that all the unstable eigenmodes are rendered neutral for all times. Then, we inquiry whether turbulence is sustained. The kinetic energy of the turbulent fluctuations of this "channel with suppressed exponential instabilities" is presented in Fig. 2(a). The result shows that, after transients, turbulence persists when $\mathcal{L}$ is replaced by its modally stable counterpart. Hence, turbulence is sustained, despite the absence of streak instabilities.

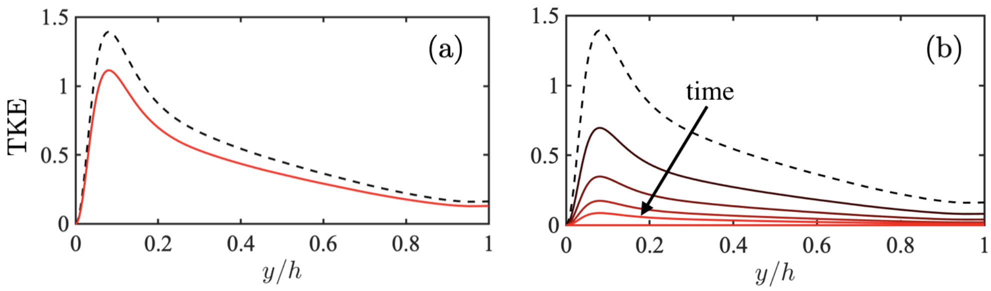

Fig. 2: Kinetic energy of the turbulent fluctuations for (a) channel with suppressed exponential instabilities and (b) same as (a) but with frozen-in-time base flow. Dashed line is for regular channel and colored lines for modified channels.

The effect of non-modal transient growth as a main source for energy injection into the fluctuating velocities is assessed by "freezing" the base flow $U(y,z,t_0)$ at the instant t_0. In order to steer clear of the effect of exponential instabilities, the numerical experiment is performed for the channel with suppressed exponential instabilities. Simulations are then continued for $t > t_0$. This procedure was repeated for 100 different t_0. The set-up disposes of energy transfers that are due to both modal and parametric instabilities, while maintaining the transient growth of perturbations. The results, shown in Fig. 2(b), suggest that turbulence is not exclusively supported by transient growth, at least when the magnitude of the perturbations corresponds to those typically encountered at the low Reynolds number used here.

Conclusions

By constraining the linear dynamics controlling the energy-injection from the base flow to the fluctuations, we have demonstrated that (i) the flow remains turbulent when the exponential instabilities are suppressed and (ii) transient growth alone is not sufficient to sustain wall turbulence. Hence, we conclude that (iii) transient growth, combined with a time-varying base flow, is able to sustain turbulence.

References

[1] J. Jiménez, *Phys. Fluids* **25**, 110814 (2013).

[2] W. C. Reynolds, A. K. M. F. Hussain, *J. Fluid Mech.* **54**, 263 (1972).

[3] F. Waleffe, *Phys. Fluids* **9**, 883 (1997).

[4] W. Schoppa, F. Hussain, *J. Fluid Mech.* **453**, 57 (2002).

[5] J. C. Del Álamo, J. Jiménez, *J. Fluid Mech.* **559**, 205 (2006).

[6] Y. Hwang, C. Cossu, *J. Fluid Mech.* **664**, 51 (2010).

[7] J. Kim, T. R. Bewley, *Annu. Rev. Fluid Mech.* **39**, 383 (2006).

[8] P. Schmid, D. Henningson, *Stability and Transition in Shear Flows*, Applied Mathematical Sciences (Springer New York, 2012).

[9] J. Kim, P. Moin, R. Moser, *J. Fluid Mech.* **177**, 133 (1987).

[10] J. Jiménez, P. Moin, *J. Fluid Mech.* **225**, 213 (1991).

*corresponding author: adrianld@stanford.edu

Increased drag of bodies settling in a linearly stratified fluid

J. Magnaudet[1]*, J. Zhang[2,1], M. J. Mercier[1]

[1]Institut de Mécanique des Fluides de Toulouse, Université de Toulouse, CNRS, INPT, UPS, Toulouse, France
[2]State Key Laboratory for Strength and Vibration of Mechanical Structures, School of Aerospace, Xian Jiaotong University, Shaanxi 710049, China

Introduction

Stratification due to salt or heat gradients greatly affects the distribution of living organisms and inert bodies settling in the ocean [1, 2], especially by enhancing their drag. Although detailed laboratory experiments [3, 4] and computational studies [5] captured this drag increase and attempted to model it, the physical mechanisms responsible for this signature of stratification effects are not entirely clear yet. To get new insight into these mechanisms, we introduce a rigorous decomposition of the governing equations which allows the various contributions to the drag to be properly disentangled whatever the relative magnitude of inertial, viscous, diffusive and buoyancy effects [6].

Decomposition scheme

Starting from the density and Navier-Stokes equations under the Boussinesq approximation, the velocity and pressure fields, $(\mathbf{u}, p)$, may be split as the sum of a contribution corresponding to the settling of the body within a homogeneous fluid, $(\mathbf{u}_w, p_w)$, and a buoyancy-induced contribution, $(\mathbf{u}_\rho, p_\rho)$. The momentum equation governing the latter involves two non-solenoidal contributions: one corresponds to the usual momentum flux provided by the advective term, while the other originates in the vertical variation of the density disturbance around the body. The pressure field p_ρ may then be expressed in the form $p_\rho = p_{\rho u} + p_{\rho\rho} + p_{\rho\omega}$, in which the first two contributions are governed by a Poisson problem with properly defined right-hand side and boundary conditions, and $p_{\rho\omega}$ obeys a Laplace equation and results from the buoyancy-induced vorticity $\boldsymbol{\omega}_\rho = \nabla\times\mathbf{u}_\rho$. It may then be shown that the total buoyancy-induced drag, F_ρ, can be written as $F_\rho = F_{\rho u} + F_{\rho\rho} + F_{\rho\omega}$, where each contribution directly results from the distribution of the corresponding pressure component at the body surface, supplemented in the case of $F_{\rho\omega}$ with the viscous contribution associated with the tangential component of $\boldsymbol{\omega}_\rho$. This exact decomposition offers a way to separate the buoyancy-induced drag into its physically meaningful components. This may easily be achieved through direct numerical simulation, once the fields $(\mathbf{u}, p)$ and $(\mathbf{u}_w, p_w)$ are computed in two separate runs, and then manipulated so as to solve the above two Poisson problems and eventually obtain each of the three contributions $F_{\rho u}$, $F_{\rho\rho}$ and $F_{\rho\omega}$.

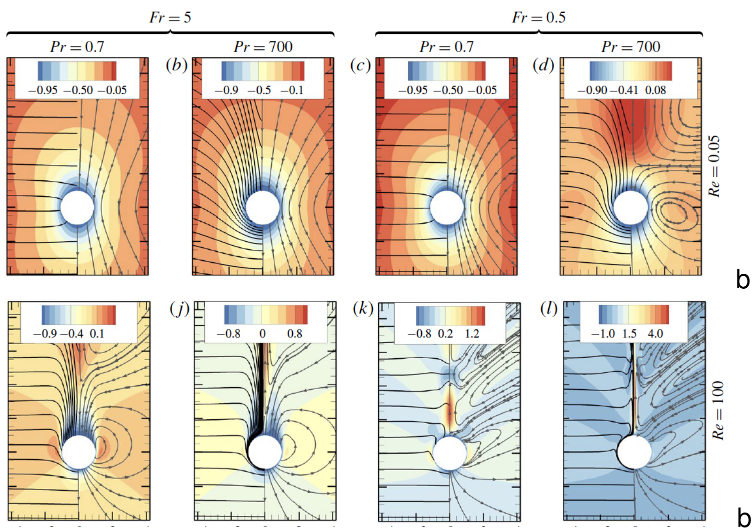

Fig. 1: Influence of the Reynolds, Froude and Prandtl numbers on the flow structure. Colours: isolevels of the vertical velocity; solid lines: isopycnals (left half), and streamlines (right half).

Results

We applied this decomposition procedure to numerical data obtained by simulating the flow past a settling sphere. Figure 1 shows several characteristics of the flow structure for selected values of the three control parameters, $Re = Wa/\nu$, $Pr = \nu/\kappa$ and $Fr = W/Na$, where W, a, ν and κ are the settling velocity, sphere radius, kinematic viscosity and molecular diffusivity, respectively, and $N = (-g\rho_0/\rho_{z0})^{1/2}$

stands for the Brünt-Väisälä frequency corresponding to the prescribed density gradient ρ_{z0}. This figure shows how the column of light fluid dragged by the body and the streamlines pattern vary as stratification effects increase for a given (Re, Pr). In particular it reveals that decreasing Fr and/or increasing Pr increases the curvature of the streamlines (figure 1$(b-c)$), which yields $\mathcal{O}(a)$-sized closed flow regions [7] in the presence of strong enough stratification (figure 1(d)). The size of these closed regions reduces when Re increases; for low Fr, they exhibit a V-shape due to the streamwise modulation of the vertical velocity field by the internal waves (figure 1$(k-l)$).
Figure 2 reveals how the drag enhancement varies with Re, Fr and Pr, and which of the above three contributions dominates in each regime. Decreasing Fr to $\mathcal{O}(1)$-values makes the drag increase dramatically whatever Re, especially for large Pr. It turns out that $F_{\rho\omega}$ dominates the drag enhancement in most regimes, especially when Pr is large. Hence, the changes in the vorticity field resulting from baroclinic effects play a pivotal role in the drag increase throughout the explored Re-range. Conversely, density variations at the body surface play a negligible role at low Re but their relative magnitude gradually increases with the Reynolds number.
Simulations also reveal how each of the buoyancy-induced contributions to the drag varies with the flow parameters (figure 3). To rationalize these variations, we analyze the different possible leading-order balances in the governing equations. We identify several distinct regimes which differ by the relative magnitude of length scales associated with stratification, viscosity and diffusivity, respectively. Making use of the spatial decay properties of the settling-induced disturbance $\mathbf{u}_w$ at low and large Re, we derive the exponents of the scaling laws followed by the buoyancy-induced drag contributions $F_{\rho\rho}$ and $F_{\rho\omega}$ in each of these regimes.

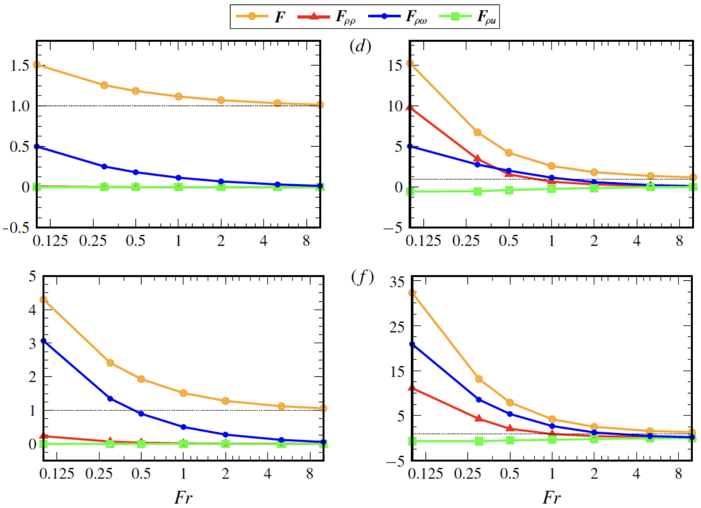

b

b

Fig. 2: Contributions to the drag force vs. the Froude number for $Re = 0.05$ (left) and $Re = 100$ (right) with $Pr = 0.7$ (top) and $Pr = 700$ (bottom). All contributions are normalized by the drag corresponding to homogeneous conditions (thin dotted line).

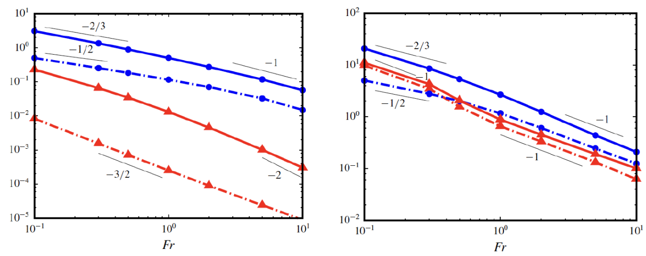

a

Fig. 3: Variations of normalized density-induced (red triangles) and vorticity-induced (blue circles) force components $F_{\rho\rho}$ and $F_{\rho\omega}$ in the low- ($Re = 0.05$, left) and high- ($Re = 100$, right) Reynolds-number regimes. Dash-dotted line: $Pr = 0:7$, solid line: $Pr = 700$.

References

[1] MacIntyre S et al. *Limnol. Oceanogr.* **40**:449468, 1995.
[2] D'Asaro E *J. Atmos. Ocean. Technol.* **20**:896–911, 2003.
[3] Srdic-Mitrovic AN et al. *J. Fluid Mech.* **381**:175–198, 1999.
[4] Yick KY et al. *J. Fluid Mech.* **632**:49–68, 2009.
[5] Torres CR et al. *J. Fluid Mech.* **417**:211–236, 2000.
[6] Zhang J et al. *J. Fluid Mech.* **875**:622–656, 2019.
[7] Ardekani AM & Stocker R *Phys. Rev. Lett.* **105**:084502, 2010.

*corresponding author: jmagnaud@imft.fr

Dissecting turbulent boundary layers: uncovering the organized flow in the log-region

Rahul Deshpande[1], Jason P. Monty[1], Ivan Marusic[1]*

[1]Department of Mechanical Engineering, University of Melbourne, Parkville, VIC 3010, Australia

Introduction

Large scale motions (LSMs) and superstructures (SS) constitute a majority portion of the turbulent kinetic energy in the log-region [1] of a zero pressure gradient turbulent boundary layer (ZPG TBL). While LSMs are known to be of the order of 2-3δ [1] in length (where δ is the TBL thickness), there remains disagreement in the literature with regards to the true streamwise extent of the SS [2]. Plausible reasons behind this inconsistency include the meandering nature of the SS [2] and/or SS simply being a consequence of spatial coherence of LSMs [1]. The present study investigates the mechanism associated with the latter, subsequently explaining the meandering and the inconsistencies in SS length. The adopted methodology leads to a better understanding of the organized flow in the log-region, culminating in the form of a 3-D conceptual sketch of the TBL.

Methodology and Results

The organized flow is brought out clearly by dissecting the full field into contributions from the *wall-attached* (WA; i.e. they physically extend to the wall) and *wall-detached* (WD) eddies via the spectral linear stochastic estimation (SLSE) technique [3]. Two ZPG TBL datasets are considered: (i) Re_τ $\approx$ 2,000 direct numerical simulation (DNS; $\mathcal{S}_1$) dataset of [4], and (ii) Re_τ $\approx$ 14,000 experimental dataset ($\mathcal{E}_1$) reported in [5], comprising multi-point hotwire measurements of the streamwise velocity fluctuations (u). Following the methodology in [3], the data are used to obtain 2-D instantaneous flow fields: u^+_{wa} (figure 1(c)) and u^+_{wd} (figure 1(d)), respectively consisting of contributions from the WA and WD eddies, at a wall-normal location (z^+) in the log-region. Similarly, $k^+_i\Phi^+_{wa}$ (figure 1(a)) and $k^+_i\Phi^+_{wd}$ (figure 1(b)) respectively represent the premultiplied 1-D u-spectra (at the same z^+) representing the per-scale WA and WD eddy contributions, where $i = x$ or y depending on the spectra being a function of the streamwise (λ_x) or spanwise (λ_x) wavelengths.

Some noteworthy observations can be made from u^+_{wa} and u^+_{wd}, underscoring the partition of the full field into these two sub-components. In general, WA eddies appear to be longer and wider compared to the WD eddies. Further, the meandering behavior of the SS is only seen in u^+_{wa}, suggesting SS are WA motions. This is substantiated by the Φ^+_{wa} plots in figure 1(a), where the 1-D streamwise and spanwise spectra respectively showcase δ-scaled peaks at $\lambda_x \sim 6\delta$ and $\lambda_y \sim 0.7\delta$, both of which are signatures of the SS [1, 2, 5]. The δ-scaling of the dominant λ_y is consistent with the quasi-periodic spanwise organization of the large scales in u^+_{wa}. Interestingly, no such large-scale periodicity is discernible in u^+_{wd}. On the contrary, Φ^+_{wd} plots reveal that the dominant WD motions follow z-scaling.

Attention is now directed to u^+_{wa} to understand SS. The apparent organized flow in u^+_{wa} is exploited to model it as a simplified synthetic field (u_s) with sinusoidal variation along y, as shown in figure 1(e). The fact that the dominant WA motions (SS) are arranged along y according to $(\lambda_y)_{dom} \sim 0.7\delta$, coupled with the knowledge of an individual SS having a nominal width of 0.35δ ($\sim \frac{(\lambda_y)_{dom}}{2}$) [1], suggests an end-to-end packing of alternatively arranged [2, 4, 5] $-u$ and $+u$ SS along y, which is adopted in u_s. The sinusoidal variation in u_s is extended up to $\sim$3δ along x, to be consistent with the length of LSMs (since LSMs concatenate to form SS). This 'stack' of LSMs (enclosed by a dashed line in figure 1(e)) is repeated along x, with a random offset along y, to more closely replicate u^+_{wa}. Next, u_s is used to demonstrate a procedure to bring out the organized flow pattern along x by utilizing the known periodicity along y. It involves cross-correlating the flow field along y, at every x, with a reference (say, $u_s(x$ = -6δ, $y))$ following:

$$\mathcal{R}_s(x,\Delta y) = \overline{u_s(x=-6\delta,y)u_s(x,y+\Delta y)}/\big(\sqrt{u_s^2(x=-6\delta)}\sqrt{u_s^2(x)}\big), \tag{1}$$

where the overbar denotes ensemble averaging. Figure 1(f) depicts the computed $\mathcal{R}_s$, with the periodicity along y inherited from u_s. Computing $\mathcal{R}_{wa}$ for u^+_{wa}, by replacing u_s with u^+_{wa} in equation 1, yields an output (figure 1(g)) qualitatively similar to figure 1(f). Two LSM stacks can be observed in figure 1(g), staggered by a certain offset along y, with each stack extending 2-3δ along x. It can be noted that $\mathcal{R}_{wa}$ drops at every x corresponding to the transition from one LSM stack to the other, suggesting the long contiguous $+u$/$-u$ structure to be simply a consequence of spatial coherence of LSMs. Present analysis thus suggests spanwise packing of the LSMs as the mechanism responsible for their concatenation (along x) leading to SS. The analysis also indicates that the staggered arrangement of these

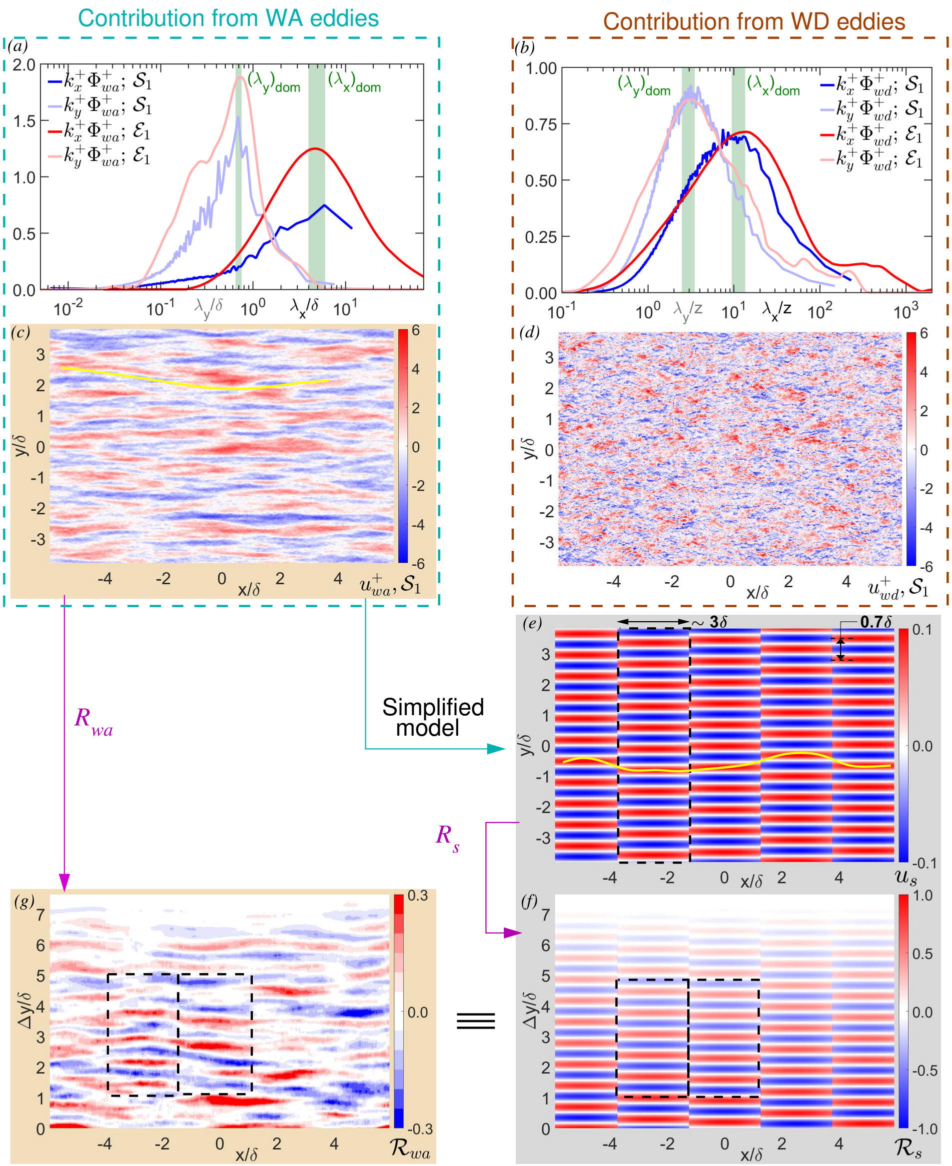

Fig. 1: Premultiplied 1-D energy spectra (a,b) and instantaneous u-fluctuations (c,d) representing contributions from WA (a,c) and WD (b,d) eddies at $z^+ \approx 2.6\sqrt{Re_\tau}$. (e) WA LSMs in $u^+_{wa}(z;x,y)$ modeled using a simplified synthetic field given by $u_s(x,y)$. (f) $\mathcal{R}_s$ and (g) $\mathcal{R}_{wa}$ computed respectively for u_s (e) and u^+_{wa} (c) following equation 1. Boxes with dashed line in (e-g) indicate the LSM 'stack' referred to in the text, while the solid yellow line in (c,e) highlights the apparent meandering pattern.

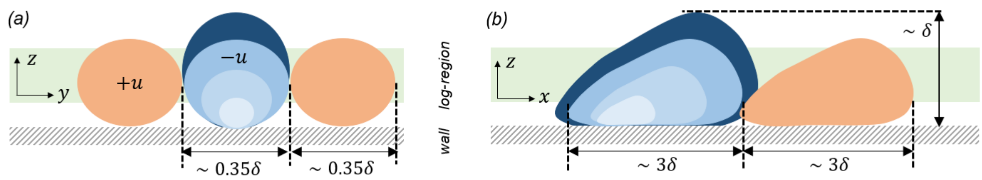

Fig. 2: An idealized schematic depicting the average growth and organization of the large WA motions in the log-region (in green) of a ZPG TBL. Growth in the (a) y-z and (b) x-z plane continues self-similarly (light-shaded) until the eddies fill the layer spanwise [1].

LSM stacks, along x, leads to: (i) an apparent meandering appearance of a long $+u/-u$ (figure 1(c,e)), and (ii) a dominant peak at $\lambda_x \sim 6\delta$ ($\sim$ twice the LSM length) in $k_x^+\Phi_{wa}^+$. These statistical observations associated with the large WA motions are summarized in the form of an idealized conceptual sketch (figure 2) depicting their organization in the log-region of a TBL. Discussion on the organization of the WD eddies will be presented in the talk and the full paper.

References

[1] Tomkins CD & Adrian RJ. *J Fluid Mech* **545**:141-162, 2005.
[2] Hutchins N & Marusic I. *J Fluid Mech* **579**:1-28, 2007.
[3] Baars WJ et al. *Phys Rev Fluids* **1**(5):054406, 2016.
[4] Sillero JA et al. *Phys Fluids* **26**(10):105109, 2014.
[5] Deshpande R et al. *J Fluid Mech (under review)* 2020.

*corresponding author: imarusic@unimelb.edu.au

Goldilocks mixing in shear-induced ocean turbulence

A. Mashayek[1]*

[1]Imperial College London

Abstract

Diapycnal turbulent mixing in the ocean interior plays a leading role in supporting the ocean overturning circulation and its associated transports of heat, carbon and biological nutrients. While the importance of diapycnal mixing in the deep ocean has been recognized since the seminal work of Walter Munk [1], a quantification of its impact on the MOC and tracer transports remains elusive [2]. Mixing in the deep ocean is primarily the result of breaking internal waves or boundary layer processes occurring at scales from millimeters to tens of meters (Figure 1-top). Such mixing is typically quantified in terms of a turbulent diapycnal diffusivity, κ. Munk first estimated that an average turbulent diapycnal diffusivity of $\kappa \sim \mathcal{O}(10^{-4})$ m^{2}s^{-1} is required to allow the observed $\mathcal{O}(10)$ Sv (1 Sv = 10^{6}m^{3}s^{-1}) flow across the deep ocean density surfaces. Values of κ an order of magnitude larger or smaller would imply an MOC much larger or smaller than observed.

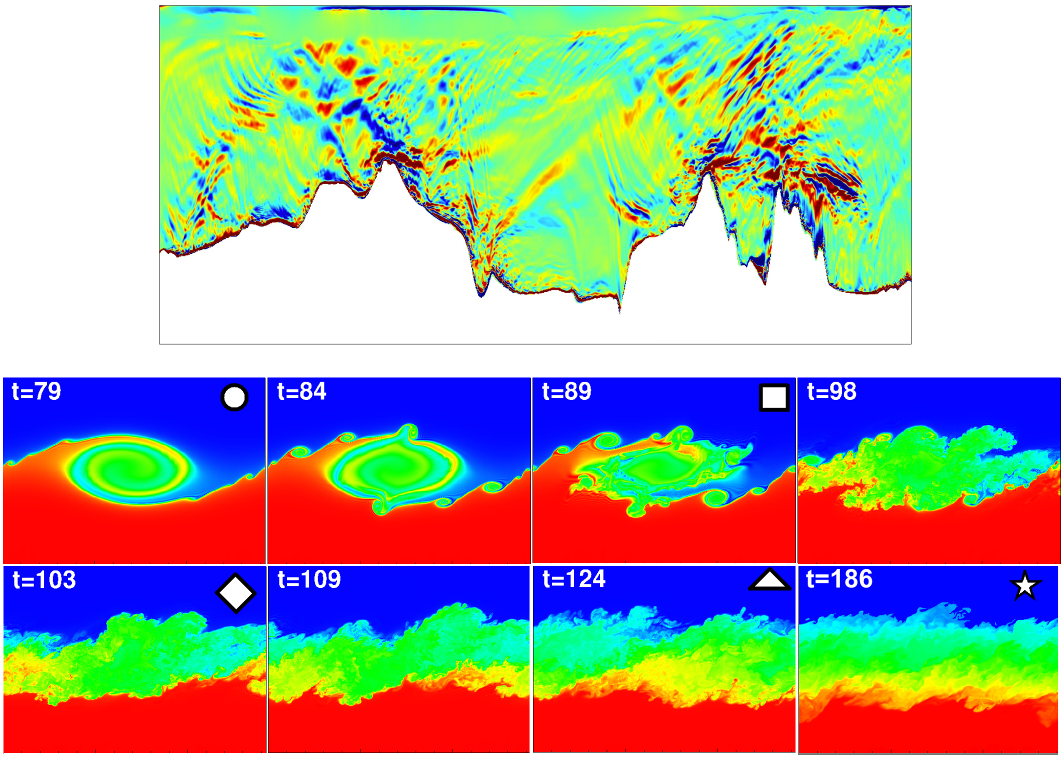

Fig. 1: Top: internal waves induced by flow over topography in the Drake Passage (from Mashayek *et al.* (2017) [5]). Bottom: turbulent lifecycle of an individual wave breaking event leading to mixing of dense water (red) with the overlying lighter water (blue); from Mashayek *et al.* (2017) [4].

As of today, it is still an open question whether diapycnal mixing in the deep ocean is sufficiently large to play a dominant role in closure of the deep branch of the ocean circulation. The oceanographic and climate modeling communities have so far attributed the large uncertainties to purely oceanographic issues such as sampling and measurement errors, all but ignoring the literature on density stratified turbulence. As one evidence to this neglect, a flux coefficient of 0.2 (defined as $\Gamma = \eta/(1-\eta)$, where η is the efficiency of mixing) has been consistently used to interpret mixing rates from observations and to parametrize such mixing in ocean models. This is despite the significant evidence accumulated in the Journal of Fluid Mechanics alone to the variability of η with parameters such as the Reynolds, Richardson and Prandtl numbers.

The reason behind the apparent topical disconnect between the Fluid Mechanics literature and the ocean/climate communities is two folds: first, there is a lack of consistent representation of mixing in terms of 'measurable' parameters in the Fluid Mechanics literature, and, second, there has been little efforts towards connecting the small scale mixing to the broader mixing-induced ocean circulation. It has only recently been revealed that the uncertainties due to lack of full understanding of the physics of small scale turbulence introduce a leading order obstacle in way of accurate quantification of role of mixing in the global circulation [4]. This revelation has led to a paradigm shift in our understanding of ocean circulation, as summarized by Powell (2006)[6].

In this work we present a simple analytical model for efficiency of turbulent mixing in terms of measurable quantities by relying on (I) dimensional consistency, (II) recent theoretical developments in physical understanding of wave breaking events (e.g. see Figure 1-bottom), and (III) a comprehensive dataset of mixing due to stratified turbulent patches in Direct Numerical Simulations as well as in ocean observations. We then employ the model and predict, based on simple theoretical grounds, that the maximum diapycnal turbulent flux in the deep ocean (where turbulence is bottom generated) occurs at a diapycnal diffusivity of $\kappa \sim 3 \times 10^{-4}\ m^2 s^{-1}$ and that while η can be variable, it is $\sim$ 0.2 where the maximum upwelling of deep waters occurs.

The significance of our result is two folds. First, it shows that purely based on physics of density stratified turbulence we can predict the rate of optimal upwelling of abyssal ocean waters to be consistent with the Munk's canonical value based on bulk tracer budgets (noting that his finding has been verified in various follow up studies since). Second, the maximum upwelling of abyssal waters, on basin-wide scales, occurs where there is the right balance between the ambient stratification and the energy available to turbulence via the background shearing flow. The very same balance is required in breaking of individual waves to facilitate an optimal mixing [3]: too strong a stratification suppresses mixing, too small stratification implies not much to mix, and the 'right' amount of stratification for a given shear gives birth to a zoo of hydrodynamic instabilities that facilitate efficient mixing. This is what we refer to as the **'Goldilocks Mixing'** and our study suggests that it is a micro-physical property (relevant on sub-meter scales) that extends to basin-wide mixing (scales of thousands of kilometers) and thereby exerts a control over the climate system.

References

[1] Munk(1966) Abyssal recipes. *Deep-Sea Research*, **113**, 207–230.

[2] Peltier & Caulfield (2003) Mixing efficiency in stratified shear flows *Annual review of fluid mechanics*, **35.1**, 135–167.

[3] Mashayek *et al.*(2017) Role of overturns in optimal mixing in stratified mixing layers *Journal of Fluid Mechanics*, **826**, 522–552.

[4] Mashayek *et al.*(2017a) Efficiency of turbulent mixing in the abyssal ocean circulation. *Geophysical Research Letters*, **44.12**, 6296–6306.

[5] Mashayek *et al.*(2017b) Topographic enhancement of vertical turbulent mixing in the Southern Ocean. *Nature communications*, **8**, 14197.

[6] Powell (2016) Role of chaos in deep ocean turned upside down. *Nature News*, 26 February 2016.

*corresponding author: mashayek@imperial.ac.uk

Interactions between scales in wall turbulence: phase relationships, amplitude modulation and the importance of critical layers

I. Jacobi[1], D. Chung[2], S. Duvvuri[3], B. J. McKeon[4*]

[1]Faculty of Aerospace Engineering, Technion Israel Institute of Technology, Haifa 32000 Israel
[2]Department of Mechanical Engineering, University of Melbourne, Victoria 3010, Australia
[3]Department of Aerospace Engineering, Indian Institute of Science, Bengaluru 560 012, India
[4]Graduate Aerospace Laboratories, California Institute of Technology, Pasadena, CA 91125, USA

Introduction

Large-scale motion, that is, motion comprising scales larger than δ, where δ is the boundary-layer height, channel half height or pipe radius, plays an increasingly important role in wall turbulence as the Reynolds number increases, e.g. [1]. In addition to contributing to the total energy, evidenced by the increasingly dominant very large-scale peak at wavelengths of order 10δ in the premultiplied velocity spectrum, the very large-scale motion also appears to modulate and organize the underlying small-scale motion. An aspect of this phenomenon is measured by the amplitude modulation statistic $\mathcal{R}$ [2], a one-point statistic that measures the relative placement of small-scale activity to the large scale motion. Near the wall, intense small-scale stresses accompany a large-scale higher momentum region and vice versa, corresponding to $\mathcal{R} > 0$, but above a certain zero-crossing height, this relationship is reversed, $\mathcal{R} < 0$. Interestingly, this height also tracks the wall-normal location of the very large-scale spectral energy peak [2]. Cross-spectral analysis [3] reveals that the amplitude modulation coefficient is dominated by the influence of the very large scale motions (VLSMs), with wall-normal variation of this phase relationship that is consistent with conditionally-averaged large eddy simulation [4] and experimental results [5], namely a $\pi/2$ spatial lag of the large-scale streamwise velocity relative to the envelope of small scale stress with the same frequency content as the very large-scale spectral energy peak, as shown in Fig. 1(a-b).

Framework for scale interaction

Extending the transfer function concepts underlying resolvent analysis [6], we present an analytical transfer function framework to predict the interactions between scales in wall turbulence that is capable of linking all three components of large- and small-scale velocity signals.

We decompose the flow field, described by the velocity u_i and kinematic pressure p, into the mean $\overline{(\;)}$, isolated single scale $\widetilde{(\;)}$ and remaining turbulent $(\;)'$ components:

$$u_i = \overline{u}_i + \widetilde{u}_i + u_i', \quad p = \overline{p} + \widetilde{p} + p'. \tag{1}$$

Here the isolated scale consists of a single turbulent scale and all other remaining turbulent activity is lumped into u_i'. Such a decomposition is most easily conceptualized by invoking a narrow bandpass spectral filter around the wavenumber $\mathbf{k_f}$. Thus, $\widetilde{u}_i$ comprises modes with wavenumber $\mathbf{k_f}$ while u_i' comprises modes with wavenumbers other than $\mathbf{k_f}$. In what follows, we will define $\mathbf{k_f} = (k_x, k_z, \omega)$, where k_x and k_z are real wavenumbers in the two spatial (wall-parallel) directions and ω is the real angular frequency, effectively a single scale in a triple Fourier decomposition.

Applying the narrow bandpass filter at $\mathbf{k_f}$, we obtain the dynamical equation for $\widetilde{r}_{ij} = \widetilde{u_i'u_j'}$, the filtered fluctuation of the background mean stress, $\overline{r}_{ij} = \overline{u_i'u_j'}$, at the isolated scale

$$\frac{\partial \widetilde{r}_{ij}}{\partial t} + \overline{u}_k \frac{\partial \widetilde{r}_{ij}}{\partial x_k} + \widetilde{u}_k \frac{\partial \overline{r}_{ij}}{\partial x_k} + \widetilde{r}_{jk} \frac{\partial \overline{u}_i}{\partial x_k} + \widetilde{r}_{ik} \frac{\partial \overline{u}_j}{\partial x_k} + \overline{r}_{jk} \frac{\partial \widetilde{u}_i}{\partial x_k} + \overline{r}_{ik} \frac{\partial \widetilde{u}_j}{\partial x_k} - \nu \frac{\partial^2 \widetilde{r}_{ij}}{\partial x_k^2} = \widetilde{g}_{ij}, \tag{2}$$

where ν is the kinematic viscosity and

$$\widetilde{g}_{ij} \quad = \quad -\frac{\partial}{\partial x_k} \widetilde{u_i'u_j'u_k'} - \widetilde{u_j' \frac{\partial p'}{\partial x_i}} - \widetilde{u_i' \frac{\partial p'}{\partial x_j}} - 2\nu \widetilde{\frac{\partial u_i'}{\partial x_k} \frac{\partial u_j'}{\partial x_k}}.$$

In the spirit of resolvent analysis, we model the nonlinear and unclosed terms $\widetilde{g}_{ij}$ as external forcing, considering first a simple version of the scale interaction equations with $\widetilde{g}_{ij} = 0$ with a view to demonstrating the origin of the amplitude modulation of the small scales by the large scales. Specialising to wall turbulence and writing velocity and stress fluctuations at the scale of interest as

$$\{\widetilde{u}_i, \widetilde{r}_{ij}\}(x, y, z, t) = \{\widetilde{U}_i, \widetilde{R}_{ij}\}(y; k_x, k_z, \omega) \mathrm{e}^{\mathrm{i}(k_x x + k_z z - \omega t)} + \mathrm{c.c}, \tag{3}$$

for each (k_x, k_z, ω), Eq. 2 may be written as

$$A\mathbf{R} + B\mathbf{U} = 0, \tag{4}$$

where A and B represent the operators acting on the stress and the large-scale velocity, respectively. A may be simply inverted upon discretization of the wall-normal coordinate [6], or upon assuming an analytical model for the form of the stress, with both developments leading to a transfer function relationship,

$$\mathbf{R} = -A^{-1}B\mathbf{U}. \tag{5}$$

Here we exploit the semi-analytical form for leading velocity resolvent modes from [7] to model the form of the large-scale velocity and the stress, and focus on streamwise velocity interactions and the modulating influence of large-scale motion in the log region on the underlying small-scale motion. By performing a scaling analysis of Eq. 5 in the vicinity of the critical layer, where $\overline{u}(y) = \omega/k_x$, we show that an inviscid assumption requires the streamwise stress, $\widetilde{R}_{xx}$, to lag (in a spatial sense) the large scale streamwise velocity, $\widetilde{U}$. For the viscous case this phase relationship is reversed such that the stress leads the large scale by $\pi/2$ at the critical layer. The resulting spatial organization (phase relationship) between the stress and the large scale motion, which is in agreement with the experimental observations, is sketched in Fig. 1(c), after [4].

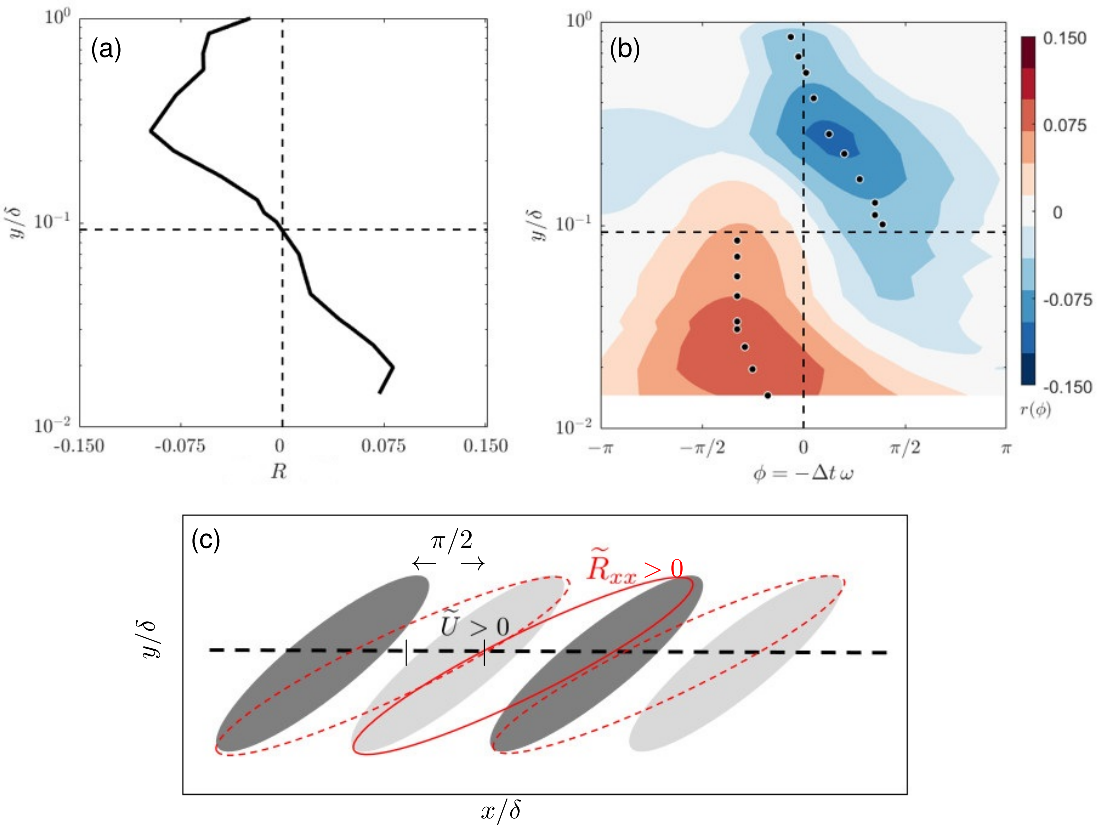

Fig. 1: (a) Correlation coefficient, R, between large- and small-scale stress introduced by [2] for a zero pressure gradient turbulent boundary layer with $Re_\tau \approx 910$ as in [3], who observed that R is dominated by contributions from the frequency of the large-scale peak, ω. (b) Temporal cross-correlation function, $r(\phi)$, between the large scale and the small-scale stress at ω. Dots indicate the temporal phase leads/lags for peak correlation, ϕ_{max}, such that while $R = r(0)$ by definition, it can also be related to the phase shift between signals by $R = cos(\phi_{max})$ [4]; the zero of R near the large-scale critical layer (indicated by dashed horizontal lines) corresponds to $\phi_{max} = -\pi/2$. (c) Sketch of the spatial phase relation between envelopes of large- and small-scales for a viscous flow, indicating that the positive small scale signal, $\widetilde{R}_{xx}$, leads the large, $\widetilde{U}$ (after [4]).

References

[1] N. Hutchins and I. Marusic. *J. Fluid Mech.*, 579:1–28, 2007.
[2] R. Mathis, N. Hutchins, and I. Marusic. *J. Fluid Mech.*, 628:311–337, 2009.
[3] I. Jacobi and B. J. McKeon. *Expts. Fluids*, 54(1481), 2013.
[4] D. Chung and B. J. McKeon. *J. Fluid Mech.*, 661:341–364, 2010.
[5] N. Hutchins, J. P. Monty, B. Ganapathisubramani, H. C. H. Ng, and I. Marusic. *J. Fluid Mech.*, 673:255–285, 2011.
[6] B. J. McKeon and A. S. Sharma. *J. Fluid Mech.*, 658:336–382, 2010.
[7] S. T. M. Dawson and B. J. McKeon. *J. Fluid Mech.*, 877:682–716, 2019.

*corresponding author: mckeon@caltech.edu

Two-point subfilter stress-strain rate correlations and non-local fractional eddy viscosity closures in turbulent flows

P. Clark Di Leoni[1], T. Zaki[1], G. Karniadakis[2] & C. Meneveau[1]*

[1]Johns Hopkins University, 3400 N. Charles Street, Baltimore, MD 21218, USA
[2]Brown University, 182 George Street, Providence, RI 02912, USA

Introduction

Scale interactions in turbulent flows can be studied using the filtering approach, in which a spatial filter separates large from small scales [1, 2]. Such studies are of particular interest in the context of Large Eddy Simulations (LES) [3, 4], where some but not all scales are solved for explicitly. The effects of scales smaller than the filter size are modeled by modifying the stress tensor in the equations. Most existing sub-filter (or subgrid-scale) models used in practical LES today rely on the concept of local eddy-viscosity, setting the sub-filter scale stress tensor proportional to the strain rate tensor of the resolved (filtered) motions at the same spatial position and time. While various models differ in how the proportionality factor, the eddy-viscosity, is specified, the approach is in essence a spatially and temporally *local* closure model. In recent years, several approaches to include non-local effects for turbulent stresses have been proposed [5, 6, 7, 8, 9]. In this work, we explore the potential benefits of non-local eddy viscosity modeling by focusing on its effects on two-point correlation functions of filtered velocities. Consideration of the Karman-Howarth equation for filtered velocity fields enables us to show that the evolution of filtered-velocity correlation functions is directly affected by the subfilter stress-strain rate correlation structure. Statistical analysis of these correlation functions then enables us to draw conclusions regarding the importance of non-locality in subgrid modeling for LES.

Two-point statistics in turbulence and non-local fractional eddy viscosity

By analyzing the Karman-Howarth equation for filtered velocity fields in turbulent flows, we show that the two-point correlation between filtered strain-rate and subfilter stress tensors plays a central role in the evolution of filtered-velocity correlation function $\langle \tilde{u}_i(\mathbf{x})\tilde{u}_i(\mathbf{x}+\mathbf{r})\rangle$. Specifically, one can show that the subfilter scale stress tensor τ_{ki} and the filtered strain-rate tensor $\tilde{S}_{ki}$ from LES should display the correct correlation function, i.e.

$$\langle \tau_{ki}^{\mathrm{LES}}(\mathbf{x})\tilde{S}_{ki}^{\mathrm{LES}}(\mathbf{x}+\mathbf{r})\rangle = \langle \tau_{ki}(\mathbf{x})\tilde{S}_{ki}(\mathbf{x}+\mathbf{r})\rangle, \qquad (1)$$

as a condition [10] to reproduce the correct second and third-order two-point moments of the resolved velocity fields. Evaluated at $r = 0$ it reduces to the usual condition that a subgrid-scale model should reproduce the correct rate of total kinetic energy extraction (SGS dissipation) from the large scales [1]. The condition also shows that if the stress tensor in LES is set proportional to the strain-rate tensor at a displaced location $\mathbf{x}+\mathbf{r}$, physically more realistic correlations may be generated through nonlocal eddy-viscosity models.

We argue that fractional calculus provides mathematically rich options to express non-locality without the a-priori introduction of additional length-scales in the mathematical operator, at least in principle. (When evaluating fractional derivatives, often an upper cutoff scale must still be introduced in practice, and subsequent physical models do often include an effective length-scale - but the fractional derivative itself as a mathematical operation is scale-free).

We generalize the notion of a Caputo fractional derivative to multi-dimensional calculus by introducing the ‘volume kernel’ Caputo gradient operator. Based on this definition, we introduce a fractional velocity gradient tensor as well as the fractional filtered strain-rate tensor. A fractional eddy-viscosity model may then be formulated. The model is parameterized by the fractional gradient order $0 < \alpha < 1$; the classical gradient local model (e.g. Smagorinsky) corresponding to $\alpha = 1$. An outer cutoff scale R is also required.

Results

Using spatially filtered data from direct numerical simulations of isotropic and channel flow turbulence we show that local eddy viscosity models fail to exhibit the long tails observed in the real subfilter stress-strain rate correlation functions (comparing the exact – dashed lines – to the $\alpha = 1$ case in Figs. 1). For example, in Fig. 1(a) we observe that at $r = 2\Delta$, the correlation modeled with local eddy viscosity ($\alpha = 1$) under-predicts the correlation by a significant margin.

Stronger non-local correlations may be achieved by defining the eddy-viscosity model based on fractional gradients of order $0 < \alpha < 1$ rather than the classical gradient corresponding to $\alpha = 1$. Analysis

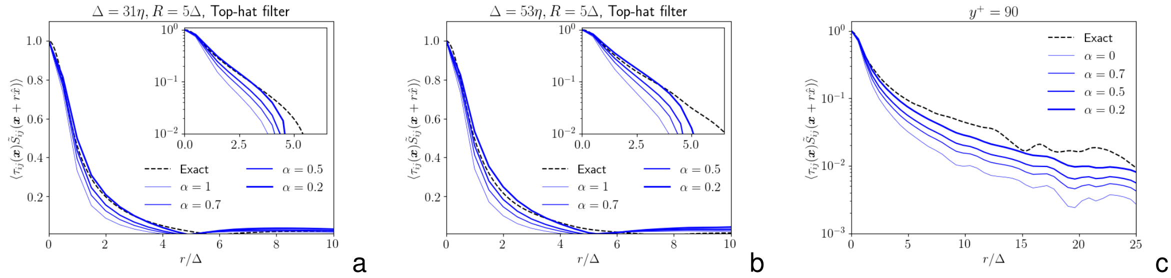

Fig. 1: Two-point subfilter stress strain-rate correlation functions normalized by their value at $r = 0$. Panels (a) and (b) show the results for isotropic turbulence at $Re_\lambda = 433$ using data from JHTDB (turbulence.pha.jhu.edu), using a top-hat filter at scale $\Delta = 31\eta$ (a) and $\Delta = 53\eta$ (b), where η is the Kolmogorov scale. Inserts show the same curves but in logarithmic scale. Panel (c) shows the results with $\mathbf{r}$ in the streamwise direction of a channel flow at $Re_\tau = 1,000$ (data also from JHTDB), at $y^+ = 90$ using a filtering scale of $\Delta^+ = 40$.

of such correlation functions are presented for various orders of the fractional gradient operators. It is found that in most cases fractional derivative order $\alpha \sim 0.2$ yields the best results. Results show a weak dependence on outer cutoff scale R but the dependence is expected to vanish for large $R/\Delta >> 1$.

Conclusions

The findings of relatively long correlations between subfilter stresses and the strain-rate tensor suggest that non-local eddy viscosity modeling can provide more accurate predictions of velocity correlation functions, as a concrete statistical measure of success. Specifically, models based on fractional gradients for orders $\alpha \sim 0.2$ yield better agreement with measured stress-strain rate correlation functions in DNS of isotropic and channel flow turbulence than values closer to unity, the value for local eddy viscosity modeling.

Acknowledgments

This research is supported by DARPA-AIRA, grant HR00111990025.

References

[1] Leonard A. Energy cascade in large-eddy simulations of turbulent fluid flows. *Adv. Geophys.*, 18:237, 1974.

[2] Pope SB. *Turbulent Flows*. Cambridge University Press, 2000.

[3] Sagaut P. *Large Eddy Simulation for Incompressible Flows (3rd Ed.)*. Springer, 2006.

[4] Meneveau C. Turbulence: Subgrid-scale modeling. *Scholarpedia*, 5:9489, 2010.

[5] Dekker H. et al. Boundary-layer turbulence as a kangaroo process. *Physical Review E*, 52(3):2549, 1995.

[6] Hamba F. Nonlocal analysis of the reynolds stress in turbulent shear flow. *Physics of Fluids*, 17(11):115102, 2005.

[7] Mani A & Park D. Macroscopic forcing method: a tool for turbulence modeling and analysis of closures. *arXiv preprint arXiv:1905.08342*, 2019.

[8] Mehta P., Pang G., Song F. & Karniadakis GE. Discovering a universal variable-order fractional model for turbulent couette flow using a physics-informed neural network. *Fractional Calculus and Applied Analysis*, 22(6):1675–1688, 2019.

[9] Samiee M, Akhavan-Safaei A &. Zayernouri M. A fractional subgrid-scale model for turbulent flows: Theoretical formulation and a priori study. *arXiv preprint arXiv:1909.09943*, 2019.

[10] Meneveau C. Statistics of turbulence subgrid-scale stresses: Necessary conditions and experimental tests. *Phys. Fluids A*, 6:815, 1994.

*corresponding author: meneveau@jhu.edu

Hierarchical structures and scaling in steady Rayleigh–Bénard convection

S. Motoki[1]*, G. Kawahara[1], M. Shimizu[1]

[1]Graduate School of Engineering Science, Osaka University
1-3 Machikaneyama, Toyonaka, Osaka 560-8531, Japan

Introduction

Rayleigh–Bénard convection is the buoyancy-driven convection between the horizontal plates heated from below and cooled from above, and it is one of the most canonical flows widely observed in engineering applications and nature. The effect of the buoyancy on the flow is characterised by the Rayleigh number Ra, the dimensionless temperature difference between two plates. When Ra exceeds a certain critical value, a thermal conductive state becomes unstable to infinitesimal perturbations, and two-dimensional steady convection rolls appear. At higher Ra, the flow becomes time-periodic, and subsequently exhibits chaotic or turbulent states. For the two-dimensional steady solutions, recently, the scaling of the Nusselt number Nu with Ra as $Nu \approx 0.115Ra^{0.31}$ has been found [2]. The scaling is quite similar to the three-dimensional turbulent data fit $Nu \approx 0.105Ra^{0.312}$ [1]. In the work, optimal two-dimensional steady solutions have been obtained so as to maximize Nu by changing the horizontal period of the solutions. The scaling $Nu \sim Ra^{0.31}$ is achieved by a family of two-dimensional steady solutions with the horizontal period which decreases with increasing Ra. Although the result suggests that quite simple coherent structures can capture the essence of the turbulent convection, it also implies that any single two-dimensional steady solution with the fixed horizontal period (fixed maximal wavelength) cannot do it.

Three-dimensional steady solutions in the Rayleigh–Bénard convection

Recently, variational problems for the Rayleigh–Bénard convection to find a divergence-free velocity field optimising heat transfer have been discussed [3]. Authors [4, 5] have found three-dimensional steady velocity fields as optimal states which maximise heat transfer between two parallel plates of a constant temperature difference under the constraint of fixed total enstrophy. For the large total enstrophy, the optimal states consist of convection with hierarchical self-similar vortical structures, and exhibit the scaling which corresponds to the scaling $Nu \sim Ra^{1/2}$, referred to as the 'ultimate' scaling in Rayleigh–Bénard problem. Although the found optimal flow fields require external body force which is different from the buoyant force, we have demonstrated that by using homotopy from the body force to the buoyancy the optimal state can be continuously connected to a steady solution to the full Boussinesq equations. The red line in figure 1(*a*) shows Nu as a function of Ra for one of the connected solutions, and it exhibits the scaling $Nu \sim Ra^{0.31}$ at $Ra \gtrsim 10^5$, corresponding to that observed in large-Rayleigh number turbulent convection (black) and that achieved by a family of two-dimensional steady solutions with an optimal horizontal period (blue). The found steady solution exhibits three-dimensional structures as shown in figure 1(*b*), and we can see thermal plumes and vortices, similar to that observed in a turbulent state (figure 1*c*).

Hierarchical structures in three-dimensional steady solution

To examine a hierarchy in the three-dimensional steady solution, we consider coarse graining the velocity field. The coarse-grained velocity field has been obtained by the Gaussian low-pass filter [6, 7]. Figure 2(*a*-*f*) shows hierarchical vortical structures which are found out in the three-dimensional steady solution at $Ra = 2.6 \times 10^7$. Non-filtered velocity and temperature fields are shown in figure 2(*a*), and isosurfaces of the second invariant of the velocity gradient tensor, Q, of the filtered velocity field with the filter width $\sigma = H, L/2, L/4, L/8$ and $L/16$ are respectively displayed in figure 2(*b*-*f*) (H and L are the distance between the walls and horizontal period, respectively). The blue objects in figure 2(*b*) are largest-scale structures corresponding to the large-scale convection cells, whereas the red objects in figure 2(*f*) are smallest-scale vortical structures with the size of $\sigma/2 = L/32 \approx 2\delta_\theta$ ($\delta_\theta = H/(2Nu)$ is the thermal boundary layer thickness), which coincide with the vortices observed in the non-filtered velocity field (figure 2*a*). The light blue, green and light red objects in figures 2(*c*-*e*) respectively show intermediate-scale vortical structures with the eight, four and two times the size of the smallest-scale vortices, and they suggest that the bulk flow is composed of multiscale coherent structures. Figure 2(*g*) shows the energy spectral function $E(k)$ at the center of the fluid layer (k is the magnitude of the two-dimensional wavenumber vector in the mid-plane). In the range $2\pi/(L/4) \lesssim k\eta \lesssim 2\pi/(L/16)$, corresponding to the intermediate-scale range, we can find that the energy spectra exhibit the Kolmogorov's $-5/3$ power law, $E = C_K\varepsilon^{2/3}k^{-5/3}$, with the constant $C_K \approx 1.5$ which is comparable with the Kolmogorov constant in the inertial subrange of high-Reynolds-number turbulence [8].

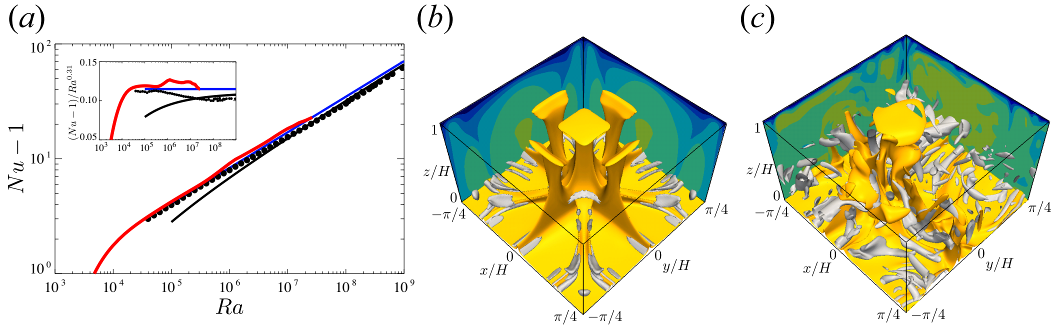

Fig. 1: (*a*) Nu as a function of Ra. The red line and black symbolds respectively represent the three-dimensional steady solution and turbulent states, obtained in the horizontally-square periodic domain of $L = L_x = L_y = 0.5\pi H$ for the Prandtl number $Pr = 1$. The blue and black lines indicate the scaling $Nu - 1 = 0.115 Ra^{0.31}$ [2] achieved by a family of two-dimensional steady solutions and the turbulent data fit $Nu = 0.105 Ra^{0.312}$ [1], respectively. (*b,c*) Flow and thermal structures in (*b*) the three-dimensional steady solution and (*c*) the turbulent state at $Ra = 10^7$. The yellow and grey objects respectively represent the isosurfaces of the temperature and the positive second invariant of the velocity gradient tensor, Q (note that, for Q only those in the lower half of the domain are shown).

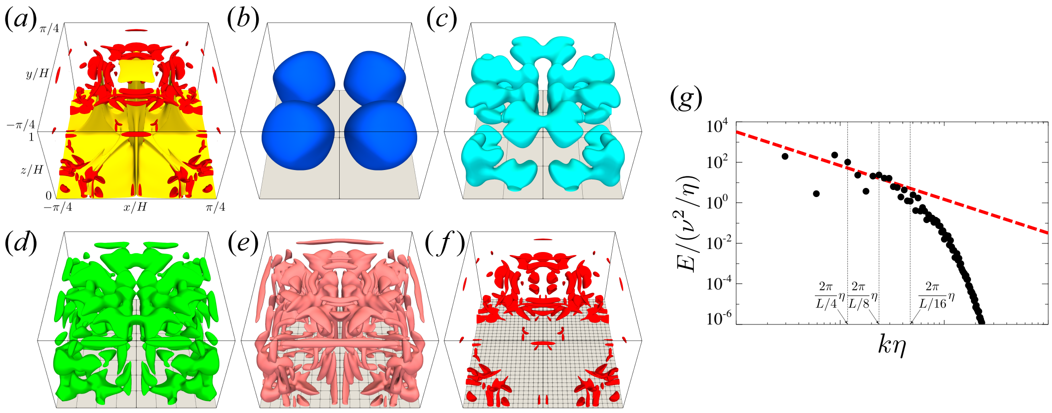

Fig. 2: (*a-f*) Hierarchical vortical structures in the three-dimensional steady solution at $Ra = 2.6 \times 10^7$ for $Pr = 1$, visualised by the coarse graining with the Gaussian low-pass filter. (*a*) Non-filtered velocity and temperature fields. The red and yellow objects show the isosurfaces of the positive Q, and the temperature, respectively. (*b-f*) The vortical structures are visualised by the isosurfaces of Q of the filtered velocity fields with the filter width $\sigma = H$ (blue), $L/4$ (light blue), $L/8$ (green), $L/16$ (light red), $L/32$ (red). (*g*) Energy spectra $E(k)$ at the center of the fluid layer in the steady solution at $Ra = 2.6 \times 10^7$ for $Pr = 1$. The lateral and longitudinal axes are normalized by the Kolmogorov micro-scale length η and the energy dissipation rate ε. The red dashed line indicates $E = 1.5\varepsilon^{2/3}k^{-5/3}$.

References

[1] X. He *et al. Phys. Rev. Lett.* **108** (024502), 2012.
[2] D. Sondak and L. M. Smith and F. Waleffe *J. Fluid Mech.* **784**:565-595, 2015.
[3] P. Hassanzadeh and G. P. Chini and C. R. Doering *J. Fluid Mech.* **751**:627-662, 2014.
[4] S. Motoki and G. Kawahara and M. Shimizu *J. Fluid Mech.* **835**:1157-1198, 2018.
[5] S. Motoki and G. Kawahara and M. Shimizu *J. Fluid Mech.* **851** (R4), 2018.
[6] A. Lozano-Durán and M. Holzner and J. Jiménez *J. Fluid Mech.* **803**:356-394, 2016.
[7] Y. Motoori and S. Goto *J. Fluid Mech.* **865**:1085-1109, 2019.
[8] K. R. Sreenivasan *Phys. Fluids* **7** (2778), 1995.

*corresponding author: motoki@me.es.osaka-u.ac.jp

A non-local model that incorporates dilatancy in slow granular flow
Fluid mechanics in the spirit of G. K. Batchelor

P. V. Dsouza, S. S. Kolluri, P. R. Nott*

Department of Chemical Engineering, Indian Institute of Science, Bangalore 560012, India

Introduction

The development of a constitutive relation for the stress for flowing granular materials is of considerable importance, due to their widespread occurrence in industrial processes and natural phenomena. In the regime of slow flow, where grain inertia is unimportant and contacts are abiding, classical plasticity theories [1, 2, 3] capture some important observed features, such as rate-independence of the stress. However, these theories suffer from kinematic indeterminacy in a broad class flows: if the deformation rate $\boldsymbol{D} \equiv \frac{1}{2}[\boldsymbol{\nabla u} + (\boldsymbol{\nabla u})^{\mathrm{T}}]$ (where $\boldsymbol{u}$ is the velocity field) satisfies the quasistatic balance of momentum, so will any multiple of $\boldsymbol{D}$. In addition, they fail to account for dilatancy, or volume deformation caused by shear deformation, a distinctive feature of granular materials. Several models have been proposed to repair the shortcoming of kinematic indeterminacy, but they all assume the granular medium to be incompressible, thereby ignoring dilatancy.

In a recent paper [4], we proposed a nonlocal constitutive model that makes quasi-static flow kinematically determinate *and* incorporates dilatancy. The model is based on the simple and physically reasonable idea that plastic deformation and dilation at a point are caused by yielding not simply at that point, but in a mesoscopic region around it. The model is a systematic non-local extension of critical state plasticity [1], and introduces no additional variables or conservation equations.

Here we describe the model of Dsouza & Nott [4] and the predictions therein for steady plane Couette flow. Further, we discuss the time evolution of the density and velocity profiles and argue that a flow in the gradient direction must arise due to dilatancy. We argue that this dilatancy-driven flow is the likely cause of the anomalous vortices observed in cylindrical Couette flow [5] and in a split-bottom Couette cell [6].

Model description and predictions

The local plasticity model, namely critical state plasticity [1], comprises a yield condition and a flow rule, which are generally written as [3]

$$F(\boldsymbol{\sigma}) = 0, \quad D_{ij} = \dot{\lambda}\, \frac{\partial F}{\partial \sigma_{ji}}, \tag{1a,b}$$

where F is a scalar function of the the stress tensor $\boldsymbol{\sigma}$, and $\dot{\lambda}$ is the scalar 'fluidity' field. Dsouza & Nott [4] introduced non-locality with the following two arguments. They reasoned that the flow rule (1b) must be modified to hold only in the following volume-averaged sense,

$$D_{ij} = \int_{\boldsymbol{y}} \left[\dot{\lambda}\, \frac{\partial F}{\partial \sigma_{ji}}\right]_{\boldsymbol{y}} g(\boldsymbol{y} - \boldsymbol{x})\, \mathrm{d}\boldsymbol{y} \tag{2}$$

where the integral is over all space. Here $g(\boldsymbol{\xi})$ is a smoothly varying isotropic weight function sayisfying $\int g(\boldsymbol{\xi})\, \mathrm{d}\boldsymbol{\xi} = 1$ and $\int \boldsymbol{\xi\xi}\, g(\boldsymbol{\xi})\, \mathrm{d}\boldsymbol{\xi} = \ell^2 \boldsymbol{\delta}$, where $\boldsymbol{\delta}$ is the unit tensor and ℓ is the measure of nonlocality. Secondly, since deformation is accompanied by dilation or compaction, they argued that volume fraction ϕ too must be nonlocal,

$$\phi = \int_{\boldsymbol{\xi}} \left[\Pi^{-1}(p_{\mathsf{c}})\right]_{\boldsymbol{y}} g(\boldsymbol{y} - \boldsymbol{x})\, \mathrm{d}\boldsymbol{y}, \tag{3}$$

where p_{c} is the pressure at critical state [1, 2], whose local relation is $p_{\mathsf{c}} = \Pi(\phi)$.

Using the extended von Mises yield condition [3], which specifies the forms of $F(\boldsymbol{\sigma})$ and $\Pi(\phi)$, they derived the non-local constitutive relation

$$\boldsymbol{\sigma} = -p\,\boldsymbol{\delta} + \frac{2\mu}{\dot{\gamma}}\big(p_{\mathsf{c}}\, \boldsymbol{D}' - \ell^2\, \Pi\, \nabla^2 \boldsymbol{D}'\big), \tag{4a}$$

$$p_{\mathsf{c}} = \Pi - \ell^2\, \frac{\mathrm{d}\Pi}{\mathrm{d}\phi}\, \nabla^2 \phi, \tag{4b}$$

$$p = p_{\mathsf{c}}\big(1 - \frac{\mu_{\mathsf{b}}}{\dot{\gamma}} \boldsymbol{\nabla \cdot u}\big) + \ell^2\, \Pi\, \frac{\mu_{\mathsf{b}}}{\dot{\gamma}} \nabla^2 \boldsymbol{\nabla \cdot u}, \tag{4c}$$

where $\boldsymbol{D}'$ is the deviatoric part of $\boldsymbol{D}$, $\dot{\gamma} \equiv (2\boldsymbol{D}'{:}\boldsymbol{D}')^{1/2}$ is its scalar invariant, μ is the Coulomb friction coefficient, and μ_b is the friction coefficient for volume deformation. In (4), the terms of O(ℓ^0) are the local contributions, and the terms of O(ℓ^2) are the nonlocal corrections.

Figure 1 compares the predictions of the non-local model with the results of particle simulations using the discrete element method (DEM) for plane Couette flow in the absence of gravity. In the DEM simulations, the particles are of mean diameter d_p and the walls are composed of spheres of diameter d_w in a close packed array. The reader is referred to the original work [4] for the details on the boundary conditions and the parameter values used to obtain the solutions. The agreement between the model predictions and the DEM simulations is remarkably good, but we note the caveat that the form of $\Pi(\phi)$ used is based on scanty data. The point that we emphasize is the strong coupling between the velocity and volume fraction fields, which has thus far not been captured in continuum models. If ϕ is assumed to be constant, the inhomogeneity in the shear rate is significantly lower (red dash-dot curve in Fig. 1b).

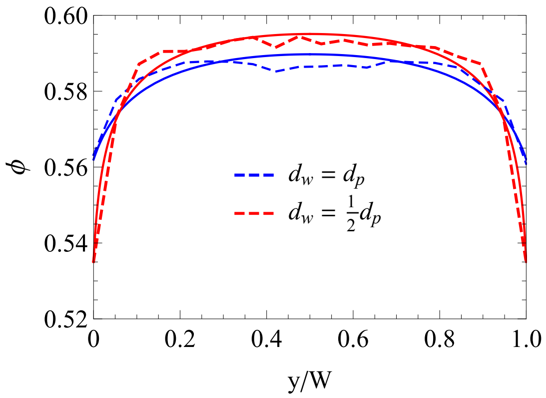

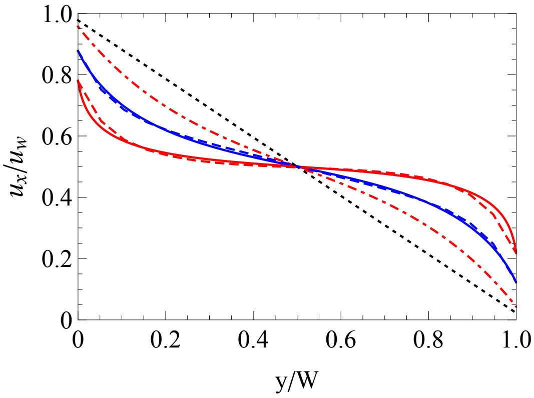

Fig. 1: Profiles of the volume fraction (a) and the velocity (b) for a Couette gap $W = 40\,d_\mathrm{p}$ and mean volume fraction 0.585. The dashed lines are the results of DEM simulations using wall particles of two sizes; the solid lines are the model predictions. In (b) the red dash-dot line is the model prediction for $d_\mathrm{w} = \frac{1}{2}d_\mathrm{p}$ when ϕ is assumed to be constant, and the black dotted line is the prediction for 'fully rough' walls. Taken from Dsouza & Nott [4]. Reprinted with permission.

While the results for steady fully developed flow in Fig. 1 are of value, it is equally of interest to understand how the velocity and volume fraction profiles develop in the transient state. For ϕ to decrease near the walls starting from an initial state of uniform density, there must be motion away from the walls. This can be understood by solving the transient equations of motion, for which the balances of mass and momentum (in the x and y directions) are coupled. We shall show that the non-local terms in (4b) and (4c) lead to a flow in the gradient direction away from regions of high shear rate. Though this is a simple illustration of dilatancy-driven flow, it yields important insight into how dilatancy can drive a highly non-trivial flow when gravity is present and its direction is not colinear with that of the imposed velocity gradient. This offers a partial explanation for the occurrence of secondary flows in the form of vortices observed recently in cylindrical Couette [5] and split-bottom Couette [6] devices. The results of the transient flow analysis are not given here, but will be presented at the meeting.

References

[1] Schofield, AN & Wroth, CP. *Critical State Soil Mechanics*. McGraw-Hill, 1968.

[2] Jackson, R. *Some mathematical and physical aspects of continuum models for the motion of the granular materials*. In *Theory of Dispersed Multiphase Flow* (ed. R. E. Meyer), 291–337, Academic Press, 1983.

[3] Rao, KK & Nott, PR. *An Introduction to Granular Flow*. Cambridge University Press, 2008.

[4] Dsouza, PV & Nott, PR. *J. Fluid Mech.* **888**:R3, 2020.

[5] Krishnaraj, KP & Nott, PR. *Nature Commun.* **7**:10630, 2016

[6] Dsouza, PV, Krishnaraj, KP & Nott, PR. *EPJ Web of Conferences, Powders and Grains*, Montpellier, France, July 3-7, 2017, **140** 03028.

*corresponding author: prnott@iisc.ac.in

RHEOLOGY OF A CONCENTRATED MONOLAYER OF SPHERICAL SQUIRMERS

Takuji Ishikawa[1], Douglas Brumley[2], Tim Pedley[3*]

[1]Department of Finemechanics, Tohoku University, Sendai, Japan
[2]School of Mathematics and Statistics, University of Melbourne, Australia
[3]Department of Applied Mathematics and Theoretical Physics, University of Cambridge, U.K.

Abstract

A concentrated, vertical monolayer of identical spherical squirmers, which may be bottom-heavy, and which are subjected to a horizontal shear flow, is modelled computationally by two different methods: Stokesian Dynamics, and a lubrication-theory-based method. The effective shear viscosity is found in general to be increased by the squirming motions.

BACKGROUND

Suspensions of swimming micro-organisms exhibit fascinating collective behaviour, ranging from steady, regular patterns, as in bioconvection [1], to random coherent structures, sometimes referred to as bacterial turbulence [2], with many variants in between. There have been many models of such behaviour, most of which have been developed to see if the observations can be explained by physical processes alone, without requiring an understanding of biological or chemical signalling or intracellular processes. Continuum models have been very successful for dilute suspensions, in which the cells interact with their environment but not with each other: bioconvection results from either a gravitational instability when the upswimming of dense cells leads to a gravitationally unstable density profile, or a gyrotactic instability in which the cells' non-uniform density or geometric asymmetry causes them to be reoriented in a shear flow [2]. Even when gravity is unimportant the stresses applied by the cells' swimming motions (a swimmer acts as a force dipole or stresslet) lead to instability and random bulk motions [3,4].

In this paper we wish to consider concentrated suspensions, in which the flow is dominated by cell-cell interactions. Continuum models fail because there is no agreed way of incorporating cell-cell interactions into the model equations – in particular the particle stress tensor $\mathbf{\Sigma}^{(\mathbf{p})}$ – even when the interactions are restricted to near-field hydrodynamics together with a repulsive force to prevent overlap of model cells. We seek to understand the rheological properties of an idealised suspension from direct numerical simulations. The cells are modelled as identical steady spherical squirmers [5,6,7]: spheres of radius a which swim by means of a prescribed tangential velocity on the surface, $u_\theta = \frac{3}{2}V_s \sin\theta(1+2\beta\cos\theta)$, where θ is the polar angle from the cell's swimming direction, V_s is the cell swimming speed and β represents the stresslet strength; inertia is negligible. The suspension is taken to be a monolayer, embedded in an infinite fluid, in which the sphere centres and their trajectories are confined to a single plane, which is vertical in cases for which gravity, $\mathbf{g}$, is important. The spheres may be bottom-heavy, so that when the swimming direction of a sphere, $\mathbf{p}$, is not vertical the sphere experiences a gravitational torque $\mathbf{L}$, where $\mathbf{L} = -\rho v h \mathbf{p}\times\mathbf{g}$ and v, h are the cell volume and the displacement of the centre of mass from the geometric centre; ρ is the average cell density, assumed the same as that of the fluid. The monolayer is taken to be driven by a simple shear flow in the same, $x-y$, plane: $\mathbf{U} = (\gamma y, 0, 0)$, with shear-rate γ; we will also take $\mathbf{g} = -g(\sin\alpha, \cos\alpha, 0)$, so the flow is horizontal if $\alpha = 0$.

METHODS

We have previously studied the rheology of semi-dilute (three-dimensional) suspensions of squirmers – volume fraction $c \le 0.1$ – in which every cell interacted only with its nearest neighbour [8]. General pairwise interactions could be computed exactly using the boundary element method, supplemented by lubrication theory when cells were very close together. Cells were prevented from overlapping computationally by the inclusion of a repulsive interparticle force $\mathbf{F} = \mu a^2\gamma F_0 \tau e^{-\tau\epsilon}/(1+e^{-\tau\epsilon})\hat{\mathbf{r}}$ where $\hat{\mathbf{r}}$ is the unit vector along the line of centres and ϵ is the minimum permitted dimensionless spacing [9]. In [8] τ was taken equal to 10^3 and F_0 was varied. It was found that the swimming activity made very little difference to the effective shear viscosity when the spheres were non-bottom-heavy, but the suspension showed significant non-Newtonian behaviour, such as anisotropic effective shear viscosity and normal stress differences, when the cells were bottom-heavy.

Here we use two different methods of simulation for very concentrated monolayer suspensions, with areal fraction c up to 0.7. One is a full numerical simulation using Stokesian Dynamics [9,10], while in the other we assume that cells in which every cell interacts with other cells in the domain and mirror domains by assuming additivity of forces. The interaction is described using lubrication theory alone. This model was recently used to investigate the stability of a regular array of bottom-heavy squirmers, swimming upwards in the absence of an imposed shear flow [11]. The point of this is to see if lubrication alone is good enough to account for all the interesting rheological behaviour of a concentrated suspension, or if some effect of more distant particles is necessary, in the case of squirmers. As well as illuminating the physics, this might make related computations significantly cheaper than the full Stokesian Dynamics. For inert and force-free spheres, Leshansky & Brady [12] reported in a footnote that suppressing all far field interactions made less than 5% difference to the quantities they were computing.

RESULTS AND DISCUSSION

In addition to β, α, τ, F_0 and the areal fraction c, the governing dimensionless parameters are: the dimensionless swimming speed, $Sq = \frac{V_s}{a\gamma}$, and $G_{bh} = \frac{\rho v g}{(3\mu a V_s)}$, the 'bottom-heaviness parameter'. The initial objective is to compute the effective shear viscosity, η_{eff}, which in Stokesian Dynamics is obtained from the off-diagonal terms of the particle stress tensor $\mathbf{\Sigma}^{(p)}$, defined as the average over all spheres of the stresslet for a single particle [13]:

$$\mathbf{S} = \int_{A_p} [\frac{1}{2}\{(\sigma \cdot \mathbf{n})\mathbf{x} + \mathbf{x}(\sigma \cdot \mathbf{n})\} - \frac{1}{3}\mathbf{x} \cdot \sigma \cdot \mathbf{n}\mathbf{I} - \eta(\mathbf{u}\mathbf{n} + \mathbf{n}\mathbf{u})]dA, \quad (1)$$

where σ is the stress tensor and $\mathbf{u}$ is the velocity. A_p is the surface of the particle with outward normal $\mathbf{n}$. Then

$$\eta_{eff} - 1 = 2.5c\frac{\langle S_{xy} + S_{yx}\rangle}{20\pi/3}. \quad (2)$$

The result of the Stokesian Dynamics simulations for horizontal shear flow ($\alpha = 0$) is that, for non-bottom-heavy spheres ($G_{bh} = 0$), η_{eff} increases with c more rapidly than for non-swimming spheres. Examination of the cell trajectories suggests that this is associated with the interior of the suspension forming horizontal layers when the spheres do not swim, but becoming very irregular when they do (presumably increasing the local rate of energy dissipation). The increase in η_{eff} is greater for larger swimming speeds ($Sq = 10$ rather than $Sq = 1$), but is not much affected by the squirming mode β ($-3 \leq \beta \leq 3$) or the magnitude of the inter-particle repulsion, F_0. Bottom-heaviness, in a horizontal flow, reduced η_{eff} in general, but not by much.

In the lubrication theory model η_{eff} is calculated in a different way: a regular array of squirmers is placed between two rigid planes parallel to the x-axis, at $y = \pm H$, and these are translated parallel to each other with speeds $\pm V$; only the cells closest to the planes are set into motion by them, through the stress in the lubricating layer, and these then cause their other neighbours to move too. Once the shear stress on the planes, S_W, has become steady, on average, η_{eff} is calculated as $\eta_{eff} = \langle S_W\rangle H/V$. Preliminary results indicate that η_{eff} is not greatly affected by the squirming alone, in the absence of bottom-heaviness. However, it is significantly reduced for bottom-heavy squirmers in horizontal shear flows. There have been few experimental studies on the effective viscosity of suspensions of microscopic swimmers. Notable among those few are the measurements of Rafai *et al.* [14] on suspensions of motile algae (*Chlamydomonas reinhardtii*), which are close to spherical, are bottom-heavy, and *pull* themselves through the fluid (equivalent in the squirmer model to $\beta > 0$). The effective viscosity in a horizontal shear flow was found to increase with volume fraction much more dramatically than for a suspension of dead cells, in agreement with the above Stokesian Dynamics prediction. On the other hand, Sokolov & Aronson [15] measured the effective viscosity of a suspension of bacteria (pushers: $\beta < 0$), and found a significant decrease in shear viscosity with swimming speed. However, this could be attributed to the rod-like geometry of the bacteria. Apparent agreement with our lubrication theory predictions is coincidental.

References

[1] Pedley, T.J. and Kessler, J.O. *Annu. Rev. Fluid Mech.* **24**:313-358, 1992

[2] Dombrowski, C., Cisneros, L., Chatkaew, S., Goldstein, RJ.O. *Phys. Rev. Lett.* **93**:098103, 2004

[3] Simha, R.A. and Ramaswamy, S. *Phys. Rev. Lett.* 89:058101, 2002

[4] Saintillan, D. and Shelley, M.J. *Phys. Fluids* **20**:123304, 2008

[5] Lighthill, M.J. *Comm. Pure Appl. Math.* **5**:109-118, 1952

[6] Blake, J.R. *J. Fluid Mech.* **46**:199-208, 1971

[7] Ishikawa, T., Simmonds, M.P. and Pedley, T.J. *J. Fluid Mech.* **568**:119-160, 2006

[8] Ishikawa, T. and Pedley, T.J. *J. Fluid Mech.* **588**:399-435, 2007

[9] Brady, J.F. and Bossis, G. *J. Fluid Mech.* **155**:105-129, 1985

[10] Ishikawa, T., Locsei, J.T. and Pedley, T.J. *J. Fluid Mech.* **615**:401-431, 2008

[11] Brumley, D.R. and Pedley, T.J. *Phys.Rev. Fluids* **4**:053102, 2019

[12] Leshansky, A.M. and Brady, J.F. *J.Fluid Mech.* **527**:141-169, 2005

[13] Batchelor, G.K. and Green, J.T. *J.Fluid Mech.* **56**:401-427, 1972

[14] Rafai, S., Jibuti, L. and Peyla, P. *Phys.Rev.Lett.* **104**:098102, 2010

[15] Sokolov, A. and Aronson, I.S. *Phys.Rev.Lett.* **103**:148101, 2009

*corresponding author: tjp3@cam.ac.uk

Granular Rafts

Suzie Protiere [1*], Antoine Lagarde[1], Christophe Josserand[2]

[1] Institut Jean Le Rond ∂'Alembert, CNRS UMR 7190, Sorbonne Universit, F-75005 Paris, France
[2] LadHyX, CNRS, Ecole Polytechnique, UMR 7646, 91128 Palaiseau, France

Introduction

When two identical objects are deposited at a liquid interface, their individual deformations overlap, leading to an attractive force. This everyday phenomenon is central in many applications, from industrial processes where it is used to manufacture objects with a specific microstructure to Nature where fire ants gather into a raft to survive floods.

Here, we study experimentally the formation and life of an axisymmetric monolayer of spherical beads at an oil-water interface, called a granular raft [1]. We first quantify the capillary interaction between two granular rafts, and exhibit its dependency with the number of particles in each aggregate. Once the attracting force described, we focus on the erosion a raft can be subjected to when in motion. The loss of particles during its displacement can lead to a modification of the forces experienced. We study this erosion process, and deduce the cohesion forces keeping a particle inside a raft. Finally we investigate the many-body interaction of non-identical aggregates. Thanks to our precise understanding of the interaction between two rafts, we undertake a statistical description of the aggregation of a n-body system into a single giant granular raft.

Erosion of a granular raft

When a granular raft is made of small enough particles (radius $R_{part} <$ 0.2 mm), erosion can occur [3] if its speed exceeds a given threshold. Particles detach behind the raft, modifying its global shape while it is still moving. This erosion mechanism is illustrated in figure 1, where a granular raft is filmed from above as its speed increases. The general shape of the raft changes as the velocity increases, until a point where it cannot even maintain the cohesion of its constitutive elements, leading to the loss of a few beads behind.

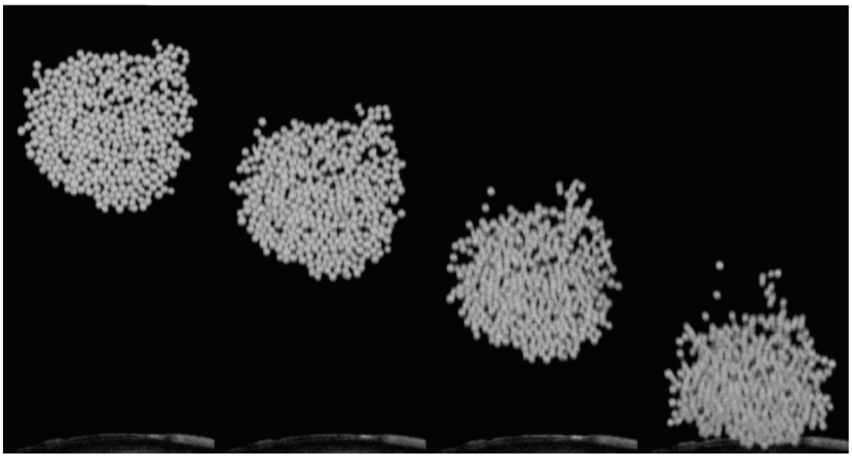

Fig. 1: Top view centered on a granular raft (ZrO beads, density 3,800 kg.m^{-3}, radius 0.125 mm) during its motion at an oil-water interface. The motion of the raft is directed from top to bottom and its instantaneous speed increases from left to right. Time between two photos: 0.25s.

The cohesion force is then measured for a large variety of beads (several radii and densities) with a model experiment testing the cohesion force between two beads. For small particles (Bond number $Bo = (R/\ell_c)2 < 0.002$, with ℓ_c the capillary length), this force appears to be several orders of magnitude higher than the capillary force predicted by the classical linear so-called Cheerios effect [2]. We quantify the dependency between this cohesion force and the particle parameters (radius, density, contact angle).

Interaction between rafts and formation of granular rafts

We then focus on the interaction forces between non-identical clusters of particles. We find that the vertical deflection of the interface can strongly depend on the number of particles they consist of, leading to unusually high capillary forces. In parallel, the viscous drag experienced is also affected by the size of the raft. By measuring the velocity profiles, we derive a model for both the capillary interaction and the drag force, and confirm these experimental results with some numerical simulations for the shape of a raft. The model developed strongly relies on the assumption that the discrete nature of a raft can be neglected to account for its motion, the raft being modeled as a heavy membrane.

Conclusion

The aggregation of particles at an interface has been thoroughly studied for a model system of two or more interacting clusters. The erosion of a raft is also characterized, through the measurement of the force responsible for its cohesion. From this understanding of the interaction between two rafts, as well as of their cohesion, we try to generalize our work to a system of n rafts, each one formed of a random number of particles, and describe statistically the aggregation process of such n-body system, from the distribution of sizes through time to the duration of collapse of all the particles into one single object.

References

[1] S. Protiere, C. Josserand, J. M. Aristoff, J. M. Aristoff, H. A. Stone and M. Abkarian. *Physical Review Letters* **118** 108001 2017.
[2] D. Vella and L.Mahadevan. *American journal of physics* **73**:817-825 2005.
[3] N. D. Vassileva, D. van den Ende, F. Mugele and J. Mellema. *Langmuir* **23**:2352-2361 2007.

*corresponding author: protiere@ida.upmc.fr

Modelling of damage of a liquid-core microcapsule in simple shear flow until rupture

N. Grandmaison[1], D. Brancherie[2], A.-V. Salsac[1]*

[1]Biomechanics and Bioengineering Laboratory, CNRS - Université de Technologie de Compiègne, Compiègne, France
[2]Roberval Laboratory, CNRS - Université de Technologie de Compiègne, Compiègne, France

Introduction

Capsules composed of a droplet surrounded by a deformable wall are used in numerous industrial applications to protect and ensure the controlled delivery of an active agent. When capsules are in flow, the viscous forces from the external flow can damage the capsules, potentially until breakup. Damage corresponds to the formation of microdefects in the wall which modify the properties of the capsule locally and thus the exchanges between the inner and the outer fluids. As a domino effect, it can lead to rupture as the accumulation of the microdefects can initiate a crack that propagates over the wall. The protection/release of the encapsulated agent is thus conditioned by the control of the damage of the capsule.

There are numerous contributions on the study of the dynamics of capsules in flow [1]. Few of them have, however, studied the rupture of capsules, the approach having been only experimental (see e.g. [2, 3]). The damage phase in the rupture process has thus never been studied. We propose to enrich a fluid-structure interaction model by modelling damage at the macroscale using the framework of continuum damage mechanics (CDM) (see e.g. [4] for a recent review), that offers a systematic approach of rupture for structures. In this work, we incorporate, for the first time, a CDM model into a fluid-structure interaction framework and study the damage process of a capsule in flow until the initiation of rupture.

Model

We consider an initially spherical capsule of radius a. The wall is assumed to be of very small thickness and is modelled as a membrane of mid-plane S and surface shear modulus G_s. The capsule is immersed in a simple shear flow of shear rate $\dot{\gamma}$. The internal and external fluids are the same incompressible Newtonian fluids of dynamic viscosity μ. Considering a capsule of microscopic size, the gravitational and inertial effects are negligeable compared to the viscous and elastic effects. Hence the only dimensionless parameter that governs the fluid-structure interaction is the capillary number $Ca = \mu a \dot{\gamma}/G_s$ that compares the fluid viscous forces to the membrane elastic forces.

The flows are governed by the Stokes equations. The boundary integral method [5] gives an explicit expression of the velocity $\underline{v}$ of the fluids on S as a function of the jump of viscous stresses $[\![\underline{\underline{\sigma}}]\!] \cdot \underline{n}$ across the membrane:

$$\forall \underline{x} \in S, \quad \underline{v}(\underline{x}) = \underline{v}^{\infty}(\underline{x}) - \frac{1}{8\pi\mu} \int_S \underline{\underline{J}}(\underline{x}, \underline{y}) \cdot [\underline{\underline{\sigma}}] \cdot \underline{n}(\underline{y}) \, \mathrm{d}S_{\underline{y}} \,, \tag{1}$$

where $\underline{v}^{\infty}$ is the velocity of the unperturbed simple shear flow and $\underline{\underline{J}}$ is the second order Oseen-Burgers tensor.

The membrane is at equilibrium at any instant. Hence, the principle of virtual works gives a relation between the internal tension tensor $\underline{\underline{T}}$ of the membrane and the external load vector $\underline{q}$ on the membrane:

$$\text{for any virtual displacement } \underline{\hat{u}}\,, \quad \int_S \underline{\underline{T}} : \underline{\underline{\varepsilon}}(\underline{\hat{u}}) \, \mathrm{d}S = \int_S \underline{\hat{u}} \cdot \underline{q} \, \mathrm{d}S \,, \tag{2}$$

where $\underline{\underline{\varepsilon}}(\underline{\hat{u}})$ is the symmetric part of the surface gradient of $\underline{\hat{u}}$.

The motions of the fluids and the membrane are coupled by imposing the continuity of the velocities and the stresses (i.e. the jump of viscous stress $[\![\underline{\underline{\sigma}}]\!] \cdot \underline{n}$ equals the external load $\underline{q}$) on the interface S.

The damage of the membrane is modelled in the standard framework of CDM. The damage variable d is chosen to be a scalar that ranges from 0 (sound material) to 1 (macrocrack initiation). The choices for the free energy and for the damage criterion are given in Table 1. The expression of the damage criterion f is chosen from a model developped by Marigo [6] for brittle damage, where we introduce the two parameters Y_D and Y_C representing an initial damage threshold and a hardening modulus, respectively. Following the standard framework, we derive the damage evolution law from the normality

Table 1: Damage model of the membrane. ϕ_{NH} is the free energy of a Neo-Hookean material.

Surface density of free energy	$\phi = (1-d)\phi_{NH}$
Damage criterion	$f = -\dfrac{\partial \phi}{\partial d} - (Y_D + Y_C d)$

law and the consistency condition:

$$\begin{cases} f < 0 \implies \dot{d} = 0 \\ f = 0 \implies d = (-\dfrac{\partial \phi}{\partial d} - Y_D)/Y_C. \end{cases} \tag{3}$$

Numerical method

We perform a Lagrangian tracking of the membrane. At the begining of a given time step, the current configuration of the membrane is known. We begin by solving the solid problem (eqs. (2), (3)) with the finite element method. It consists of, first, solving the local problem of damage evolution (eq. (3)) at the integration points, and then, the global problem of equilibrium (eq. (2)) to find the external load at the nodes. We then solve the fluid problem by computing the velocity of the fluids at the nodes using eq. (1). Finally, following the method developed by Walter *et al.* [5], we integrate the velocity explicitly with a second-order Runge-Kutta scheme to determine the position of the nodes at the following time step.

Results

We have studied the damage process of a capsule as a function of the value of Ca for given values of the dimensionless damage parameters Y_D/G_s and Y_C/G_s. Damage occurs when Ca is larger than a critical value Ca_c and leads to the initiation of rupture if Ca is larger than a limit value Ca_ℓ. When there is no damage ($Ca < Ca_c$), the motion of the capsule is known in the literature (see e.g. [5]): the capsule elongates in the flow strain direction, reaches a steady ellipsoidal shape and the membrane rotates around the vorticity axis (Figure 1a). When $Ca > Ca_c$, damage develops on the flanks of the capsule around the tip on the vorticity axis while the capsule elongates. If $Ca < Ca_\ell$, the capsule reaches a steady damaged state (Figure 1b), but when $Ca \geqslant Ca_\ell$, rupture is initiated when $d = 1$: it occurs at the tips of the vorticity axis (Figure 1c). The dimensionless damage parameters Y_D/G_s and Y_C/G_s influence the values of the thresholds Ca_c and Ca_ℓ and the intensity of damage.

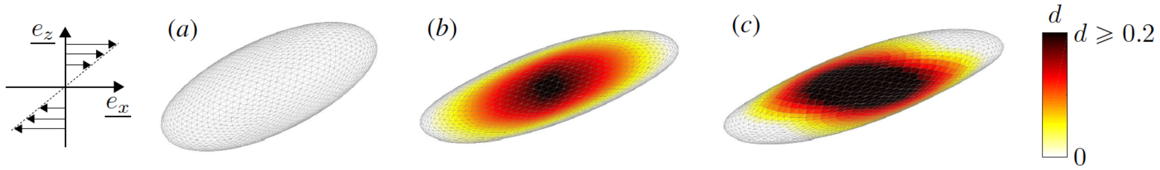

Fig. 1: Damage of a capsule in simple shear flow observed, at steady state, in the shear plane ($\underline{e_x}$, $\underline{e_z}$) from the side, for (*a*) $Ca \leqslant Ca_c$ and (*b*) $Ca_c < Ca < Ca_\ell$, and (*c*) $Ca \geqslant Ca_\ell$ (shown at the instant of initiation of rupture, i.e. when $d = 1$ at the center of the capsule). Damage is symmetric with respect to the shear plane.

In conclusion, the model proposed in this work enables to study the damage process and the criteria that control rupture of a capsule in flow.

Acknowledgements

This project has received funding from the European Research Council (ERC) under the European Union Horizon 2020 research and innovation programme (Grant agreement No. ERC-2017-COG - MultiphysMicroCaps).

References

[1] Barthès-Biesel D. Motion and deformation of elastic capsules and vesicles in flow. *Annual Review of Fluid Mechanics* **48**: 25-52, 2016.

[2] Chang K.S., Olbricht W.L. Experimental studies of the deformation and breakup of a synthetic capsule in steady and unsteady simple shear flow. *J. Fluid Mech.* **250**: 609-633, 1993b.

[3] Koleva I., Rehage H. Deformation and orientation dynamics of polysiloxane microcapsules in linear shear flow. *Soft Matter* **13**: 3681-3693, 2012.

[4] Lemaitre J., Desmorat R. *Engineering Damage Mechanics*. Springer, 2005.

[5] Walter J., Salsac A.-V., Barthès-Biesel D., Le Tallec P. Coupling of finite element and boundary integral methods for a capsule in a Stokes flow. *Int. J. Numer. Meth. Engng.* **83**: 829-850, 2010.

[6] Marigo J. J. Formulation d'une loi d'endommagement d'un matériau élastique. *C. R. Acad. Sci. Paris* **292**: 1309-1312, 1981.

*corresponding author: a.salsac@utc.fr

Encounter rates involving elongated marine microorganisms.

Jonasz Słomka[1]*and Roman Stocker[1]

[1]Institute for Environmental Engineering, Department of Civil, Environmental and Geomatic Engineering, ETH Zurich

Introduction

Marine microorganisms control the global biogeochemistry of the oceans through interactions between individual cells and between cells and particles of organic matter. Prominent examples include marine snow formation by elongated phytoplankton following a phytoplankton bloom or bacterial degradation of marine snow responsible for carbon export from the upper ocean in the biological pump. A variety of physical mechanisms can drive these interactions, including diffusion, active swimming, gravitational settling and turbulent mixing, and the concept of encounter rates provide a unifying framework to describe them. However, the corresponding collision kernels, which map the physical mechanisms to the frequency of encounters, have been traditionally computed for spherical particles. Here, we first describe the impact of elongation on marine snow formation. We derive the collision kernels between identical and dissimilar rods settling in a quiescent fluid and show that marine snow formation by elongated phytoplakton can proceed efficiently even under quiescent conditions and that the resulting coagulation dynamics can lead to periodic bursts in the concentration of marine snow particles [1, 2]. Later, we describe the impact of elongation and fluid shear on the encounters between non-motile and motile bacteria and sinking particles of organic matter [3]. There, we find that the shape-shear coupling has a considerable effect on the encounter rate and encounter location through the mechanisms of hydrodynamic focusing and screening. Overall, our results demonstrate that elongation and fluid shear must be taken into account to accurately predict encounter rates at the microscale, which govern the large carbon flux in the ocean's biological pump.

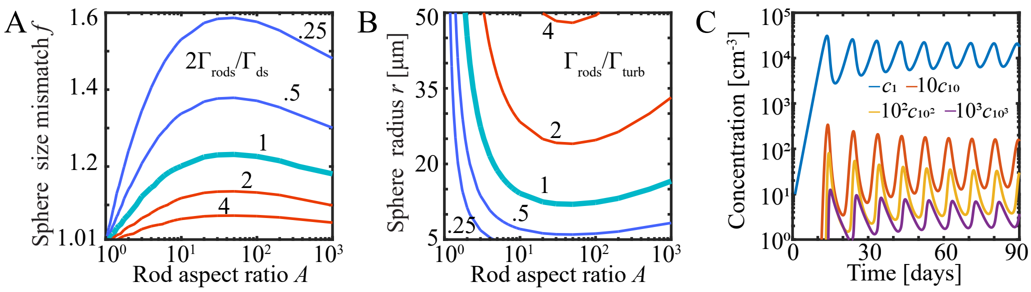

Fig. 1: (A,B) Comparison between the collision kernel Γ_{rods} for identical rods settling in a quiescent fluid [Eq. (1)] and the collision kernels for spheres colliding by two different mechanisms: differential settling due to small size mismatch [(A)] and turbulence-induced encounters of identical spheres [(B)]. (C) In the full Smoluchowski model for coagulation, periodic bursts characterize the statistically stationary concentration profiles of elongated aggregates.

Marine snow formation by elongated phytoplankton

Rods settling under gravity in a quiescent fluid can overcome the bottleneck associated with aggregation of equal-size spheres because they collide by virtue of their orientation-dependent settling velocity. We find the corresponding collision kernel

$$\Gamma_{\text{rods}} = l\beta_1 \Delta\rho V_{\text{rod}} g/(16A\mu), \tag{1}$$

where l, A and V_{rod} are the rods' length, aspect ratio (length divided by width) and volume, respectively, $\Delta\rho$ is the density difference between rods and fluid, μ is the fluid's dynamic viscosity, g is the gravitational acceleration and $\beta_1(A)$ is a geometrical parameter [1]. We apply this formula to marine snow formation following a phytoplankton bloom. Over a broad range of aspect ratios, the formula predicts a similar or higher encounter rate between rods as compared to the encounter rate between (equal-volume) spheres aggregating either by differential settling or due to turbulence (Fig. 1A,B). Since many phytoplankton species are elongated, these results suggest that collisions induced by the orientation-dependent settling velocity can contribute significantly to marine snow formation, and that marine snow composed of elongated phytoplankton cells can form at high rates also in the absence of turbulence.

We then extend the above results to the case of dissimilar rods, including rods that can differ between each other by density, length or aspect ratio [2]. We find an exact formula for the corresponding

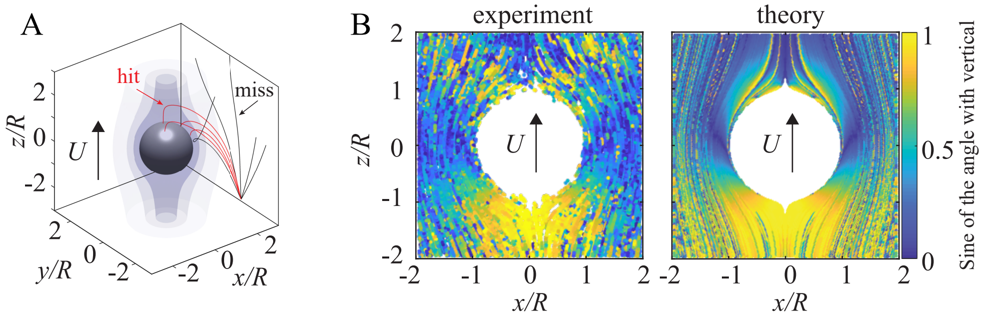

Fig. 2: (A) The ballistic Jeffrey-type model of the encounter between bacteria and sinking particles includes the impact of shear on bacterial trajectories. (B) Experiments with non-motile elongated diatom cells (*Phaeodactylum tricornutum*) are consistent with the predictions of the model that rods orient tangentially (normally) upstream (downstream) of the sinking particle. Each dot represents position and orientation of a diatom cell.

collision kernel, valid in the limit of thin rods. For dissimilar rods of finite width, we provide an integral formula for the collision kernel, which is easily evaluated numerically. Motivated by marine snow formation between elongated phytoplantkon cells, we then apply the kernel to study coagulation of elongated particles in a quiescent fluid. Assuming elongated cells form bundles of the same length as the individual cell but of greater width, we discover a strong coupling between the thinnest and thickest bundles, rather than between bundles of similar size. By contrast, models based on spherical particles predict strong coupling between aggregates of similar size. In the full Smoluchowski model for coagulation that combines exponential growth of cells with settling, the thin–thick coupling leads to statistically stationary states where the concentration of aggregates of different size oscillate in time, characterized by periodic bursts occurring on the scale of a week (Fig. 1C).

Encounter rates between bacteria and small sinking particles

Bacteria in aquatic environments often interact with particulate matter. A key example is bacterial degradation of marine snow responsible for carbon export from the upper ocean in the biological pump. The ecological interaction between bacteria and sinking particles is regulated by their encounter rate, which is therefore important to predict accurately in models of bacteria-particle interactions. Models available to date cover the diffusive encounter regime, valid for sinking particles larger than the typical run length of a bacterium. The majority of sinking particles, however, are small, and the encounter process is then ballistic rather than diffusive. In the ballistic regime, the shear generated by the particle's motion can be important in reorienting bacteria and thus determining the encounter rate, yet the effect of shear is not captured in current encounter rate models. Here, we combine analytical and numerical calculations to quantify the encounter rate between sinking particles and non-motile or motile microorganisms in the ballistic regime, explicitly accounting for the hydrodynamic shear created by the particle and its coupling with microorganism shape (Fig. 2A). We complement results with selected experiments on non-motile diatoms (Fig. 2B). We find that the shape—shear coupling has a considerable effect on the encounter rate and encounter location through the mechanisms of hydrodynamic focusing and screening (Fig. 2B), whereby elongated microorganisms preferentially orient normally to the particle surface downstream of the particle (focusing) and tangentially to the particle surface upstream of the particle (screening). Non-motile elongated microorganisms are screened from sinking particles in ballistic interactions because shear aligns them tangentially to the particle surface. As a result, the encounter rate is reduced by a factor proportional to the square of the microorganism aspect ratio as compared to a spherical microorganism. For motile elongated microorganisms, hydrodynamic focusing increases the encounter rate approximately twofold compared to the case without shear when particle sinking speed is similar to microorganism swimming speed, whereas for very quickly sinking particles hydrodynamic screening can reduce the encounter rate below that of non-motile microorganisms.

Conclusions

Elongated morphologies are ubiquitous among marine phytoplankton and bacteria. By studying marine snow formation by phytoplankton and encounters between bacteria and sinking particles, we demonstrated that elongation and hydrodynamic shear are important determinants of the countless encounter processes at the ocean microscale, which govern the global biogeochemistry of the oceans.

References

[1] Słomka J & Stocker R. *PNAS*, 2020.
[2] Słomka J & Stocker R. *submitted*, 2020.
[3] Słomka J, Alcolombri U, Secchi E, Stocker R & Fernandez I V. *New J. Phys. (accepted) 2020*.

*corresponding author: jslomka@ethz.ch

Propulsion by pitching and heaving foils

A. J. Smits*

Princeton University, Princeton NJ 08544, U.S.A.

Introduction

The thrust and power performance of simple rigid foils moving in oscillatory motion in water is of interest in helping to understand the swimming action of aquatic animals, and the propulsion of a new generation of underwater vehicles [1]. Here, we confine our attention to cases where the propulsive force is derived from the action of hydrodynamic and added-mass forces. For a surface craft, the analysis would apply to sculling over the stern where a single oar is worked over the transom, rather than ordinary rowing where the thrust is primarily produced by drag. For fish, it would apply, at least approximately, to fast-swimming fish such as tuna where the principal source of propulsion is the side-to-side action of the caudal fin, and also for mammals such as dolphins where it is due to the up-and-down action of the fluke. In these examples, the motion of the propulsive element without acceleration may be represented as a combination of pitch θ and heave h [2, 4], where

$$\theta(t) = \theta_0 \sin(2\pi f t + \phi), \quad h(t) = h_0 \sin(2\pi f t)$$

(f is the frequency, ϕ is the phase difference). The performance can be expressed in terms of the thrust and power coefficients, and efficiency, according to

$$C_T = \frac{F_x}{\frac{1}{2}\rho U_\infty^2 sc}, \quad C_P = \frac{F_y \dot{h} + M\dot{\theta}}{\frac{1}{2}\rho U_\infty^3 sc}, \quad \eta = \frac{C_T}{C_P}$$

(F_x is the thrust produced by the foil, F_x is the side force, U_∞ is the speed of motion, M is the moment taken about the leading edge, s is the span, c is the chord length).

Combined Heave and Pitch

For a pitching foil thrust is produced by the component in the streamwise direction of the added mass force, while for a heaving foil thrust is produced by the component in the streamwise direction of the lift force. Simple hydrodynamic models for the lift and added mass forces seem to do remarkably well in scaling the performance of rectangular foils in either pitch or heave motion [2], and for combined pitch and heave motions [4]. A phase difference of about 270° appears to yield the highest efficiency, and this condition corresponds closely to what is observed in the swimming motion of many fish and mammals. Under these circumstances, the thrust and power for an effectively two-dimensional foil are represented well by a reduced model where

$$C_T = c_1 St^2 - C_D, \qquad C_P = c_2 f^* St^2 \left(1 - H^* \Theta^*\right). \tag{1}$$

Here, $St = 2fa_0/U_\infty$, $H^* = h_0/a_0$, $\Theta^* = c\theta_0/a_0$, and a_0 is the peak amplitude of the trailing edge motion [3]. The constants c_i are determined empirically. Recent results on large-amplitude motions, as shown in Fig. 1, confirm the usefulness of the model and its range of applicability [6].

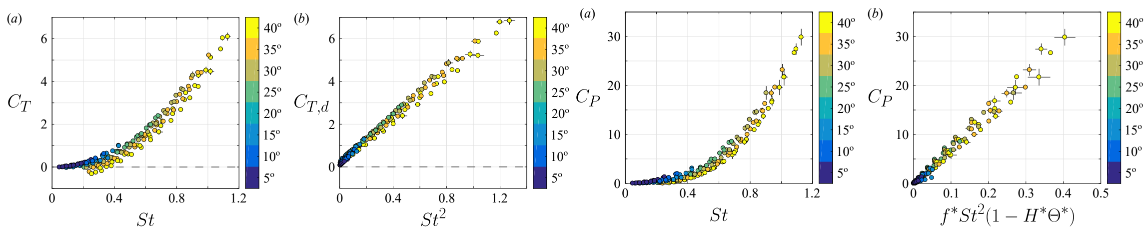

Fig. 1: Coefficients of thrust (left) and power (right) as a function of St, and scaled according to Eqn. 2. Color indicates θ_0. Heaving amplitude covers the range $0.125 \leq h_0/c \leq 0.75$. From [6].

The cycle-averaged drag coefficient of the foil, C_D, is a determining factor in the efficiency; it is primarily due to pitch [4], and it also depends on Reynolds number [5]. For a teardrop foil, C_D varies linearly with the pitch angle amplitude θ_0, and so we arrive at an expression for the efficiency (with $A^* = a_0/c$), given by

$$\eta \sim \frac{A^* \left(St^2 - a_1 \theta_0\right)}{St^3 \left(1 - H^* \Theta^*\right)} \tag{2}$$

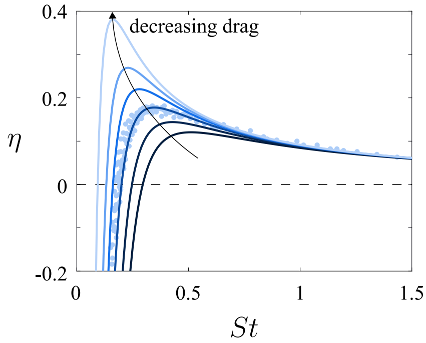

Fig. 2: Efficiency η as a function of St. Data are as given for a heaving and pitching NACA0012 foil. Solid lines are given by Eqn. 2 with a fixed proportionality constant of 0.155. The drag constant, a_1, is set to 0.5, 0.35, 0.23, 0.15, 0.1, and 0.05 as the colors vary from dark to light. From [3].

[3]. For any given operating point, the peak efficiency is obtained at $St = \sqrt{3a_1\theta_0}$, highlighting the important role that drag plays in determining the performance, as shown in Fig. 2. In addition, high efficiency is achieved with large values of A^*, small values of drag, and the "right" balance of heave and pitch. The amplitude of the motion is limited either by the physiology, or the onset of dynamic stall. The drag can be reduced by shaping the foil, and by increasing the Reynolds number [5, 7].

Effect of Aspect Ratio

The results considered so far were for effectively two-dimensional foils. Reducing the aspect ratio (here, $\mathcal{R} = s/c$) will generally diminish the thrust and efficiency. For the contribution due to lift (heave), the circulatory forces will be important, and so it seems likely that they would depend on aspect ratio as indicated by finite wing theory, that is, they would reduce by the factor $\mathcal{R}/(\mathcal{R}+2)$. Recent results support this expectation [8], although the results for finite wing theory are probably not reliable for $\mathcal{R} < 1$, and for more complicated planform shapes.

For the contribution due to added mass (pitch), for small aspect ratio panels we would expect the added mass to vary as $\rho s^2 c$, that is, the circumscribing circle that is at the heart of added mass models is defined by the span. This is also used in slender body theory where the circumscribing circle is defined by the cross-sectional area of the body. However, for large aspect ratio panels we would expect the added mass term to vary as $\rho s c^2$, that is, the circumscribing circle is defined by the chord. Based on recent observations [1], it appears that the cross-over point from small- to large-aspect ratio rectangular panels occurs at $\mathcal{R} \approx 2$.

Summary

For rigid, rectangular panels in combined heave and pitch motions, simple models based on circulatory and added-mass forces appear to describe the thrust and efficiency behavior even for large-amplitude motions. Such models give insight into optimizing the design of propulsors for underwater vehicles and understanding the swimming performance of fish and mammals. This work has been supported by the Office of Naval Research through Program Manager R. Brizzolara.

References

[1] Smits, A. J. *JFM*, **874**: P1-P70, 2019.
[2] Floryan D. et al. *JFM*, **822**: 386-397, 2017.
[3] Floryan D. et al. *PNAS*, **115**: 8116-8118, 2018.
[4] Van Buren, T. et al. *AIAA J.*, **57**: 3666-3677, 2019.
[5] Sentürk, U. and Smits, A. J. *AIAA J.*, **57**: 2663–2669, 2019.
[6] Floryan D. et al. *PRF*, **4**: 093102, 2019.
[7] Van Buren, T. et al. *AIAA Paper 2019-1379*, 2019.
[8] Ayancik, F. et al. *J. Fluid Mech.*, **871**: 1117–1138, 2019.

*corresponding author: asmits@princeton.edu

Driven and self-propelled colloids at fluid interfaces

N. G. Chisholm[1], K. J. Stebe[1*]

[1]Department of Chemical and Biomolecular Engineering, University of Pennsylvania, Philadelphia, PA 19104, USA

Driven and active colloidal systems exhibit unique and useful behaviors such as collective motion and enhanced mass transport. While these systems are well-studied in bulk fluids, less is known about their behavior under the influence of boundaries, which can strongly alter the motion of nearby colloids and the fluid flows they generate. Fluid-fluid interfaces provide a particularly rich and useful class of boundaries because they can exhibit a variety of mechanical properties that can be readily tuned, e.g., by the addition of surfactants. Thus, fluid interfaces provide untapped opportunities to assert precise control over active colloidal systems via boundary guidance.

In this work, we quantify the flows generated by driven and self-propelled colloids at fluid-fluid interfaces by developing an appropriate flow singularity model, focusing on the leading-order modes most influential to hydrodynamically induced mixing and colloid-colloid interactions. We consider both externally driven colloids and self-propelled colloids (swimmers) either near or adhered to the interface. While they are otherwise free to move about the interface, we assume that interfacially adhered colloids have a pinned contact line, which prevents their translation normal to the interface and rotation about an axis parallel to the interface. This assumption is motivated by known behavior of passive colloids at interfaces, which become similarly pinned. The Reynolds and capillary numbers are assumed small, in line with typical colloidal systems involving an air- or oil-water interfaces, and we assume that the interface is flat.

First, we consider a “clean” or surfactant-free interface. The interface acts to trap colloids, prevent fluid flux, and resist deformation of the interface. Akin to those in the bulk, colloids driven by external forces and torques can exert Stokelets parallel to the interface and rotlets perpendicular to the interface, respectively. Colloids driven normal to the interface are simply trapped and do not move or create flow. Swimmers are more interesting; they can drive motion in configurations parallel or normal to the interface. Viewed as a force dipole, swimmers moving parallel to the interface are found to generate flows similar to those in a bulk fluid. However, important new flow modes arise for active colloids pinned to the interface. Motivated by experimental observation, we then consider an interface that acts as a surface-incompressible layer. This behavior occurs, for example, when the Marangoni number is large, as is often the case if even scant surfactant is present. Interestingly, the incompressibility restriction substantially weakens flows directed normal to the interface unless the colloid experiences a net hydrodynamic torque that is balanced by a torque on the interface itself. This observation has potentially important implications for mass transport enhancement near boundaries. Finally, we compare our theoretical results with experimental flow fields generated by driven and active colloids. Specifically, we image displacement fields around a magnetic colloid forced to translate at constant velocity along an oil-water interface, and around an actively swimming bacterium, *P. Aeruginosa*, trapped at an oil-water interface. Our work is relevant to bacterial colonization of complex interfaces and control of artificial microswimmers via boundary guidance.

*corresponding author: kstebe@seas.upenn.edu

Modern applications of classical ideas in fluid mechanics: thin films, physical chemistry and molecular biology

H. A. Stone

Department of Mechanical and Aerospace Engineering, Princeton University, Princeton, NJ 08540

Abstract

Fluid mechanics has a rich history. Many classical ideas are discussed in Batchelor's *An Introduction to Fluid Dynamics*, which was written about the time(mid-1960s) that he was transitioning from a research focus on turbulence to studies of microhydrodynamics. The latter, combined with the desire to highlight the continued insight offered by classical ideas in fluid dynamics, motivates the selection of themes for this talk. In particular, modern research themes in science and engineering introduce new questions, some of which can be understood using fundamental concepts. We will provide two examples of research discoveries from the subjects of thin film dynamics, and cellular biology and in each case illuminate the phenomenon using fundamental ideas in fluid dynamics. In the first example, we will document experimentally the time and (three-dimensional) space variations of the shape of a falling film near the edge of a vertical plate and rationalize the quantitative features using a similarity solution. As a second example, we discuss the formation of the spindle in a dividing cell, and report experiments documenting a condensed protein phase on growing microtubules, followed by the Rayleigh-Plateau instability, which produces discrete droplets along a microtubule, that then drives branching nucleation. If there is time we will discuss recent interest in physicochemical hydrodynamics where motion of colloidal particles is driven by chemical gradients; we highlight the role of the difference of ion valences and background electrolyte. (The work discussed here involves many collaborators at Princeton including Bernardo Gouveia, Ankur Gupta, Sabine Petry, Sagar Setru, Suin Shim, Josh Shaevitz, Jessica Wilson and Nan Xue.)

*corresponding author: hastone@princeton.edu

On the collision of a rigid sphere with a deformable membrane in a viscous fluid

R. Verzicco[1]*, G. Querzoli[2]

[1]Uniroma2, Roma, Italy; GSSI, L'Aquila, Italy, UTwente, Enschede, The Netherlands
[2]DICAAR, Università di Cagliari, Cagliari, Italy

Abstract

In most natural phenomena and technological applications, the contact between two bodies is mediated by a fluid whose motion generates fluid dynamic forces. These, in turn, alter the motion of the objects and in some cases yield a completely different dynamics. If the fluid is a gas, with a density much smaller than that of the bodies, the presence of the fluid medium can be usually neglected and many models for the contact of solid bodies are available [1]. However, when the interacting bodies are immersed in a liquid, inertia and viscous stresses produce significant loads and the effect of the fluid has to be accounted for.

Concerning the bodies, in the interaction among rigid objects the deformations are small and limited to a well defined point (or set of points) of contact, thus allowing for simple force [2] and flow [3] models.

If the bodies are deformable, but the shapes can be described by a reduced set of parameters (like small bubbles or droplets), their contact can still be described by simple algorithms [4]. In contrast, for the interaction among arbitrarily deformable objects effective contact models are still missing and this study aims at progressing in that direction.

The motivation for this investigation comes from the dynamics of the heart valves whose leaflets move passively as a result of the hemodynamic loads. When a valve closes, its leaflets seal by coapting along a contact surface that is unknown and must be determined as part of the solution. For this application, however, the complex geometrical configuration, the multiple structures in relative motion and the pulsatile flow [5] yield an exceedingly difficult and computationally expensive problem that prevents its systematic study.

In order to retain only the essential features of the phenomenon of interest, here we focus on a simpler model problem which is the collision of a rigid spherical pendulum with a rectangular deformable membrane, clamped at its upper border and immersed in water. In fact, while the geometries are relatively simple and well defined yet the collision occurs at unknown positions because of the flapping and deformation of the membrane.

By varying independently the properties of both, pendulum and membrane, different impact regimes can be realized and the contact features analysed.

The problem has been investigated by direct numerical simulation of the Navier–Stokes equations two–way coupled with a model for deformable membranes via a fluid/structure interaction algorithm; all the details of the numerical method can be found in [6].

The simulations have been verified and validated by laboratory experiments performed under dynamically similar conditions: both the membrane dynamics (by high-speed contour tracking) and the flow velocity in a two–dimensional plane (by PIV) could be measured and compared with the numerical counterpart.

In figure 1a we report the basic setup of the problem together with an instantaneous snapshot of the numerical calculation and of the experiment after the collision.

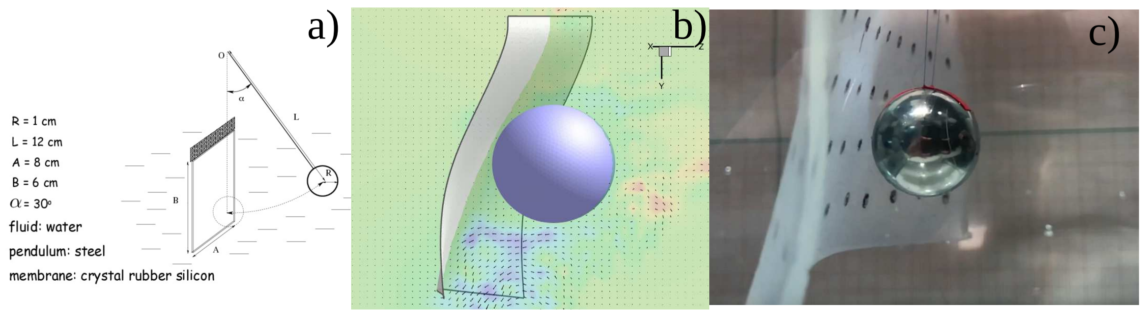

Fig. 1: a) Sketch with the parameters of the experiment, b) snapshot of the pendulum and membrane after the impact (numerical simulation), c) the same as b) but for the experiment.

As the sphere approaches the membrane the fluid in between is squeezed out by the pressure build–

up that, in turn, deforms locally the structure and pushes away the whole membrane. When the pendulum retreats from the membrane, the fluid is sucked towards the gap and this produces a low pressure region that again produces a local deformation and pulls the structure towards the swinging sphere. Depending on the membrane inertia and stiffness and on the pendulum energy, the contact between the bodies may or may not occur and the dynamics of the interaction can change radically.

It has been found that, regardless of the large–scale Reynolds number of the flow, the local pendulum/membrane interaction obeys to the Stokes dynamics that it is well described by the lubrication theory for a sphere approaching a flat plate as described by [7]. Using this theory a flexible and simple contact model has been derived that has made possible the numerical simulation of the various interaction regimes.

References

[1] Rao, A.V., *Dynamics of particles and rigid bodies*, Cambridge University Press, 2006.
[2] Johnson, K.L., *Contact Mechanics*, Cambridge University Press, 1987.
[3] Becker, V. & Briesen, H., *Phys. Rev. E*, **78**, 061404, 2008.
[4] Heitkam, S., et al., *J. Phys.: Condens. Matter*, **29**, 124005, 2017.
[5] Viola, F. et al., *Eur. J. Mech. B/Fluids*, **79**, 212–232, 2020.
[6] Spandan, V.A., *J. of Comp. Phys.*, **348**, 567–590, 2016.
[7] Pasol, L. et al., *Phys. Fluids*, **17**, 073602, 2005.

*corresponding author: verzicco@uniroma2.it

Droplets in electric fields: electrohydrodynamic instabilities and interactions

Petia M. Vlahovska

Engineering Sciences and Applied Mathematics, Northwestern University, Evanston, IL 60208, USA

A classic result due to G.I.Taylor is that a weakly conducting drop bearing zero net charge placed in a uniform electric field adopts a prolate or oblate spheroidal shape, the flow and shape being axisymmetrically aligned with the applied field. In this talk I will overview some intriguing phenomena studied by my group [1]: symmetry-breaking instabilities in strong fields (Quincke rotation resulting in drop steady tilt or tumbling[2,3], vortices around the drop equator[4,5], azimuthal waves on a liquid bridge [6,7]), the streaming from the drop equator that creates visually striking “Saturn-rings” around the drop [8], the electrohydrodynamic lift of a drop near an insulating wall [9], and the non-axisymmetric interactions of drop pairs [10].

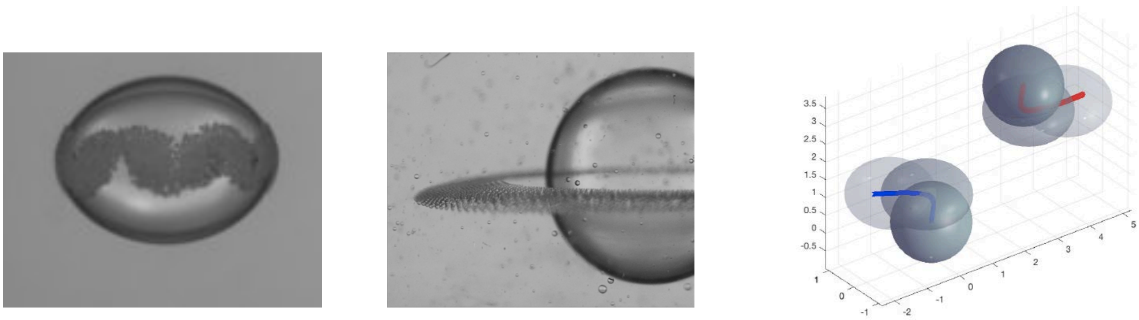

Fig. 1: **Droplet dynamics in a uniform electric field.** Left: Equatorial vortices visualized by colloidal particles [4]. Center: Saturn-ring instability [8]. Right: Attraction-repulsion interaction of two droplets [10].

References

[1] P. M. Vlahovska “Electrohydrodynamics of drops and vesicles” *Annual Review of Fluid Mechanics* **51**:305–330, 2019.

[2] P. F. Salipante and P. M. Vlahovska “Electrohydrodynamics of drops in strong uniform DC electric fields” *Physics of Fluids* **22**:112110, 2010.

[3] P. F. Salipante and P. M. Vlahovska “Electrohydrodynamic rotations of a viscous drop” *Physical Review E* **68**:043003, 2013.

[4] M. Ouriemi and P. M. Vlahovska “Electrohydrodynamics of particle-covered drops” *J. Fluid Mech.* **751**:106-120, 2014.

[5] M. Ouriemi and P. M. Vlahovska “Electrodeformation and rotation of a particle-covered drop” *Langmuir* **32**:6298-6305, 2015.

[6] G. Pradillo and P. M. Vlahovska, “Surface electroconvection instability of a liquid bridge” *in prep.*

[7] G. Kokot, A. Snezhko, P. M. Vlahovska “Deformation and motion of a drop induced by Quincke rollers” *in prep.*

[8] Q. Brosseau and P. M. Vlahovska, “Equatorial streaming of a drop in an electric field” *Physical Review Letters* **119**:034501, 2017.

[9] J. Koch and P. M. Vlahovska “Electrohydrodynamic lift of a drop near an insulating wall” *in prep.*

[10] C. Sorgentone, A.-K. Tornberg, P. M. Vlahovska , “Non-axisymmetric electrohydrodynamic interaction of drop pairs” *in prep.*

*corresponding author: petia.vlahovska@northwestern.edu

The fluid mechanics of kidney stone removal

J. G. Williams[1], B. W. Turney[2], A. A. Castrejon-Pita[3], P. E. Farrell[1], S. J. Tavener[4], D. E. Moulton[1], S. L. Waters*

[1]Mathematical Institute, University of Oxford
[2]Nuffield Department of Surgical Sciences, University of Oxford
[3]Department of Engineering Science, University of Oxford
[4]Department of Mathematics, Colorado State University

Introduction

Flexible uretero-renoscopy provides a minimally invasive surgical treatment for kidney stone removal. A *ureteroscope* is passed to the *renal pelvis* within the kidney through a hollow cylinder, the *access sheath*, and has a central lumen, the *working channel*, for surgical tools, such as high-frequency laser fibres to pulverise stones. Resulting stone dust can impede the surgical view from a minuscule camera at the scope tip; this necessitates irrigation - debris clearance by saline solution, which flows into the kidney through the working channel, and returns via an access sheath (see Figure 1)[1, 2]. Fast debris clearance allows for efficient ureteroscopy. In this talk, we consider the fluid dynamics of irrigation fluid within the renal pelvis, resulting from the emerging jet through the working channel and return flow through the *access sheath* [3]. We explore the effects of system parameters, in particular the Reynolds number of the flow, kidney size, and scope position, on flow patterns and clearance time.

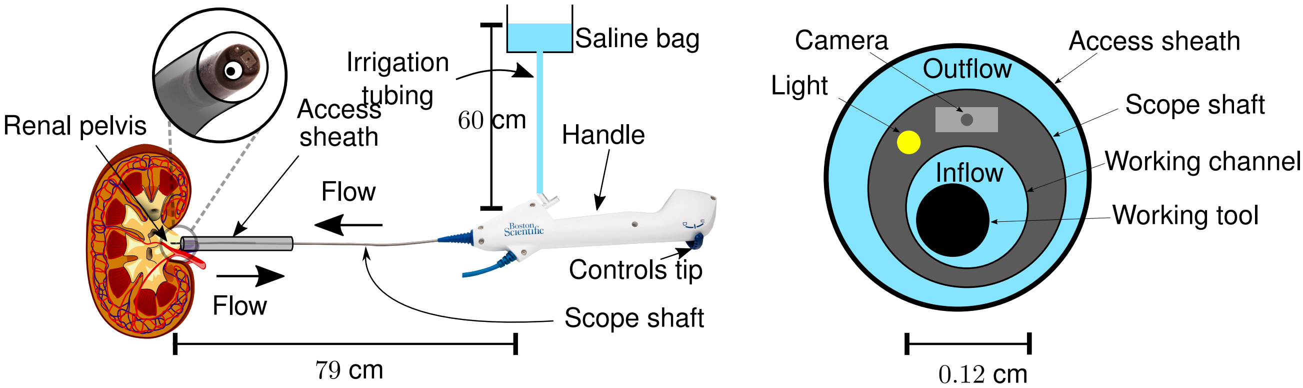

Fig. 1: A photograph of a Boston Scientific ureteroscope (left) with the tip of the scope circled and a zoomed-in schematic provided of the scope tip (right). The scope lies within an access sheath, and a working tool sits inside the working channel. A camera and a light are embedded in the scope wall. Dimensions of the scope shaft and working channel are labelled.

Methods

We represent the renal pelvis as a two-dimensional rectangular cavity and investigate the effects of flow rate and cavity size on flow structure and subsequent clearance time. We model fluid flow with the steady, incompressible Navier-Stokes equations, imposing a Poiseuille profile at the inlet boundary for the jet of saline, and zero-stress on the outlets. We complement numerical simulations with particle image velocimetry (PIV) experiments. We model the clearance of an initial debris cloud via an advection-diffusion equation and define *washout time* T_{90} to be the time required for 90% of the initial debris to exit the cavity.

Results

We demonstrate excellent agreement between experimental flow patterns and the results of numerical simulations, both of which are shown to contain vortical structures (see Figure 2). We demonstrate the existence of multiple solution branches, dependent on the Reynolds number of the flow and the aspect ratio of the cavity, and we compute bifurcation diagrams. We use the calculated flow fields to drive the advection-diffusion equation for debris, and we explore the effects of the initial position of the debris cloud within the vortical flow, and the Péclet number, on washout time. The relevant scaling law between washout time and Péclet number depends on the initial position of the debris cloud within the flow (see Figure 3). With only weak diffusion, debris that initiates within closed streamlines can become trapped. We discuss a flow manipulation strategy to extract debris from vortices and decrease washout time.

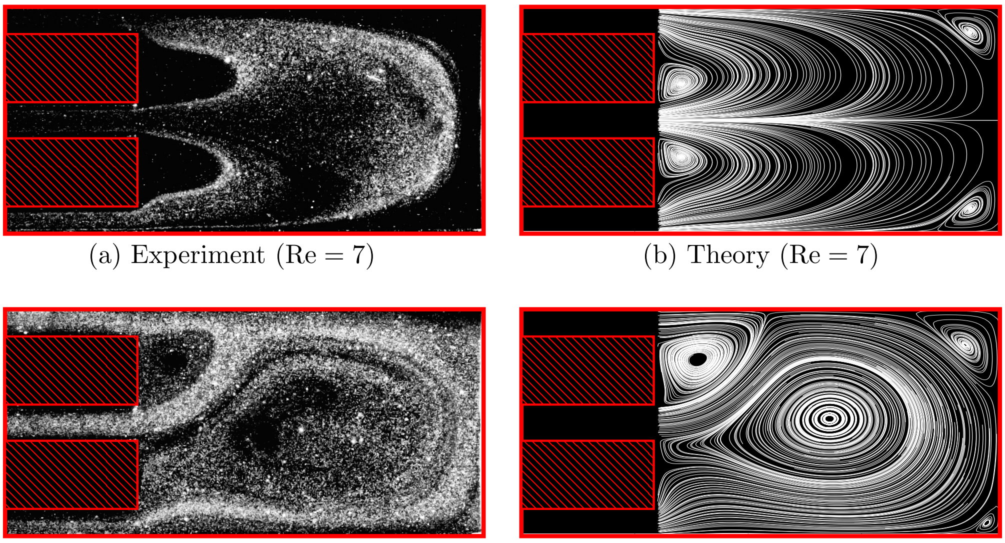

(a) Experiment (Re = 7)
(b) Theory (Re = 7)
(c) Experiment (Re = 34)
(d) Theory (Re = 34)

Fig. 2: A comparison of PIV images (left) with numerically calculated streamlines (right).

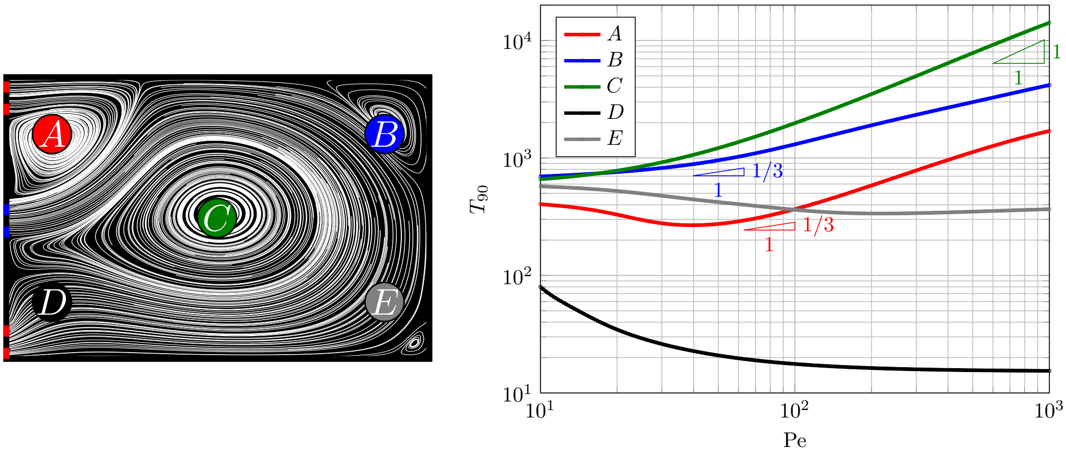

Fig. 3: A log-log plot of T_{90} as a function of Pe for dust placed in positions A, B, C, D, and E (see left). Péclet numbers considered: Pe $= 10^x$ for 200 evenly distributed x values $x \in [1, 3]$.

Conclusions

Complex, asymmetric flow patterns exist during ureteroscopy irrigation and kidney stone debris is likely to be entrapped in vortices, resulting in lengthy washout times. Disturbing the flow can move debris onto streamlines that advect out of the cavity, resulting in shorter times required to clear the field-of-view.

References

[1] Williams JG et al. *J. Endourol.*, **33**: 28-34, 2019.
[2] Williams JG et al. *J. Fluid Mech.*, *In press*, 2020.
[3] Williams JG et al. *J. Fluid Mech.*, *Submitted*, 2020.

*corresponding author: waters@maths.ox.ac.uk

Colloidal mushy layers

M. Grae. Worster[1]*, S. S. L. Peppin[2], J. S. Wettlaufer[3]

[1]Department of Applied Mathematics and Theoretical Physics, University of Cambridge, CMS
Wilberforce Road, Cambridge CB3 0WA
[2]Mississauga, L5G 2K5 Canada
[3]Yale University, New Haven, CT 06520 USA

Introduction

During solidification of multi-component melts, solutions or alloys, the solid phase often forms an intricate microstructure of dendritic crystals aligned with the thermal gradient (figure 1a) within what is called a *mushy layer*. Similarly intricate microstructures can form during the freezing of colloidal suspensions (figures 1b,c,d) but with a greater variety of patterns, including dendrites aligned with the thermal gradient (figure 1b), lenses perpendicular to the thermal gradient (figure 1c) and polygonal structures (figure 1d). Mathematical models of mushy layers formed from solutions [1] often describe them with continuum equations, averaged over the microstructure, which can be used to predict the spatial distribution and temporal evolution of the solid fraction as well as any macro-segregation caused by solute diffusion or convection of the interstitial liquid. We describe an approach to modelling mixed-phase regions (*mushy regions*) within solidifying colloidal suspensions that is independent of their microstructural morphology.

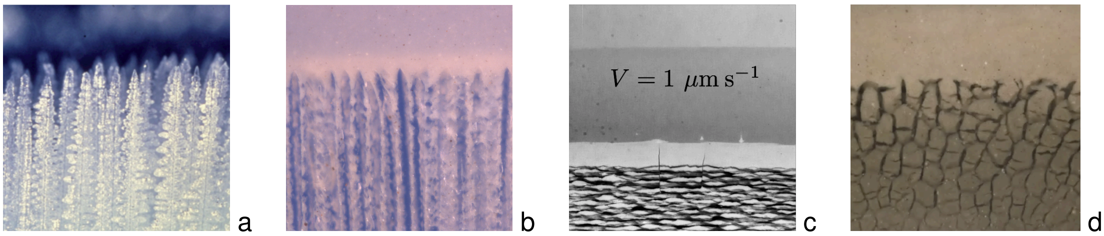

Fig. 1: Mushy layers formed in different materials frozen in vertical temperature gradients. (a) Dendritic mushy layer of ammonium chloride crystals formed from aqueous solution (photo MA Hallworth). (b) Dendritic mushy layer of ice platelets formed from a dilute suspension of bentonite clay in water (photo Stephen Peppin). (c) Mushy layer of horizontal lenses (lower layer) formed from a suspension of alumina particles in water [2]. (d) Polygonal mushy layer formed from a concentrated suspension of bentonite clay in water (photo Stephen Peppin).

Analysis

We find similarity solutions for colloidal suspensions solidifying against a fixed chill. For definiteness, we refer to the suspending phase as water and the resulting solid as ice. We start by finding solutions relating to complete rejection of suspended particles, in which the ice front has position $2\lambda\sqrt{\kappa t}$, where κ is the thermal diffusivity and λ is the scaled height, and determine the conditions under which constitutional supercooling occurs in the suspension ahead of the front. For dilute suspensions, relative motion between particles and water can be described by Fick's law of diffusion. However, relative motion can equivalently be described by Darcy's law [3, 4], which becomes a more tractable formulation at high concentrations, once particles build up to near the close-packed limit against the ice front.

Constitutional supercooling can be relieved by the formation of a mushy layer, in which rejected particles are accommodated in the interstices between ice elements and latent heat is distributed. Key to the development of a continuum model of a colloidal mushy layer is the determination that regelation of large clusters of particles is regulated by Darcy flow through the pores between particles, which leads to a net particle flux equal to

$$\chi \frac{\phi k(\phi)}{\mu} \frac{\rho L}{T_m} \frac{\partial T}{\partial z},$$

independent of the size or shape of the cluster, where χ is the volume fraction of unfrozen colloid, ϕ is the volume fraction of particles, $k(\phi)$ is the permeability to flow between particles, ρ is density, L is latent heat, T_m is the absolute freezing temperature of water and $T(z,t)$ is the local temperature. This contrasts significantly with the regelation of a single particle, which is regulated by flow in a thin premelted liquid film around the particle [5, 6]. Even for clusters of particles, film flow at the contact between a cluster and surrounding ice can have a major influence on the development of microstructure [7] but we have not yet incorporated any consideration of film flow in our model of a colloidal mushy layer.

Results

We will present phase diagrams for binary colloidal systems, determined by osmotic pressure based approximately on considerations of hard-sphere interactions. They are characteristic of the phase diagrams typical of solutions when the particle size is small but become strongly nonlinear for larger particles.

Some key results relating to colloidal mushy layers are presented in figure 2. Hard-sphere colloidal suspensions mimic the behaviour of solutions [8] when the hard-sphere radius is a few Angströms (figure 2a). There is quite a dramatic change in behaviour even when the hard-sphere radius is just 1 nm (figure 2b), with the unfrozen fraction becoming quite uniform. Once the hard-sphere radius is more than about 5 nm, the unfrozen fraction consists of almost-close-packed, consolidated particles (figures 2d, e). As the particle flux increases further, the regelative flux of particles increases, allowing the particle-free layer of ice near the chill to deepen.

The differential equations describing particle distributions are increasingly stiff as the particle size increases and become uncomputable, at least using standard packages, even those designed specifically for stiff systems. Once this happens (at a particle size of order 10 nm) we switch to a simpler mathematical model that exploits the character of the physical system, with sharp transitions between regions of consolidated, close-packed particles and regions with the initially dilute concentrations.

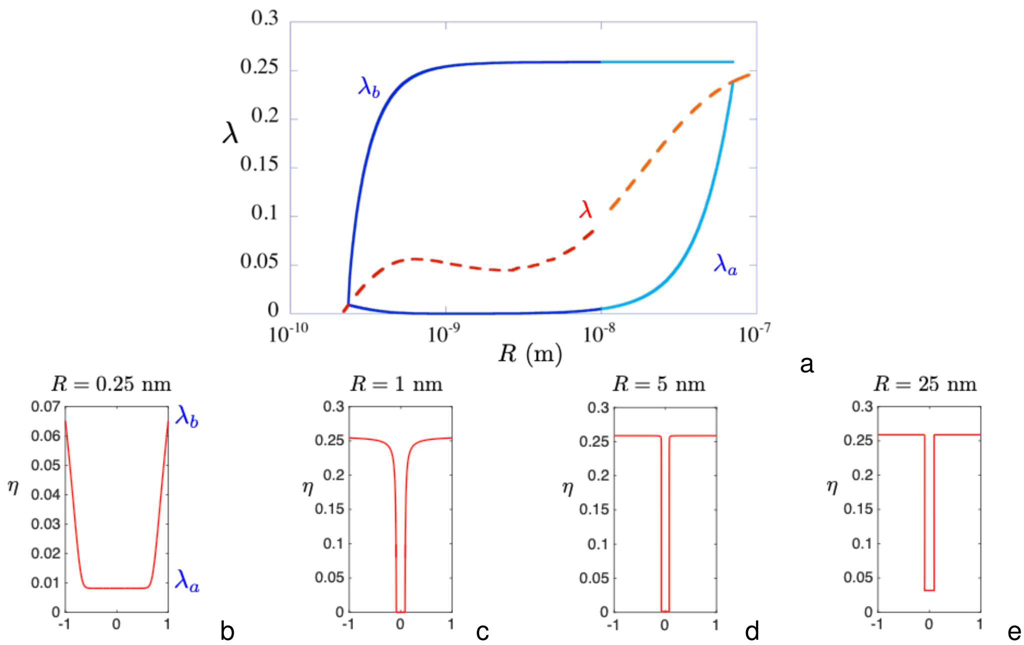

Fig. 2: (a) Scaled thicknesses of a planar interface λ separating pure solid (ice) from colloidal suspension, shown with a dashed curve, and those between a pure solid layer and a mushy layer λ_a and a mushy layer and the original suspension λ_b, shown with solid curves. Panels (b)–(e) show solid-fraction profiles as they vary with the size of the suspended particles.

Conclusions

We have developed a continuum model of colloidal mushy layers based on particle fluxes driven by regelation resulting from thermodynamic buoyancy [6]. Results of the model illustrate how particle distributions vary with particle size and that the high rates of regelation associated with large particles tend to expel particles efficiently to warmer temperatures, preventing mushy layers from forming. Further effects, not currently represented in the model, include film flow, ice entry into pores between particles, and the influences of additional solutes.

References

[1] Worster MG *Interactive Dynamics of Convection and Solidification. NATO ASI Series E219, pp 113–138. Kluwer, 1992.*

[2] Anderson AM & Worster MG *Langmuir* **28(48)**: 16512–16523, 2012.

[3] Peppin, SSL, Elliot JAW & Worster MG *Physics of Fluids* **17(5)**: art. no. 053301, 2005.

[4] Peppin, SSL, Elliot JAW & Worster MG *J. Fluid Mech.* **554**: 147–166, 2006.

[5] Gilpin RR *J. Colloid interface Sci.* **68**:2 35–251, 1979.

[6] Rempel AW, Wettlaufer JS & Worster MG *Phys. Rev. Lett.* **87(8)**: 088501,1–4, 1986.

[7] You J, Wang, Z & Worster MG *Acta Materialia* **157**: 288–297, 2018.

[8] Worster MG *J. Fluid Mech.* **167**: 481–501, 1986.

*corresponding author: mgw1@cam.ac.uk

The effect of horizontal buoyancy on turbulent thermal convection

Ke-Qing Xia[1,2*], Lu Zhang[1,2] and Guang-Yu Ding[1,2]

[1]SUSTech Center for Complex Flows and Soft Matter Research and Department of Mechanics and Aerospace Engineering, Southern University of Science and Technology, Shenzhen, 518055, China
[2]Department of Physics, The Chinese University of Hong Kong, Shatin, Hong Kong, China

Abstract

In thermal convection, any misalignment between the global temperature gradient and the gravity will induce a horizontal buoyancy (with respect to the temperature gradient). This horizontal buoyancy will significantly influence the transport properties of heat, mass and momentum. It may also change the flow morphology in turbulent convection. In this paper, we present an experimental and numerical study, using Rayleigh–Bénard convection (RBC) as a platform, to explore systematically the effect of horizontal buoyancy on heat transport in turbulent thermal convection. Experimentally, a condition of increasing horizontal Rayleigh number (Ra_H) under fixed vertical Rayleigh number (Ra_V) is achieved by simultaneously titling the convection cell and increasing the imposed global temperature gradient. We find that with increasing horizontal to vertical buoyancy ratio (Λ), the overall heat transport is featured by a monotonic increase of vertical heat transport (Nu_V) as well as an increase in the horizontal component (Nu_H). We also propose a method to estimate the horizontal heat transport efficiency Nu_H based on a new analytical form of experimentally measured azimuthal temperature profile at mid-height of the cell, and the results are in reasonable agreement with our numerical findings. We find that the enhancement of vertical heat transport comes from the increased shear generated by the horizontal buoyancy at the boundary layer. The horizontal buoyancy meanwhile decreases the turbulent intensity, and facilitates the formation of two stable 'heat channels' with extremely high local heat flux at each end of the sidewall. The effect of Prandtl number is also studied using direct numerical simulations (DNS). We find that the relative enhancement is higher for lower Prandtl numbers.

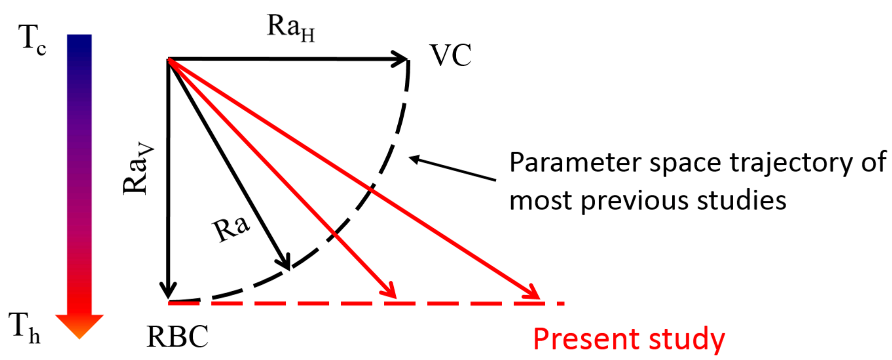

Fig. 1: Comparison between the parameter space trajectories explored in the present study (red dashed line) and that used in previous studies by simply tilting the convection cell (black dashed curve, which is the case in most of the previous studies). In the figure Ra_V is the vertical Rayleigh number and Ra_H is the horizontal Rayleigh number. Here, RBC stands for 'levelled' Rayleigh–Bénard convection, and VC stands for vertical convection.

*corresponding author: xiakq@sustech.edu.cn

A metamorphosis of three-dimensional wave-like structure in early transitional and turbulent boundary layers

X. Y. Jiang[1], C. B. Lee[1*], X. Chen[2], C. R. Smith[3], P. F. Linden[4]

[1]State Key Laboratory for Turbulence and Complex Systems, College of Engineering, Peking University, No.5 Yiheyuan Road Haidian District, Beijing, 100871, P.R.China
[2]State Key Laboratory of Aerodynamics Research and Development Center, No.6, South Section, Second Ring Road, Mianyang City, Sichuan Province, 621000, P.R. China
[3]Department of Mechanical Engineering and Mechanics, Lehigh University, 19 Memorial Drive Bethlehem, PA 18015, United States
[4]Department of Applied Mathematics and Theoretical Physics, Centre for Mathematical Science, Wilberforce Road, Cambridge CB3 0WA, UK

Introduction

Laminar-turbulent boundary layer transition is characterized by the metamorphosis of both wave structure and hairpin vortex. However, the detail evolution of a three-dimensional (3D) wave into a young hairpin vortex is not well understood. This article numerically presents the early spatiotemporal wave-warping process of different transition regimes, illustrating the relationship between 3D waves, low-speed streaks (LSS), and hairpin-vortices. Fig. 1 shows that a warped wave front (WWF) develops into a Λ-vortex for K-type, N-type and O-type transition, respectively, accompanied by multiple folding behavior. The LSS is observed to consist of several wave-like structures at higher wall-normal position

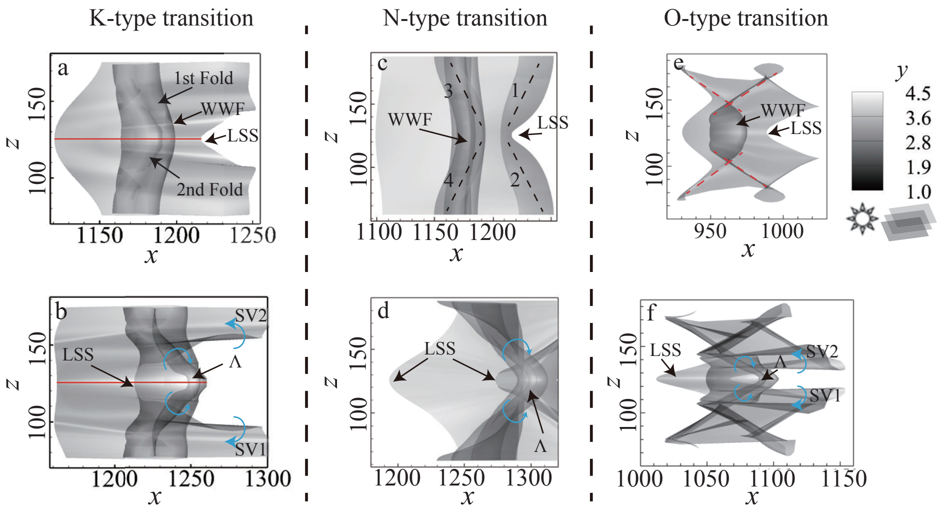

Fig. 1: Evolution of time-line surface initiated at $y = 1.71$ $(\approx 24\%\, \delta_{0.99})$: K-type transition (a, b), N-type transition (c, d) and O-type transition (e, f).

(Fig. 2), which appears to be consistent with previous observations of soliton-like coherent structure [1]. Based on the visualization, the generic transition process is identified as:

- an inflectional region appears in vertical streamwise velocity profiles, accompanied by ejection-sweep behaviors;
- horizontal timelines display a chevron-like structure in near-wall region, which subsequently develops into a long narrowed streaky structure (LSS);
- a WWF with multiple folding behavior and wave-like amplification/damping behavior, develops adjacent to the LSS in the near-wall region, prior to the appearance of Λ-vortices;
- a coherent 3D wave front similar to a soliton is observed within the upper boundary layer, accompanied by regions of depression along the flanks of the wave.

The development of LSS and vortices in an early turbulent boundary layer is also examined using tomographic PIV measurement the same as [2]. Lagrangian tracking method are applied to illustrate the streak bursting process and streak-vortex interaction in the near-wall region. Lagrangian coherent vortices are identified by the scheme of Lagrangian-averaged vorticity deviation (LAVD) [3]. The LAVD is defined by as:

$$\mathrm{LAVD}_{t_0}^{t}(\boldsymbol{x}_0) := \int_{t_0}^{t_1} |\boldsymbol{\omega}(\boldsymbol{x}(s;\boldsymbol{x}_0), s) - \bar{\boldsymbol{\omega}}(s)|\, \mathrm{d}s, \quad (1)$$

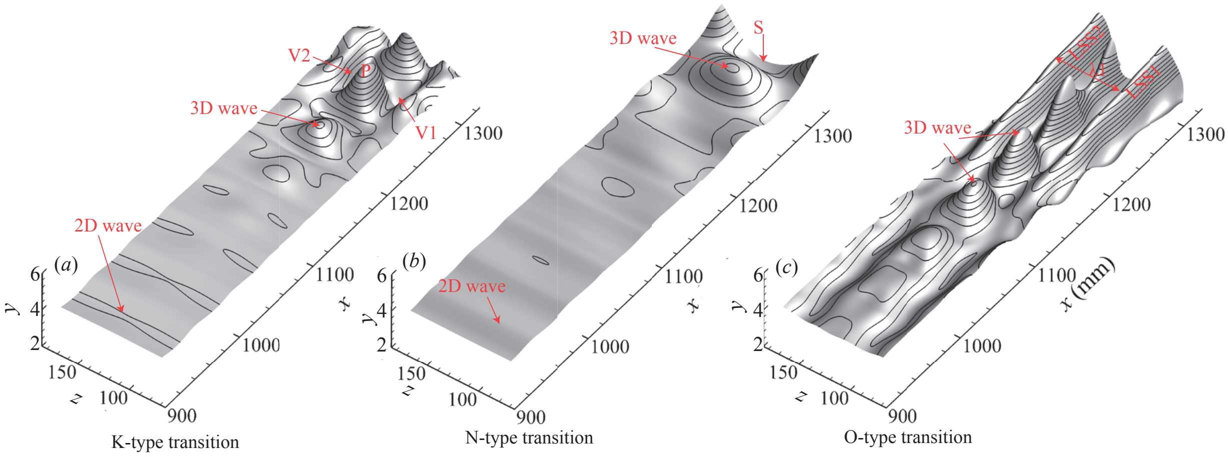

Fig. 2: Evolution of time-line surface initiated at $y = 3.83$ ($\approx 53\%\,\delta_{0.99}$): K-type transition (a), N-type transition (b) and O-type transition (c).

where $\boldsymbol{x}_0$ is the initial position that a specific fluid volume traced from t_0 to t_1, $\boldsymbol{\omega}$ is the vorticity defined as $\nabla \times \boldsymbol{v}$, and $\bar{\omega}$ is the instantaneous spatial mean vorticity over the material domain formed by a set of evolving trajectories. The assessment of LSS in the turbulent boundary layer reveals a close similarity

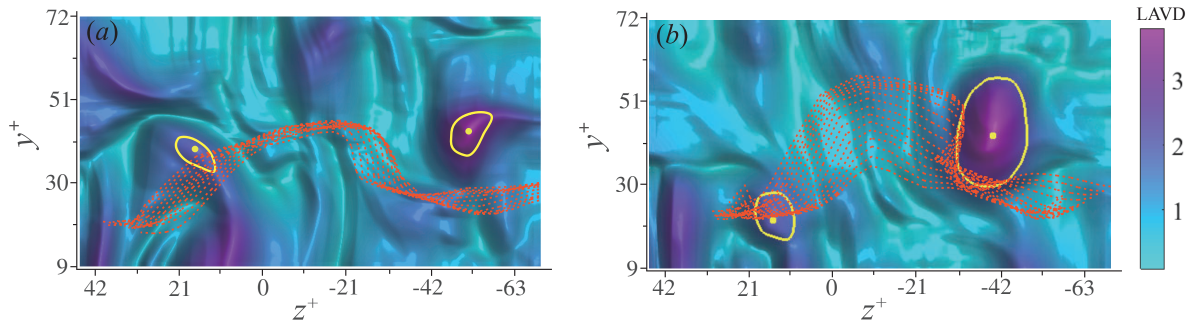

Fig. 3: End view contour of LAVD at different times: $x^+ = -105$, $t^+ = 164$ (a) and $x^+ = 0$, $t^+ = 183$ (b). Superposed on these figures are the corresponding time-line patterns at LSS region.

with previous transitional boundary layer behavior. It is observed that the sides of a 3D wave are where the initial vortex roll-up occurs, with the 3D wave structure appearing to be the initiator of the near-wall vortex structure (Fig. 3). It further observed that quasi-streamwise vortices, located to the sides of a 3D wave, precipitate an interaction with the streak, as shown in Fig. 4.

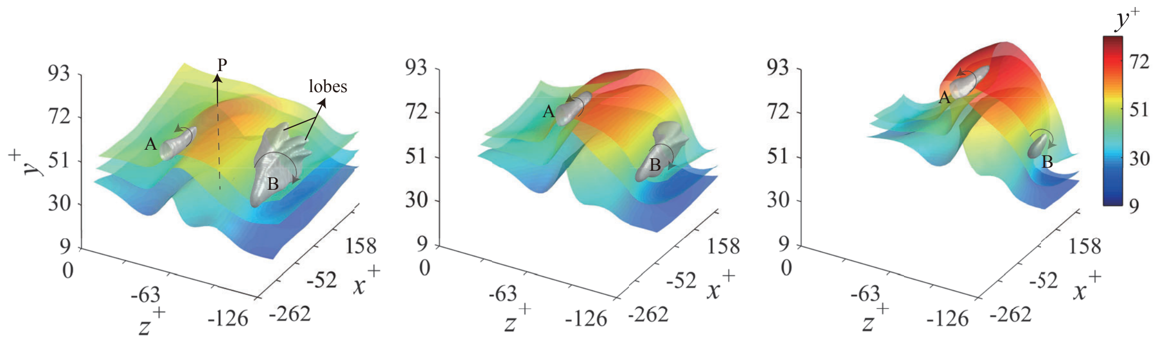

Fig. 4: Spatiotemporal evolution of Lagrangian coherent vortices, in comparison with the evolution of wave-like material surfaces: $t^+ = 151$ (a), $t^+ = 161$ (b) and $t^+ = 170$ (c).

References

[1] Lee CB & Wu JZ. *Appl Mech Rev* **61**:030802, 2008.
[2] Jiang X. *Appl Math Mech-Engl Ed* **40**:261–272, 2019.
[3] Haller G et al. *J Fluid Mech* **795**:136–173, 2016.

*corresponding author: cblee@mech.pku.edu.cn

Turbulence effects in wind-blown sand movements

Xiaojing Zheng[1,2*]

[1]Research Center for Applied Mechanics, School of Mechano-Electronic Engineering, Xidian University, Xi'an 710071, P.R.China
[2]Key Laboratory of Mechanics on Disaster and Environment in Western China(MOE), Lanzhou University, Lanzhou 730000, P.R.China

Introduction

Sand storms and land desertification caused by surface wind shear and sand movements are perplexing environmental subjects of human society, which are essentially the consequences of gas-solid two-phase wall turbulences with high Reynolds number. At present, the predictions of wind-blown sand movements are mainly based on the physics of wind-blown sand proposed by Bagnold (1941), while the numerical simulations of atmospheric turbulent flow fields are based on one-dimension RANS (Anderson, 1988) or LES (Dupont, 2013). Up to date, rare attempts have aimed to investigate the effects of heavy solid particles on the high-Reynolds number wall turbulences except for Wang & Richter (2019). This lecture will start from a trans-scale numerical model for the formation and evolution of an aeolian dune field covering hundreds of square kilometers (Zheng, 2009) which reveals the limitations of existing RANS and LES models for wind-blown sand flows. Systematic measurements conducted at the Qingtu Lake Observation Array (QLOA) with 7400-hour synchronous data of sand-free and sand-laden turbulent flows in Atmospheric Surface Layer (ASL), as well as experimental results obtained in wind tunnel are then introduced. The turbulence effects in wind-blown sand movements are discussed in the following perspectives: 1) the variation laws of the turbulent kinetic energy (TKE) and the TKE proportions of the Very-Large-Scale Motions (VLSMs) with height in sand-free flow fields in ASL; 2) the significant differences between the wall turbulences in fluid dynamics and the 'gusty wind' in meteorology as the description of the wind field in the ASL; 3) the super-scale structures in the PM10 concentration fields firstly identified in sand storms whose streamwise length scales also reach up to 3 times the thickness of the boundary layer (δ), and their characteristics, laws and differences with VLSMs in clean-air flow fields; 4) the influence of the near-wall motions of heavy particles on the turbulent structures and the Reynolds number effects of the high-Reynolds number wall turbulences, from which we suggest two critical Reynolds number indicating the appearance of VLSMs and the streamwise scales of VLSMs no longer increasing in the Turbulent Boundary Layer(TBL). Finally, this lecture emphasizes that the study of gas-solid two-phase wall turbulences with high Reynolds number is not only helpful to depth the understanding of particle-turbulence interaction, but also of importance to promote the physics of wind-blown sand and improve the prediction accuracy of wind-blown sand movements and sand storms.

Detailed instructions

Methods The analysis and conclusions of this lecture are based on the field measurements of the sand-free and sand-laden flows in the ASL and the wind tunnel experiments on the wind-blown sand flows with and without the interaction between particles and the wall. The field observation is based on the Qingtu Lake Observation Array (QLOA). Comparing with the SLTEST (Hutchins & Marusic, 2007), this array can achieve full-field observation of the ASL including streamwise towers, synchronous high-frequency measurements of three-dimensional wind velocities, dust concentrations, temperatures, humidity, visibility, electric fields etc.. The total amount of the accumulated data till now have been above 4.7Tb, including nearly 600-hour high-quality stationary data. The characteristic Reynods numbers for clean-air and sand-laden flows (including sand storms) are $\mathrm{Re}_\tau \sim 4.7\times10^6$ and $\mathrm{Re}_\tau \sim 5.4\times10^6$ respectively, which are the highest Reynods number conditions achieved in the study of clean-air and particle-laden two-phase flows at present. The wind tunnel experiments were conducted with hot-wire anemometers and a 4-CCD PIV system whose field of view was 5δ in the streamwise direction. The air flow fields and sand-particle motions formed respectively by laying a sand bed on the bottom wall and a sand feeder at the top wall were synchronously measured.

Results and Conclusions For the sand-free flows in the ASL, it is found: 1) the TKE of VLSMs increases with height which is different from LSMs and the proportion of energy can reach 60%; 2) the contribution of the 'gusty wind' to the total TKE is significantly less than that of VLSMs and the energy loss of the 'gusty wind' accounts for 50% of the contributions by VLSMs and LSMs; 3) the amplitude modulation coefficients between turbulent structures demonstrate a scale effect in which VLSMs have the strongest modulation effect on structures smaller than 0.3δ.

For the sand-laden flows in ASL, we found that: 1) there exists one type of coherent structures with streamwise scales larger than 3δ in the PM10 concentration fields in the sand storms. As shown in Fig.1, the streamwise scales of the PM10 structures are related to the vertical wind velocity fluctuations, which are larger than those of VLSMs below 14m, and their inclination angles are larger than those of VLSMs; 2) based on the 1-Hz time series of wind velocities at a given height near the surface, it is practicable to predict the wind velocity time series at any heights, and thus calculate one of the key parameters to predict sand storms, that is, the sand transport flux above 20m which in contrast has been reported to be zero above 0.3m by current RANS simulations; 3) the heavy particles in wind-blown sand flows lead to the scale variation even the breakup of VLSMs, which is related to the existence of the particle-wall interaction effects and the height from the wall.

With regard to the Reynolds number effect, we revealed that: 1) the outer-scaled location of the middle of the log layer keeps invariant with the Reynolds number, while the inner-scaled location of the lower bound of the log layer increases with the Reynolds number which demonstrates a significantly different trend from the previous studies that have suggested the lower bound of the log layer be constant or increase with Reynolds number in a 1/2 power law, as shown in Fig.2; 2) there are two critical Reynolds number with respect to the appearance of VLSMs and the invariance of the streamwise scales of the VLSMs in the TBL, as shown in Fig.3, which are about Re_{c1}=500 and Re_{c2}=1200 respectively.

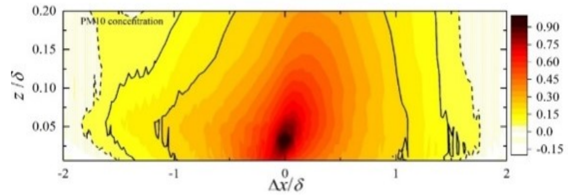

Fig. 1: Super-scale structures identified in the PM10 concentration field.

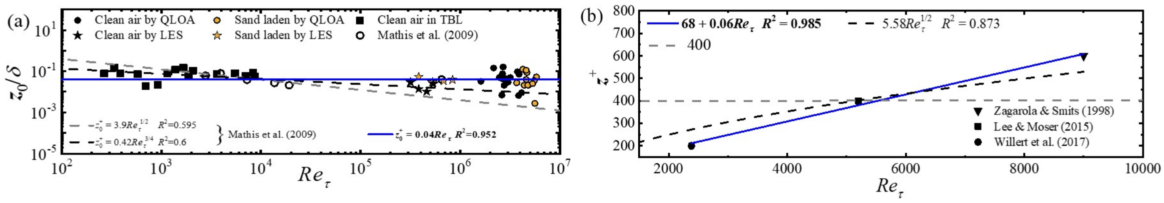

Fig. 2: The locations of the middle (a) and the low bound (b) of the log layer varying with Reynolds number.

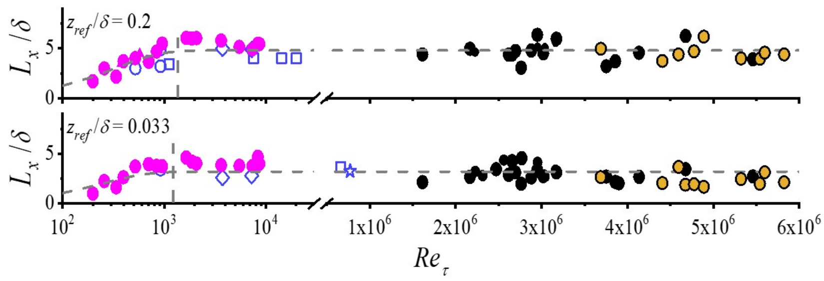

Fig. 3: The streamwise scales of the VLSMs based on the two-point correlations in the TBL.

Acknowledgement

This research was supported by grants from NSFC (no. 11490553).

References

[1] Bagnold R A. *The Physics of Windblown Sand and Desert Dunes*. 1st ed, William Morrow & Company, 1941.
[2] Anderson R S. & Haff P K. *SCIENCE*. **241**:820-823, 1988.
[3] Dupont S et al. *J GEOPHYS RES-ATMOS*. **118**:7109-7128, 2013.
[4] Wang, G. & Richter, D. H. *J FLUID MECH*. **868**:538-559, 2019.
[5] Zheng X. *Mechanics of Wind-blown Sand Movements*. 1st ed, Springer Science & Business Media, 2009.
[6] Wang, G. & Zheng X. *J FLUID MECH*. **802**:464-489, 2016.
[7] Hutchins, N. & Marusic, I. *J FLUID MECH*. **579**:1-28, 2007.

*corresponding author: xjzheng@xidian.edu.cn